Cortical Surface Recurrent Brain-Computer Interfaces

Stavros Zanos

A dissertation

submitted in partial fulfillment of the requirements

for the degree of

Doctor of Philosophy

University of Washington

2013

Reading Committee:

Eberhard E. Fetz, Chair

Jeffrey G. Ojemann

Steve I. Perlmutter

Program Authorized to Offer Degree:

Physiology and Biophysics

University of Washington

Abstract

Cortical Surface Recurrent Brain-Computer Interfaces

Stavros Zanos

Chair of the Supervisory Committee:

Prof. Eberhard Fetz

Physiology and Biophysics

The output of a “traditional” brain computer-interface (BCI) is the operation of an effector mechanism, like a cursor or a prosthetic arm. In contrast, the output of a recurrent brain-computer interface (rBCI) is electrical stimulation delivered directly into the central nervous system (CNS). Recurrent BCIs have been used to artificially bridge two separate sites in the CNS whose communication may have been interrupted. They have also been used to associate activity of a site in the CNS with stimulation of another site, to produce synaptic plasticity between the two sites. To date, rBCIs have utilized intracortical implants to record neural activity and deliver electrical stimuli, which have problems that limit their clinical applicability. These limitations can be addressed by cortical surface electrodes, subdural or epidural, that can capture electrocorticography (ECoG) signals and deliver electrical cortical surface stimulation.

We first examine the recording capabilities of cortical surface arrays. We study the relationship of ECoG signals with motor behavior and EMG activity from upper extremity muscles. We demonstrate that EMG activity can be decoded from multichannel ECoG, and document the gradual decrement in decoding performance over several months of recording.

Second, we examine the stimulation capabilities of cortical surface arrays. We characterize the effects of repetitive stimulation on the electrode-tissue interface, by measuring electrode impedance. We determine the impact of stimulation on cortical excitability, by measuring stimulus-evoked motor responses. Finally, we examine the effect of stimulation on spontaneous cortical activity, as evidenced by ECoG power at different frequencies.

Third, we investigate a cortical surface rBCI system to study the role of sensorimotor beta oscillations in synaptic plasticity. Stimulation at a cortical site was triggered from specific phases of beta (15-25 Hz) oscillatory episodes of ECoG recorded from a different site. The effects of conditioning stimulation on cortical connectivity were determined through cortically-evoked potentials and ECoG phase coherence. We document a short-term change in cortical connectivity following beta oscillations that is mediated by synaptic modification and follows a Hebbian-like rule.

Our findings on properties of cortical surface recording and stimulation will promote translation of these techniques to clinical applications. Our demonstration of changes in cortical connectivity induced by a cortical surface rBCI furthers our understanding of cortical oscillations and provides a paradigm for studying activity-dependent cortical plasticity using these less invasive implants.

Table of contents

Chapter 1: Introduction

The output of a "traditional" brain computer-interface (BCI) is usually the operation of an effector mechanism, like a cursor or a prosthetic arm. A recurrent brain-computer interface (rBCI) is different in that its output is delivered directly into the central nervous system (CNS) in the form of electrical stimuli (Figure 1). Recurrent BCIs have been used in two main applications. The first is to artificially bridge two separate sites in the CNS whose communication has been interrupted. For example, motor signals from the brain can be translated directly into electrical stimuli to the spinal cord (Nishimura et al. 2013) or to a muscle (Moritz et al. 2008) and generate movement in a subject with spinal cord injury. The second is to associate activity of a site in the CNS with stimulation of another site, with the aim of producing plasticity between the two sites (Jackson et al. 2006a; Nishimura et al. (in press); Rebesco et al. 2010). Controlling targeted brain plasticity can find application in disorders like stroke, partial spinal cord injury, traumatic brain injury etc.

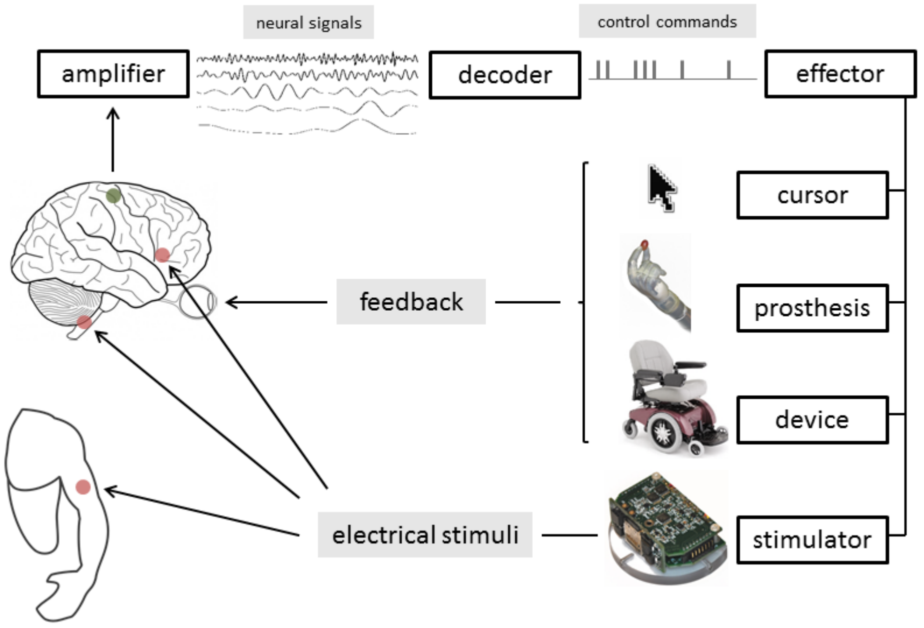

Figure 1. The main components of a brain-machine or brain-computer interface. Neural signals generated by the brain and captured by cortical electrodes are amplified by appropriate hardware; decoding algorithms then translate signal features into commands for the control of an effector mechanism. That mechanism can be a computer cursor, a prosthetic arm, a device for moving around etc. The output of that mechanism provides feedback, usually visual, that is used by the subject to adjust her neural signals in order to gain better control. The electrical stimulator is another effector mechanism, whose output, electrical impulses, is delivered directly into the brain, the spinal cord or skeletal muscles.

All those implementations of rBCIs used intracortical implants to record neural activity, and in some cases to deliver stimuli. Recurrent BCIs that rely on stable single unit activity over several hours or days (Jackson et al. 2006a; Nishimura et al. (in press); Rebesco et al. 2010) have limited clinical applicability given current recording technology. Moreover, intracortical implants are associated with an increased infection risk and significant gliosis around the electrodes, which degrades signal quality (Geddes and Roeder 2003a; Spira and Hai 2013). One aim of this thesis is to extend the applicability of rBCIs in clinical applications by developing less invasive implants and use of neural signals that are more stable in time. A recording and stimulation vehicle that could potentially meet these requirements is cortical surface, subdural or epidural, implants that can capture electrocorticography (ECoG) signals and deliver electrical cortical surface stimulation (ECS). However, a number of important issues, regarding the use of these implants in rBCIs, remain unresolved.

Even though ECoG and its application in “acute” BCIs have been thoroughly evaluated in humans (e.g. Schalk and Leuthardt 2011), the use of ECoG in chronic BCIs has not been explored. The first chapter of this thesis discusses the relationships of ECoG activity recorded from the sensorimotor cortex of behaving NHPs (define) with their motor behavior, as documented by EMG activity from specific arm and forearm muscles. The extent to which ECoG can be used to decode EMG activity is also addressed, as well as the decoding performance across several months of experiments. We find that stereotypical ECoG changes, in the time and frequency domains, occur with motor movement. In addition, ECoG can be used for decoding EMG activity, with accuracy comparable to that of single unit recordings. This accuracy declines with increasing the interval between training and testing of the decoders, as well as with progressing implant age.

Cortical surface arrays have been in use clinically for stimulation mapping of the cortex prior to or during neurosurgical procedures (e.g. Berger et al. 1990), but the long-term effects of ECS on the electrodes themselves, as well as on the cortex, have not been documented. The second chapter of this thesis discusses the effect of prolonged, repetitive ECS on the electrode-tissue interface, cortical excitability and spontaneous cortical activity. We found that repetitive ECS for 30 minutes increases the electrode impedance, decreases cortical excitability and affects spontaneous cortical activity. These effects last from less than 24 to more than 48 hours after stimulation.

The third chapter of the thesis discusses the implementation of a cortical surface rBCI to study the functional role of oscillations in the sensorimotor cortex and to induce and document ECoG activity-dependent cortical plasticity. We describe a relatively short-lasting form of stimulation-induced change in effective cortico-cortical connectivity, which manifests as a change in the amplitude of stimulus-evoked cortical potentials and a change in the phase coherence of spontaneous ECoG activity. This effect appears to be mediated by short-term synaptic plasticity and is dependent on the level of cortical depolarization at the time of stimulation, as assessed by the phase of the beta oscillation that triggers the stimulus.

In parallel to those studies in the use of cortical surface implants in rBCIs, we designed and implemented a portable system capable of recording ECoG potentials and delivering ECS in freely behaving nonhuman primates. This system expanded and extended the original Neurochip's capabilities (Jackson et al.

2006b) beyond recording single-unit spikes and delivering intracortical microstimulation (ICMS). The Neurochip2, can record a variety of signals (spikes, local field potentials, ECoG and EMG), extract different features of these signals in real-time, and deliver ICMS or ECS upon the detection of specific patterns of these features (Zanos et al. 2011).

Chapter 2: Long-term decoding of forearm muscle activities by electrocorticography

Introduction

Brain-machine interfaces (BMIs) allow communication between the brain and the environment, beyond the natural means of sensory and motor neural systems. In that sense, they provide a methodology for augmenting or restoring lost or impaired sensory, motor or cognitive neural function. They are also used to probe and manipulate different aspects of the normal function of the nervous system and therefore provide insight to its physiology (Hatsopoulos and Donoghue 2009a). In the typical case, a motor BMI comprises an electrode array that records brain signals that are related to an aspect of motor behavior, a decoder that transforms these signals to a variable that can be used to control an effector system and the effector system. In closed-loop systems, there is the addition of a feedback loop (Gerven et al. 2009).

In the BMI cycle, the selection of the electrode array and its placement are most important, and often present the most technical challenges. On one hand, noninvasive recording of electrical brain signals, namely scalp electroencephalography, is safe but has low signal-to-noise ratio (SNR) making it useful only in specific clinical scenarios (Birbaumer 2006; Krusienski and Wolpaw 2009). On the other hand, invasive methods, namely intracortical recordings of single-unit activity and local field potentials (Donoghue 2008; Green and Kalaska 2011; Nicolelis and Lebedev 2009; Santhanam et al. 2006; Schwartz et al. 2006) yield signals with the highest SNR but have a number of drawbacks. First, they exhibit significant signal variability (Chestek et al. 2011; Suner et al. 2005) and, because of that, require large numbers of recording channels, to allow stable decoding of movement variables (Carmena et al. 2005), and almost daily re-calibration (Chestek et al. 2011). Second, intracortical arrays penetrate the pia and have been associated with cortical neuronal loss and extensive gliosis (Griffith and Humphrey 2006;

Szarowski et al. 2003; Vetter et al. 2004; Ward et al. 2009), properties that could potentially limit their long-term functionality.

Electrocorticography (ECoG) arrays are surgically placed in the epidural or subdural space and can both record brain surface potentials and deliver cortical surface stimulation. They have been successfully used in human BMI applications, as they combine a non-penetrating approach, and therefore less potential for reactive cortical histological changes, with high SNR, increased temporal and spatial signal resolution, and signal stability (Schalk and Leuthardt 2011). The decoding ability of ECoG for certain movement variables is superior to that of EEG and almost equivalent to that of intracortical signals (Chao 2010; Schalk et al. 2007) The use of subdural electrodes in animal research has been limited to rabbits and rats; surprisingly, very few studies have considered them in the non-human primate, an excellent model for human motor function and disease (Chao 2010; Craggs 1975).

Most motor BMIs use neural signals to decode a kinematic variable, namely, the position, velocity or acceleration of a limb (e.g. Bansal et al. 2012; Carmena et al. 2003; Chapin et al. 1999; Donoghue 2008; Ganguly and Carmena 2009; Hochberg et al. 2012; Schwartz et al. 2006; Serruya et al. 2002). Kinematic variables yield a relatively noise-free control signal that is suitable for controlling prosthetic devices, artificial limbs or computer cursors by paralyzed patients. Functional electrical stimulation (FES) is another approach to restoring movement, in which electrical stimuli are delivered to peripheral nerves that innervate the muscles, that themselves move the limb (Peckham and Knutson 2005). Brain control of an FES system could exploit decoding of muscle activations from cortical signals. This has been accomplished with EEG (Lauer et al. 1999; Pfurtscheller et al. 2003) and intracortical signals (Carmena et al. 2003; Cherian et al. 2011; Flint et al. 2012a; Nazarpour et al. 2012; Pohlmeyer et al. 2007), but not with ECoG. In most of those studies, muscle activity was decoded in conditions of a controlled motor task, but not during “naturalistic” behaviors. Furthermore, the long-term performance of cortical signals in decoding of muscle activity is unknown.

We studied the performance of ECoG signals recorded from the sensorimotor cortex of nonhuman primates in decoding the activity of a number of contralateral forearm muscles, in a self-paced, naturalistic reaching and grasping task, over a period of 6 months. ECoG recordings were obtained through 2 different types of subdural arrays, of different electrode diameters and inter-electrode distances. Using decoders based on the instantaneous power of a small number of frequency ranges, we found that EMG activity of multiple muscles can be decoded at high accuracy. Decoding accuracy degraded with time but re-training restored it. Even though delta range (2-4 Hz) power had the highest modulation between movement and rest, power in the high-gamma range (70-100 Hz) was the most useful for decoding EMG activity. A larger cortical coverage area and smaller diameter electrodes were associated with improved decoder performance. Finally, an inter-electrode distance of 75-150 µm seems to be associated with maximum decoder performance.

Methods

Behavioral task

Two monkeys were trained to sit calmly in a primate chair, with their head restrained at a neutral, comfortable position, facing forward. Each experimental session began with the monkey brought into the lab, seated in the primate chair. One of the arms was restrained at the elbow and at the wrist, at a neutral position (elbow flexed at a 90 degree angle, wrist straight). The experimenter presented a treat at a random location in the monkey’s extrapersonal space, within its reach; using its free arm, the monkey started from rest to reach for the treat. The treat was either kept at the location originally presented, in which case the monkey would simply reach and grab it, or was moved around inside its visual field, in which case the monkey would “chase” it for about 0.5 to 3 seconds, before finally grabbing it. Treats were chosen to engage both finer (e.g. raisins) and coarser (e.g. apple pieces) finger movements during grabbing. After grabbing the treat, the monkey brought the treat to its mouth, either directly or, in some sessions, indirectly, following a trajectory imposed by a barrier placed on the primate chair, between its reaching space and its head. The duration of each session ranged between 30 and 60 minutes. Several 1- to 3-minute-long breaks, with the monkey being still, were taken during those sessions. ECoG and EMG were recorded during both “reaching/grasping” and “resting” periods of each recording session.

Implants and surgical procedures

Cortical implants

Two different types of cortical surface arrays of 4x8 electrodes were implanted in the 2 animals. A mini-grid had external dimensions of 15.25x28.53mm (435mm^2 area); platinum discs; 2mm exposed electrode diameter; 3mm inter-electrode distance; and was custom-manufactured by Ad-Tech Medical Instruments Corporation (Racine, WI USA) (Figure 1). A micro-grid had external dimensions of 7.0x13.5mm (95 mm^2 area); platinum-iridium contacts; 75µm exposed electrode diameter; and was manufactured by PMT Corporation (Chanhassen, MN USA) (Figure 2).

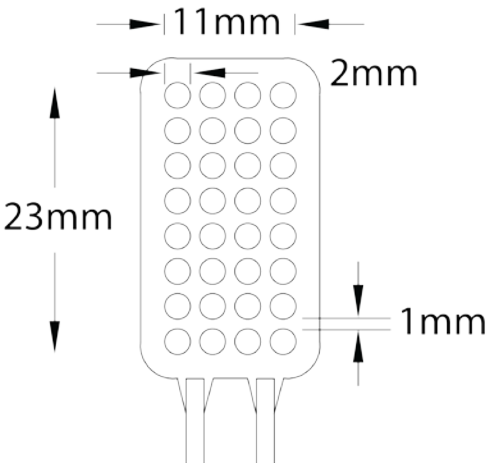

Figure 2. Schematic representation of the mini-grid array.

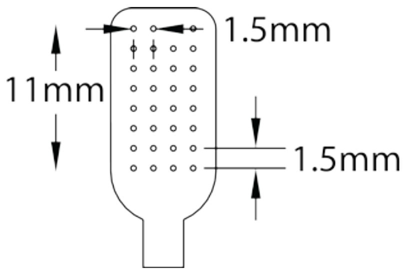

Figure 3. Schematic representation of the micro-grid array

Monkey X received both types of arrays, one on each hemisphere (Figure 3). After a single, bilateral, frontal craniotomy that exposed the two central gyri, the dura overlying them was incised and reflected to reveal the central sulci. Each of the arrays was placed on the pia overlying the precentral gyri, as close to the arm/hand representation as possible, based on anatomical landmarks and cortical stimulation mapping. The mini-grid was placed on the left hemisphere and the micro-grid on the right hemisphere. The arrays were then covered by the dural flap, which was sutured to the dura around the defect. A piece of autologous periosteum, extracted from the skull flap, was placed over each of the suture lines to reinforce it and prevent cerebrospinal fluid leakage. The skull flap was then placed over the two implants and secured with acrylic cement. Connectors were secured on the skull with acrylic cement and enclosed in a titanium casing that was also attached to the skull with cement and skull screws. Several of the skull screws were electrically connected and served as ground leads. Monkey C received a micro-grid array on its right hemisphere, using a similar technique; for technical reasons, the array was placed anterior to the convexity of the precentral gyrus (Figure 3). Steroids were administered parenterally 24 hours and immediately before each of the implant surgeries.

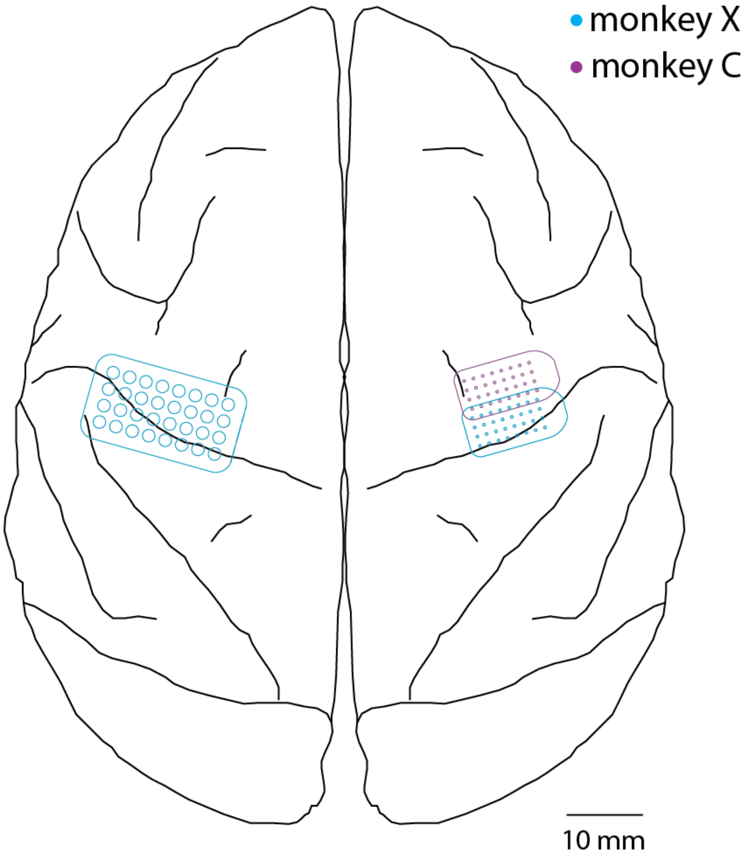

Figure 4. Schematic representation of the subdural array implants used in the two animals. Dimesions are approximately to scale.

Muscle implants

In separate surgeries, intramuscular, subcutaneously-routed, EMG wires were implanted on several upper extremity muscles. EMG wires were inserted through the epimysium and brought in contact with the surface of the muscle belly, without penetrating it. Monkey X was implanted with 3 wires in each of the following muscles in the right upper extremity: abductor pollicis longus (APL), extensor digitorum for the 2nd and 3rd finger (ED23), flexor digitorum superficialis (FDS), biceps, triceps, deltoid (posterior segment), pectoralis major, teres major; also, 3 wires in each of the following muscles in the left upper extremity: extensor digitorum communis (EDC), extensor digitorum ulnaris (EDU), flexor carpi radialis

(FCR), flexor carpi ulnaris (FCU), biceps, triceps, deltoid (posterior segment), pectoralis major. Monkey C was implanted with 2 wires in each of the following muscles in the left upper extremity: extensor carpi ulnaris (ECU), EDC, extensor carpi radialis (ECR), brachioradialis (BR), FCR, APL, triceps, deltoid (posterior segment). Connectors to the EMG wires were placed in the titanium casing, and secured with acrylic cement.

Muscles were grouped in 2 groups, proximal and distal: proximal muscles were those whose effector joint was the elbow or shoulder, and distal muscles were those whose effector joint was the wrist or the metacarpophalangeal joint. Proximal muscles included biceps, triceps, deltoid, perctoralis major and teres major. Distal muscles included APL, ED23, FDS, EDC, FCR, FCU, ECU, APL, ECR and BR.

Recordings

Simultaneous electrocorticographic (ECoG) and contralateral EMG recordings were made during performance of the reaching task, in the booth. The ECoG recordings comprised signals from all 32 electrodes of a single array; those were recorded single-ended (relative to tissue ground) using two 16-channel ZC-16 headstages (Tucker-Davis, Alachua, FL) and two 16-channel, DC-coupled g.USB amplifiers (g.tec medical engineering Gmbh, Schiedlberg, Austria). The EMG recordings comprised single-ended signals from all EMG wires, recorded on another two 16-channel, DC-coupled g.USB amplifiers. Sampling of both ECoG and EMG signals was done at 24 bit resolution, sampled at 4 Ks/sec, with no filtering. The data from amplifiers were streamed to a personal computer through a USB 2.0 link, then stored and visualized in real-time using a custom-made Matlab-based graphical user interface.

Analysis

All analyses were performed using custom software written on Matlab v7.11.0 (The MathWorks Inc., 2010).

Pre-processing of EMG and ECoG signals

Bipolar EMG signals were derived from single-ended recordings by sample-by-sample subtraction. When more than 2 signals from the same muscle were recorded, the 2 better ones (in terms of noise and artifacts) were selected. Bipolar EMG signals were then converted to root mean square (RMS) EMG. The temporal resolution at which RMS-EMG was computed was 25 ms. Each RMS-EMG signal was then normalized between the values of 0 and 1 (equal or greater than the 99.9th percentile of that RMS-EMG's values).

For each RMS-EMG signal, epochs when muscle activation occurred were semi-manually determined, resulting in a number of EMG activity-onset and offset triggers. That method consists of manually setting an EMG activation threshold based on visual inspection of EMG signals during the entire recording session; EMG onset and offset triggers are then determined automatically, by threshold crossings. Only triggers that followed a rest period of at least 3 seconds and activation period of at least 2 seconds were accepted, to avoid re-triggering on ongoing EMG activity.

By visually inspecting the ECoG recordings, channels or recording epochs with excessive noise or artifacts were excluded. The common average reference (CAR) was then calculated, by averaging the single-ended ECoG recordings across all channels. Just curious (this is not for the thesis; if you remember, let's just discuss it) – if the array covered a very large area of cortex, would you calculate the CAR from a subset of the electrodes within a certain distance from the recording electrode? Or is it common for ECoG signal processing to subtract out the average across the entire array? Unipolar, CAR-corrected ECoG was derived by subtracting the CAR from the single-ended recording of each channel. Laplacian ECoG was also derived by subtracting from the single-ended ECoG from each electrode, the average of single-ended ECoG from the electrodes surrounding it (Figure 4).

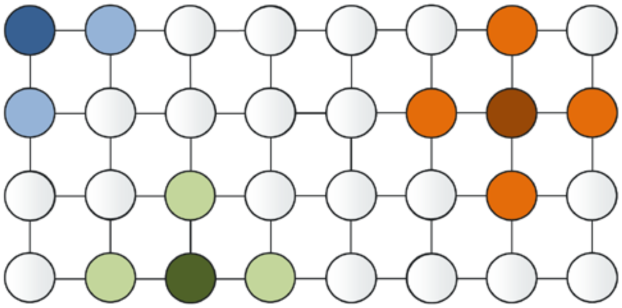

Figure 5. Schematic representation of the surface Laplacian derivation. The signal from each "active" electrode (dark-colored circles) is re-referenced relative to the average of signals from surrounding "reference" electrodes (light-colored circles). Depending on the location of the active electrode on the array, there are 2, 3 or 4 reference electrodes.

Instantaneous ECoG power

In order to generate the time-series of ECoG power at different frequencies, the raw ECoG signal was band-pass filtered in a number of pre-determined frequency ranges: 2-4 Hz (delta), 4-8 Hz (theta), 8-12 Hz (alpha), 15-25 Hz (beta), 35-50 Hz (low gamma), 70-100 Hz (high gamma). Hilbert transform was applied to the filtered data, to produce the analytic amplitude at that frequency and power was derived by squaring the analytic amplitude. Power time series were then binned at 25 ms. The local motor potential (LMP) was also derived, as the running average of the raw ECoG signal at each electrode, binned at 25 ms. There were a total of 7 power features per ECoG channel.

Visualizing muscle activity-related ECoG power changes

In order to visualize and quantify ECoG power changes related to EMG activity on different muscles, a time-frequency map of average ECoG power on each channel was computed, around EMG activity-onset and -offset triggers. Because ECoG power drops quickly with increasing ECoG frequency, and in order to avoid masking power changes in higher-frequencies by the, much larger, ones in lower-frequencies, ECoG power at each frequency was adjusted by ECoG power (in that frequency) during times when no muscle activity occurred. Those "rest times" were determined by applying a manually-defined EMG level threshold on the rectified EMG signal; times when rectified EMG was above threshold continuously for more than 500 ms, were termed as "movement", and the remaining times as "rest" (Figure 5).

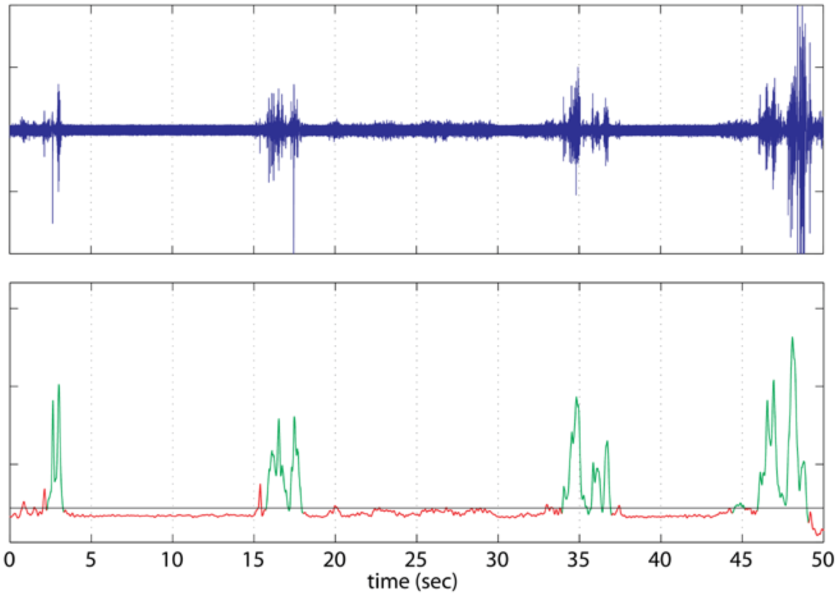

Figure 6. Determining "activity" and "rest" periods by applying a threshold on the root-mean-square EMG signal. Threshold was defined manually.

This was done by calculating the z-score of ECoG power, at a specific frequency, against rest, defined as the running difference between ECoG power (P), at a given time point, and mean ECoG power at rest, divided by the standard deviation (SD) of ECoG power at rest:

$$z = \frac{P - \text{mean}(P_{rest})}{\text{SD}(P_{rest})}$$

The z-score of 2 normal distributions, in our case of power at times around the onset (or offset) of EMG activity and at rest, is a measure of their "separability", or distance between their means in units of the

SD of one of them. Time-frequency maps were generated by averaging ECoG power z-score vectors after aligning them at EMG-onset and EMG-offset triggers.

Correlations among ECoG features and among EMG signals

In order to examine whether there are ECoG features that are highly correlated, correlation coefficients (CCs) were computed among the time-courses of all ECoG features. Those included CCs among ECoG power across all frequency ranges, on the same ECoG electrode, and CCs among ECoG power across all ECoG electrodes, for a given frequency range. CCs were finally computed among the time-courses of all RMS-EMG signals.

ECoG-EMG regression

Linear regression was used to build a multi-variate predictive model of ECoG power and phase features on each of the EMG signals. Because of the presence of multicollinearity among ECoG features partial least squares (PLS) regression was performed (Abdi 2010). PLS finds the direction in the predictor (ECoG features) space that explains the maximum variance direction in the response (EMG activity) space. The Matlab Statistics Toolbox function ‘plsregress’ was used, which is based on a method described in (de Jong 1993).

In order to determine the number of PLS components that provide an optimal fit to the EMG data, PLS models of various numbers (2 to 10) of PLS components were generated from various lengths sections (1 to 10 minutes) of recording sessions. Mean squared error (MSE) was calculated, using 10-fold cross-validation, on data from the same recording session (Mosteller 1948). MSE values from each of the models with different numbers of PLS components were then correlated to the number of PLS components, as well as to the length of the section used to compute the PLS model. The number of PLS components and the section duration associated with the minimum MSE were used to compute PLS models. We found that 6 PLS components and a minimum training duration of 3 minutes were associated with minimum MSEs in all three arrays.

Training and testing of ECoG-EMG decoders

For each EMG signal, 10 linear decoders were computed from 10 randomly selected 3-minute-long, continuous segments, from a given recording session (the “training sets”).

$$B_i = \mathrm{plsregress}(f_{ECoG}, EMG_i)$$

Where B_i is the regression matrix, f_{ECOG} are the ECoG features and EMG_i is the actual EMG signal.

Each decoder was then tested on unused data from the same recording session as the training set, or on entire recording sessions from subsequent or preceding days (the “testing sets”).

$$rEMG_i = f'_{ECoG} \times B_i$$

Where $rEMG_i$ is the reconstructed EMG signal and f'_{ECoG} are the ECoG features of the test recording.

When the training and testing sets were from different recording sessions, features that were not present on both sessions (e.g. different “noisy” ECoG channels on different days) were removed during the evaluation of the decoders. The interval, in days, between the session used for the training set and the session used for the testing set, as well as the age of the cortical implant at the time of recording of the training set session were registered.

In each case, the resulting reconstructed EMG (rEMG) signal was compared to actual EMG by computing the CC, the percent variance explained (R^2) and the root mean square error (RMSE) between rEMG and EMG, henceforth termed quality of reconstruction (QoR) measures:

$$CC_i = \mathrm{corrcoef}(EMG'_i, rEMG'_i)$$

$$R_i^2 = CC_i^2$$

$$RMSE_i = \sqrt{(EMG'_i - rEMG'_i)^2}$$

Effect of ECoG derivation and ECoG-EMG time delay

The decoders were tested on data recorded on the same session as those used for their training with each of 2 ECoG signal derivations (unipolar re-referenced by the common average and Laplacian).

The decoders were also tested with each of a number of different ECoG-EMG time delays, that ranged between -2000 ms (EMG preceding ECoG) and 2000 ms (ECoG preceding EMG), in 50 ms steps. To normalize performance across different EMG signals and recording sessions, the CC between actual EMG and reconstructed EMG for each decoder at a given ECoG-EMG delay was divided by the CC of the same decoder with no ECoG-EMG delay.

Drop-channel and drop-feature analysis

In order to examine the relative contribution of ECoG channels and ECoG features to decoding accuracy, QoR measures were calculated for decoders that were trained with increasingly less ECoG channels or with all but one ECoG features, and tested on data recorded on the same day. The order at which ECoG channels were dropped from the training set was determined using a “best goes first” strategy, i.e. the channel whose dropping was associated with the largest reduction in QoR (while all others were used) was dropped first; the two “top-performing” channels were dropped next, etc. ECoG features were dropped one at a time, across all channels.

Effect of cortical surface coverage area

In order to determine whether the area of cortical surface coverage has an effect on QoR, we repeated the drop-channel analysis described above, this time consecutively dropping entire columns or rows, to compile QoR vs area relationships. To normalize performance across different EMG signals and recording sessions, a QoR measure for a given EMG signal derived from a partial array montage was divided by that derived from a full array montage, using data from the same training and testing sets.

Effect of electrode diameter

In order to determine whether exposed electrode diameter has an effect on QoR, independently of electrode density and the area covered by the arrays, we compared the decoding performance of montages of the mini-grid and the micro-grid array that were matched in electrode number and coverage area. The mini-grid array montage consisted of a contiguous 2x4-electrode array section; that section covered an area of 25 mm^2 (approximately the same area as a micro-grid) and included 8 electrodes. A total of 12 mini-grid montages were considered, which is the maximum number of different contiguous 2x4 sections that can fit in the 4x8 array. The micro-grid array montage consisted of 8 (out of the 32) electrodes; each of those 8 electrodes was randomly selected among a group of four neighboring electrodes in the original array (Figure 6). A total of 50 different micro-grid montages were considered. Decoders were then trained using these mini-grid and micro-grid montages, from data recorded at 4 similar implant ages for both arrays (at about 15 days, 55 days, 80 days and 110 days post-implant), against muscles that were implanted on both the left and right arm of monkey X (pectoralis major, deltoid, biceps, and triceps). For each pair of recording sessions with the 2 arrays, matched for implant age, a total of 12 mini-grid decoders and 50 micro-grid decoders per muscle were generated.

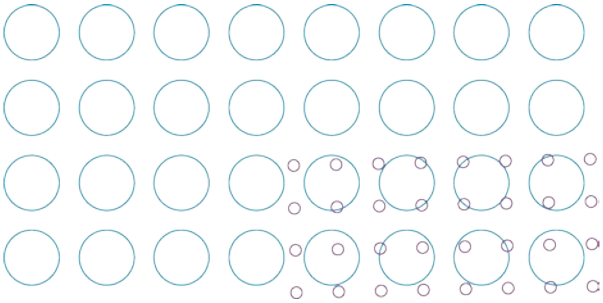

Figure 7. The 2 types of subdural arrays (mini-grid, micro-grid), overlaid. The cortical surface covered by 1 mini-grid electrode roughly corresponds to that covered by 4 micro-grid electrodes.

Effect of training-testing interval and implant age

In order to determine what the impact of the time interval between the training and the testing set was on QoR, CC between actual and reconstructed EMG, for a given EMG signal, associated with a certain train/test set interval was divided by that CC, for the same EMG signal, when the test set came from the same recording session as the train set. This was done separately for each electrode array. A similar approach was followed to test the effect of implant age on decoding performance, comparing that to the decoding performance at the earliest time data were recorded for each array.

Results

A total of 16 recording sessions were performed with monkey C, with the micro-grid array, between 3 weeks and 5 months after the array's implantation. With monkey X, 19 sessions involved the mini-grid array (2 weeks to 6 months post-implantation), and 27 sessions involved the micro-grid array (2 weeks to 4 months post-implantation).

ECoG changes related to onset and offset of muscle activity

EMG activity was associated with ECoG signal changes that were different for different ECoG frequencies, and were visible in single trials. For example, power in the beta range (15-25 Hz) was higher during periods of rest and suppressed during periods of increased EMG activity, whereas power in the high gamma range (70-100 Hz) exhibited the opposite behavior (Figure 7).

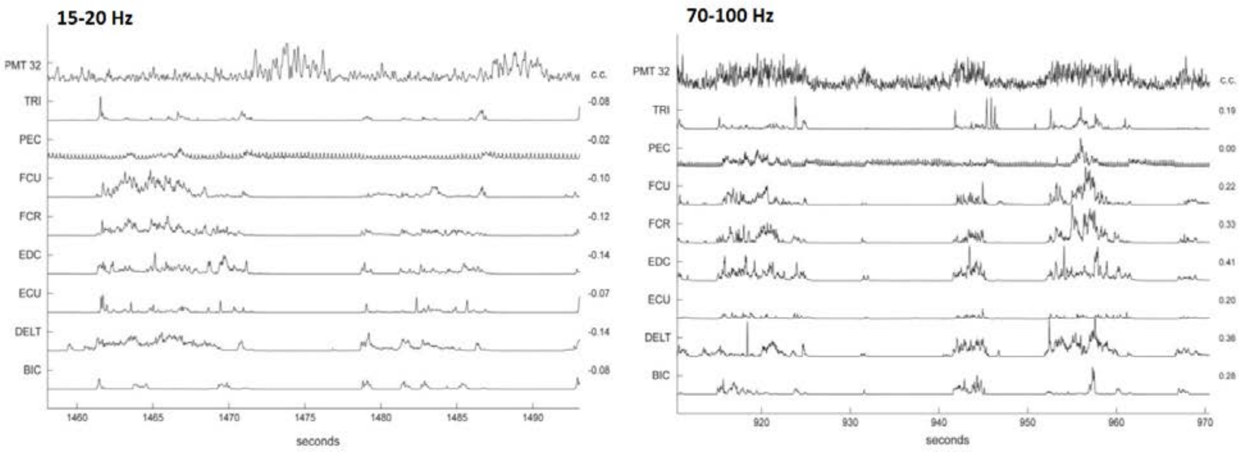

Figure 8. Example of ECoG power changes associated with EMG activity and rest. (Left) Time course of Laplacian-derived ECoG power in the beta range (15-25 Hz) from a micro-grid electrode, shown in the top row, and of simultaneously recorded EMGs from a number of contralateral upper extremity muscles. Next to each EMG signal, the correlation coefficient between EMG and beta ECoG power is shown. (Right) Time course of power in high gamma range (70-100 Hz) from the same micro-grid electrode and of EMGs from the same muscles, during a different segment of the recording.

In all three arrays, ECoG on many electrodes displayed a stereotypical pattern of ECoG changes with the onset and ending of muscle activity. For example, in the mini-grid, low frequency (LF) components, i.e. <10 Hz, and high frequency (HF) components, i.e. >30 Hz, increased in power up to 300 ms before the onset of EMG activity, whereas intermediate frequencies (IF), i.e. 12-25 Hz, decreased in power before EMG onset (Figure 8). Similar ECoG changes were seen in the micro-grid recordings as well (Figure 9). On some channels, IF exhibited a rebound starting at around 200-300 ms after the end of EMG activation (Figure 10).

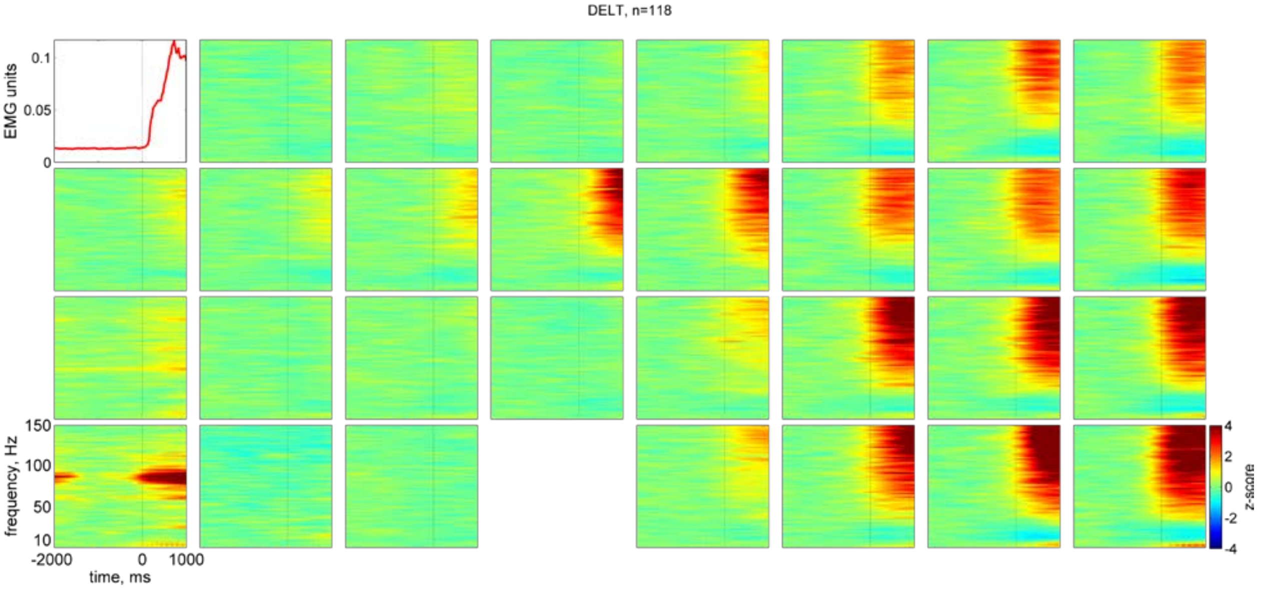

Figure 9. Time-frequency plot of average ECoG power changes associated with onset of contraction of the contralateral deltoid; ECoG was recorded with a mini-grid array covering a large part of the sensorimotor cortex (see inset at bottom of figure), 2 weeks after implantation. Each panel represents an electrode of the array. In each map, warm colors denote increase in power relative to a "resting baseline", cold colors denote decrease; power changes are shown in z-score units. (Top-left inset) Average of deltoid EMG around the onset of contraction. A total of 118 "onset triggers" were used to compile the EMG average, as well as each average map.

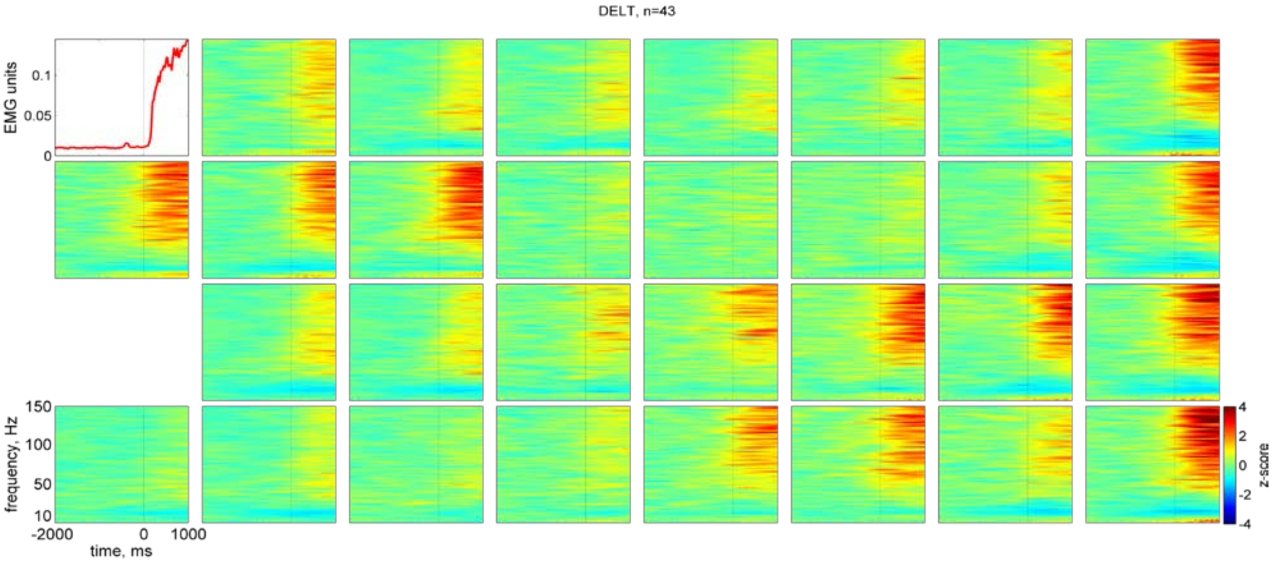

Figure 10. Time-frequency plot of average ECoG power changes in the micro-grid array, associated with onset of contraction of the contralateral deltoid. Each panel represents an electrode of the array. In each map, warm colors denote increase in power relative to a "resting baseline", cold colors denote decrease; power changes are shown in z-score units. (Top-left inset) Average of deltoid EMG around the onset of contraction. A total of 43 "onset triggers" were used to compile the EMG average, as well as each average map.

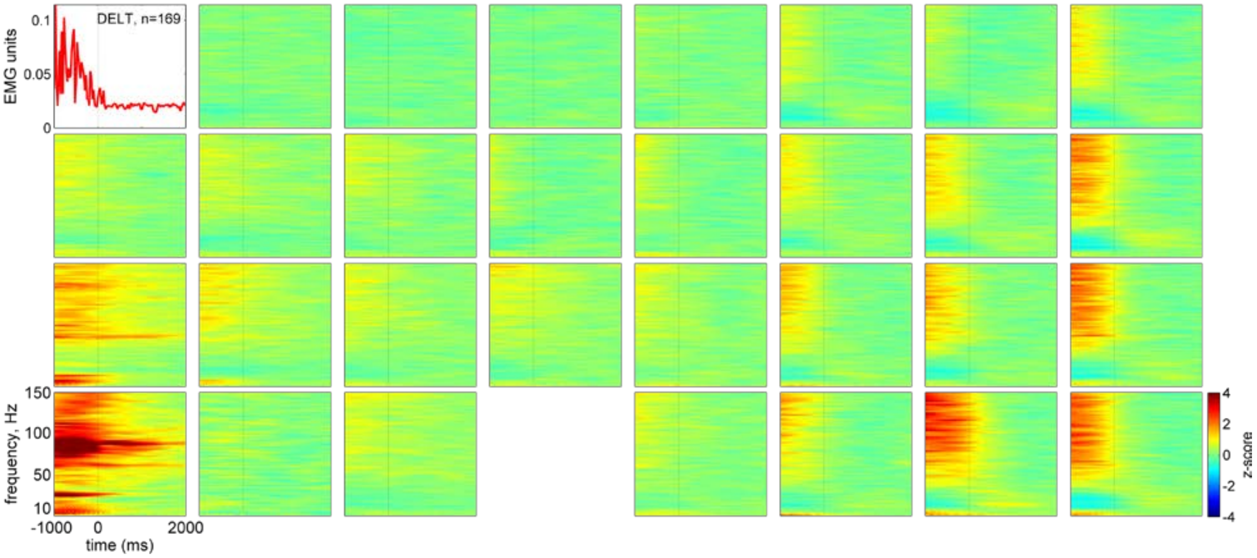

Figure 11. Time-frequency plot of average ECoG power changes associated with the ending of contraction of the contralateral deltoid; ECoG was recorded with a mini-grid array covering a large part of the sensorimotor cortex (see inset at bottom of figure??), 2 weeks after implantation. Each panel represents an electrode of the array. In each map, warm colors denote increase in power relative to a "resting baseline", cold colors denote decrease; power changes are shown in z-score units. (Top-left inset) Average of deltoid EMG around the end of muscle contraction. A total of 169 "end triggers" were used to compile the EMG average, as well as each average map.

Time-frequency maps of ECoG activity associated with onset of EMG activity on different muscles were similar. For example, the T-F map for deltoid activation (Figure 8) was very similar to that for APL activation (Figure 11), even though those two muscles exhibited little co-contraction (CC between deltoid and APL EMG was 0.34) (Figure 12).

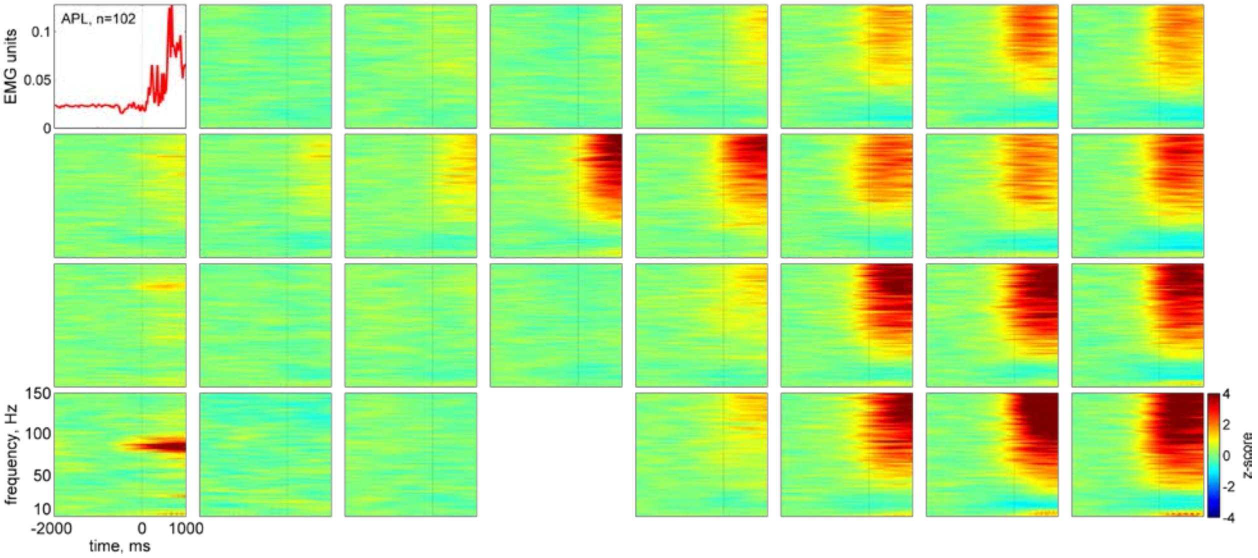

Figure 12. Time-frequency plot of average ECoG power changes associated with onset of contraction of the contralateral APL; ECoG was recorded with a mini-grid array covering a large part of the sensorimotor cortex (see inset at bottom of figure??), 2 weeks after implantation. Each panel represents an electrode of the array. In each map, warm colors denote increase in power relative to a "resting baseline", cold colors denote decrease; power changes are shown in z-score units. (Top-left inset) Average of APL EMG around the onset of contraction. A total of 102 "onset triggers" were used to compile each average map.

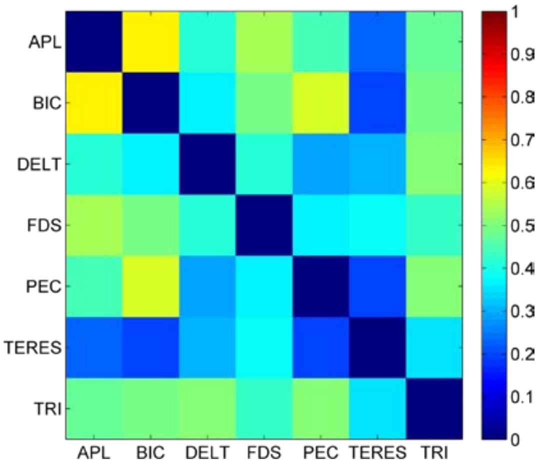

Figure 13. Correlation coefficients between EMG signals recorded from the right upper extremity of monkey X (contralateral to a mini-grid).

Movement-related ECoG changes depended on the implant's age. Several months after implantation, the stereotypical pattern of LF/IF/HF power changes with movement was still present, but the modulation of power in each frequency range with movement was much smaller than early after implantation (Figure 13).

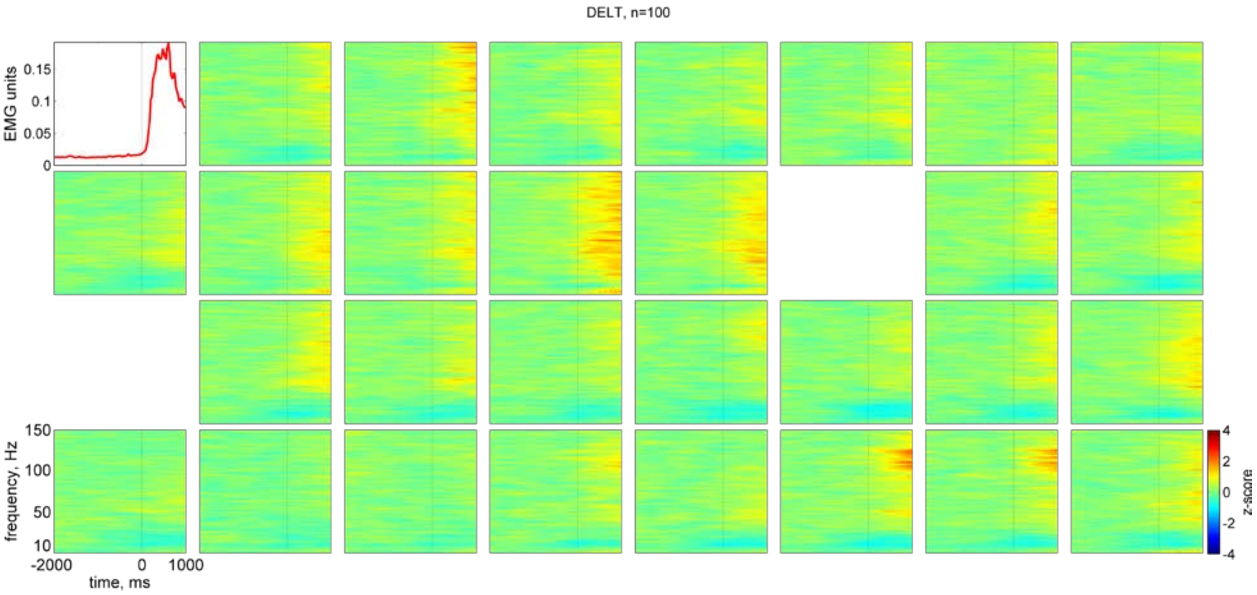

Figure 14. Time-frequency plot of average ECoG power changes in the mini-grid array, associated with onset of contraction of the contralateral deltoid, 5 months after implantation.

Correlations between ECoG power and EMG activity

There were variable degrees of linear correlation between power in different frequency ranges of ECoG from a given electrode and EMG activity across the various muscles. For example, correlation coefficients between power in the beta range (15-25 Hz) and EMG on most muscles were negative (Figure 7, left panel), and that was true for many electrodes in the array (Figure 14). In contrast, power in the high gamma range (70-100 Hz) was positively correlated with EMG activity (Figure 7, right panel); that was the case for most array electrodes (Figure 15). The correlation of EMGs with high gamma was stronger than that with beta (compare the CC scales in (Figure 14) and (Figure 15). By normalizing individual CCs by the maximum CC on a given electrode, we found that ECoG-EMG relationships on an electrode are simply scaled versions of those of many other electrodes (Figure 16).

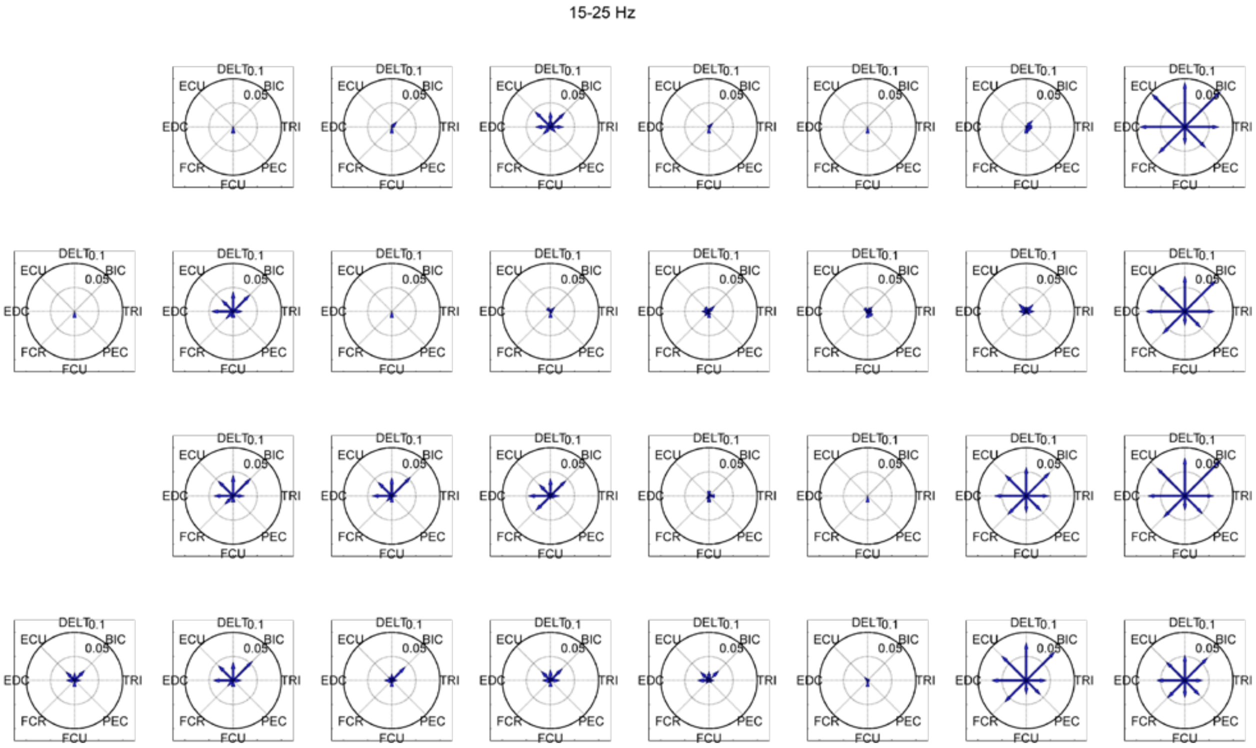

Figure 15. Correlations between beta range ECoG power on a micro-grid array and EMGs from contralateral upper extremity muscles. Panels represent the location of array electrodes, as arranged on the cortical surface. In each panel, arrows represent the (negative) correlation coefficients between beta (15-25 Hz) ECoG power on that electrode and each of 8 EMG signals. Longer arrows are associated with more negative CCs.

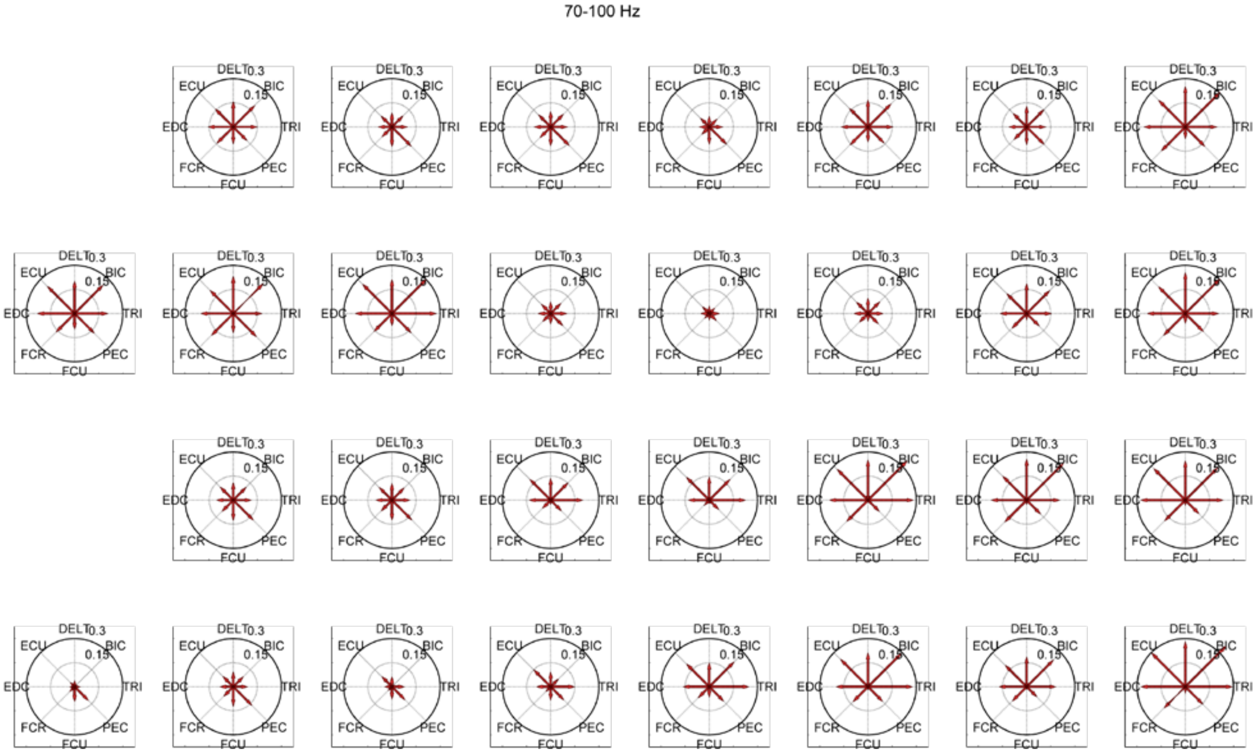

Figure 16. Correlations between high-gamma range ECoG power on a micro-grid array and EMGs from contralateral upper extremity muscles. Panels represent the location of array electrodes, as arranged on the cortical surface. In each panel, arrows represent the (positive) correlation coefficients between high gamma (70-100 Hz) ECoG power on that electrode and each of 8 EMG signals. Longer arrows are associated with larger CCs. Notice the difference in scale between high-gamma and beta CCs (shown in the previous figure).

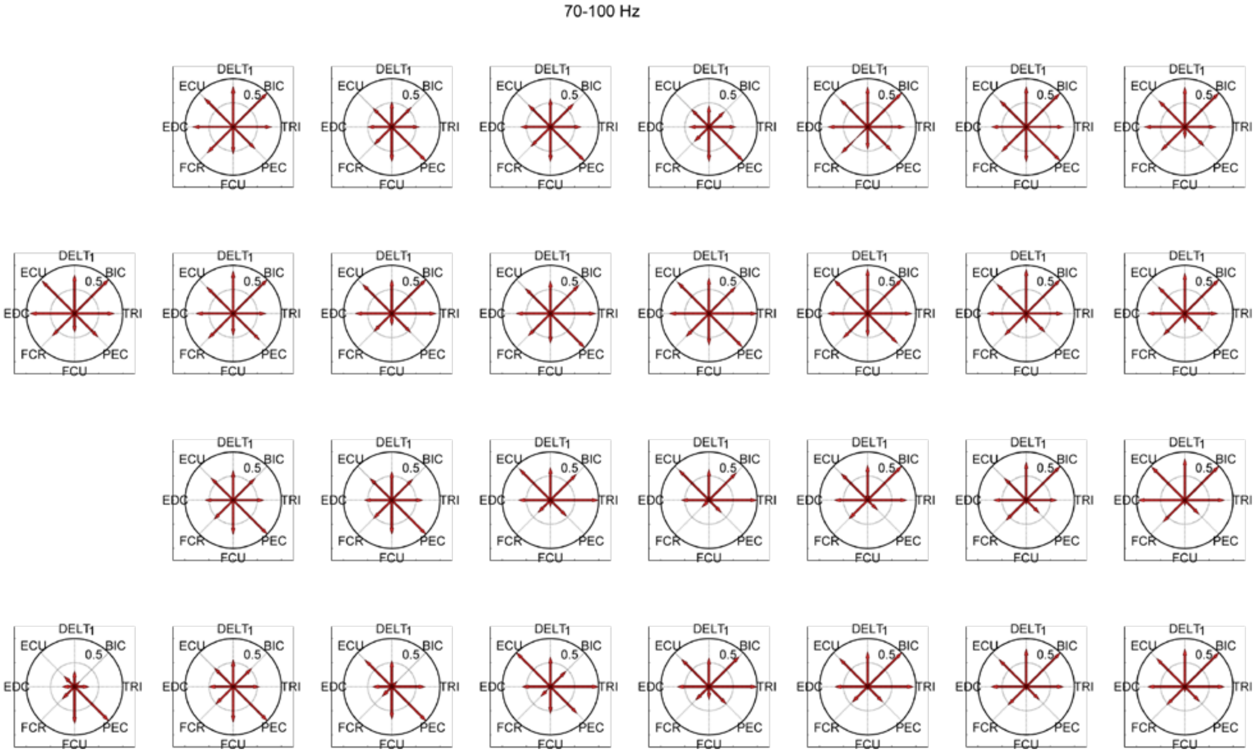

Figure 17. Normalized correlations between high-gamma range ECoG power and EMGs from contralateral upper extremity muscles. Panels represent the location of array electrodes, as arranged on the cortical surface. In each panel, arrows represent the (positive) correlation coefficients (CCs) between high gamma (70-100 Hz) ECoG power on that electrode and each of 8 EMG signals, normalized by the maximum CC on that electrode. ECoG-EMG relationships on an electrode are simply scaled versions of those of many other electrodes.

Correlations among ECoG power features

The time courses of power at different frequencies of ECoG recorded on a given electrode of the micro-grid were correlated, at varying degrees (Figure 17, Figure 18). The time course of the local motor potential was correlated with that of LF (<10 Hz) power, while the time course of LFs was positively correlated with that other neighboring frequencies in the LF range, as well as that of power of HFs. Frequencies in the HF range were positively correlated to each other. The time course of power in IFs (12-25 Hz) was weakly anti-correlated with that of all other frequencies.

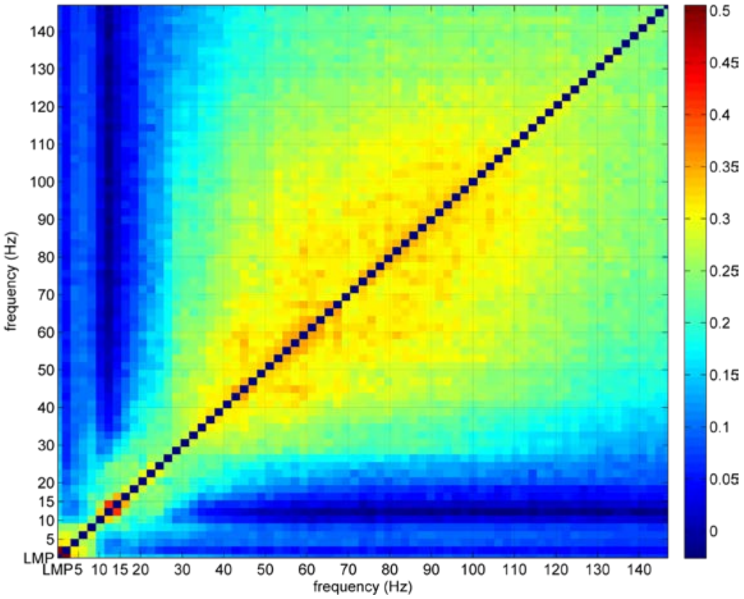

Figure 18. Correlation coefficients (CC) between time series of ECoG power at different frequencies, on the same electrode, in a micro-grid array. Average CC across all electrodes of the micro-grid array of monkey X, calculated over 10 recording sessions. LMP: local motor potential.

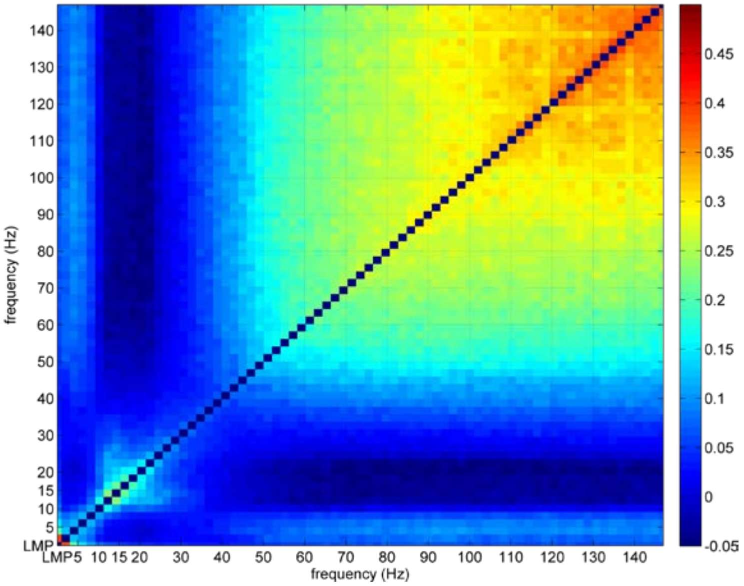

Figure 19. Correlation coefficients (CC) between time series of ECoG power at different frequencies, on the same electrode, in a mini-grid array.

ECoG power at a given frequency was correlated across different electrodes, in both the micro-grid (Figure 19) and the mini-grid (Figure 20). Interestingly, CC values were similar between the 2 types of arrays, despite their different inter-electrode distances. These findings suggest that there is significant co-linearity between ECoG features, at a given frequency, across electrodes.

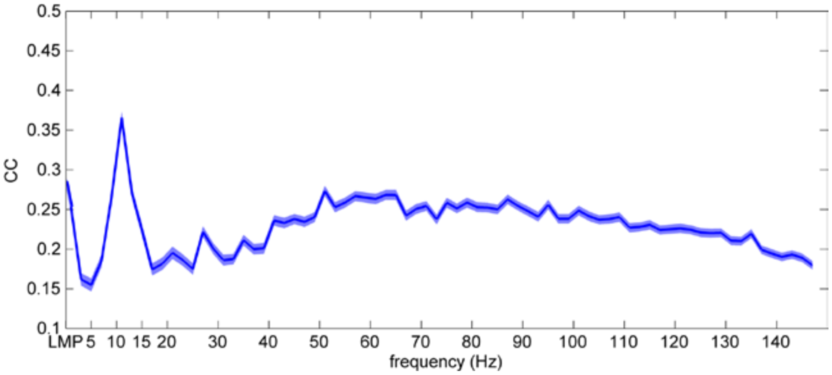

Figure 20. Correlation coefficients (CC) between time series of ECoG power at a given frequency across different electrodes of a micro-grid array. Average (+/- SD) CC across all electrode combinations of the micro-grid array of monkey X, calculated from 10 recording sessions. LMP: local motor potential.

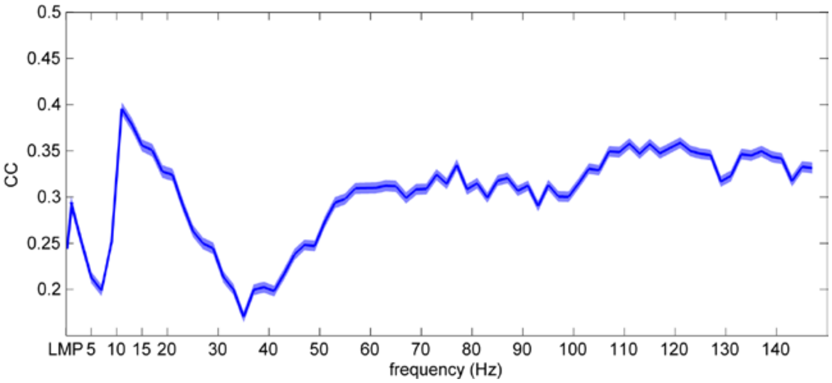

Figure 21. Correlation coefficients (CC) between time series of ECoG power at a given frequency across different electrodes of a mini-grid array. Average (+/- SD) CC across all electrode combinations of the mini-grid array of monkey X, calculated from 10 recording sessions. LMP: local motor potential.

Correlations among EMG signals

Correlation coefficients among different EMG signals ranged between 0.05 and 0.6 for the left arm of monkey X (contralateral to a micro-grid) (Figure 21), between 0.12 and 0.62 for the left arm of monkey X (contralateral to a mini-grid) (Figure 12) and between 0.1 and 0.68 for the left arm of monkey C (contralateral to a micro-grid) (Figure 22).

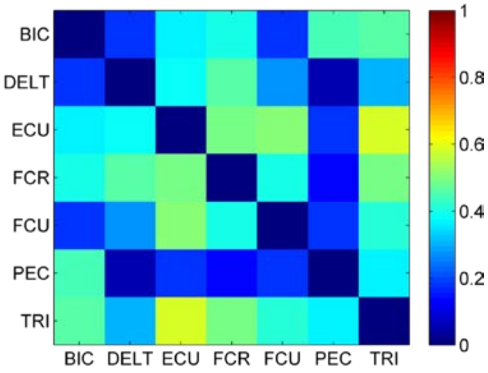

Figure 22. Correlation coefficients between EMG signals recorded from the left upper extremity of monkey X (contralateral to a micro-grid).

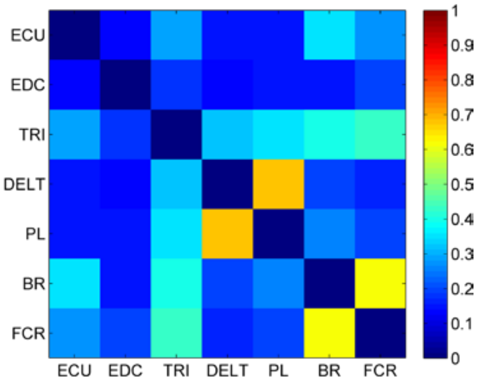

Figure 23. Correlation coefficients between EMG signals recorded from the left upper extremity of monkey C (contralateral to a micro-grid).

Decoding of EMG activity

Decoders trained with short segments of simultaneous ECoG-EMG data were able to reconstruct contralateral? EMG activity from ECoG recorded at a different time. EMG signals from different muscles were reconstructed at different levels of fidelity (Figure 23). Decoder performance was higher for distal muscles than for proximal muscles, but that difference did not reach statistical significance: across all 3 arrays, average CC for proximal muscles was 0.69, and for distal muscles 0.71 (p=0.02). The average peak CC value was 0.73 (range 0.61-0.88) for the mini-grid in monkey X, 0.74 (range 0.64-0.81) for the micro-grid in monkey X, and 0.54 (range 0.42-0.64) for the micro-grid in monkey C.

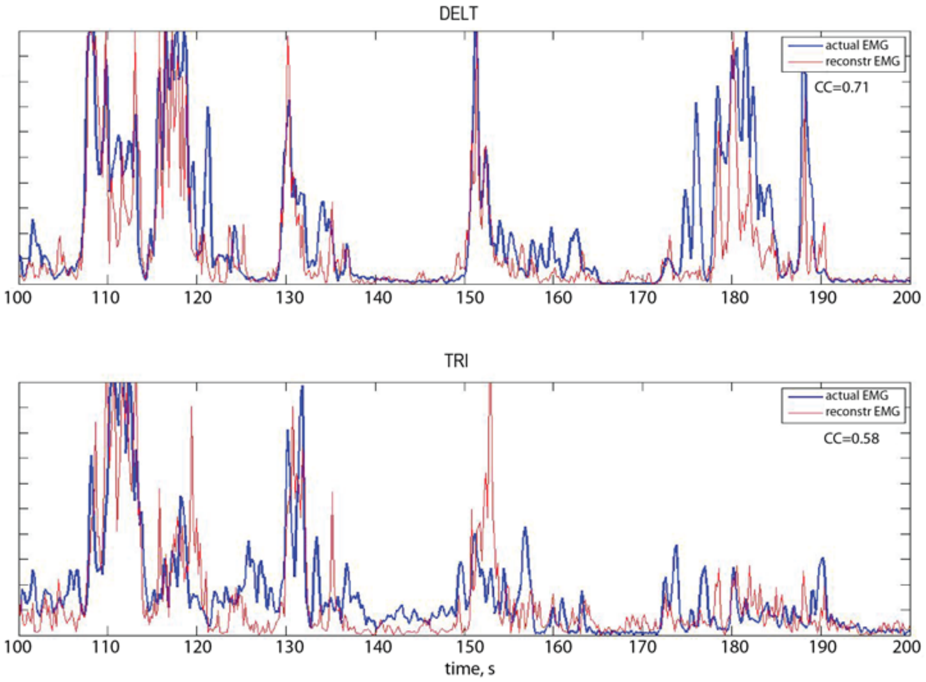

Figure 24. Example of decoding of EMG activity from 2 upper extremity muscles from contralateral ECoG signals recorded by a mini-grid array. Training of these 2 decoders was performed with data recorded approximately 1 month after implantation of the array, and testing with data recorded 1 week after their training.

Effect of signal derivation

There was no effect of the type of signal derivation (unipolar with common average re-referencing or Laplacian) on decoder performance. The mean difference in RMSE between the two derivations for the mini-grid in monkey X was 1.2±0.16% (*p*=0.34), for the micro-grid in monkey X was 1.7±0.19% (*p*=0.29) and for the micro-grid in monkey C was 1.46±0.17% (*p*=0.26).

Effect of ECoG-EMG delay

Decoder performance depended on the delay between ECoG and EMG signals. For the mini-grid array in monkey X, the optimal delay was ECoG preceding EMG by 50-100 ms (Figure 24). For the micro-grid in monkey X optimal performance was attained when ECoG preceded EMG by 50-100 ms and for the micro-grid in monkey C when ECoG preceded EMG by 100-200 ms.

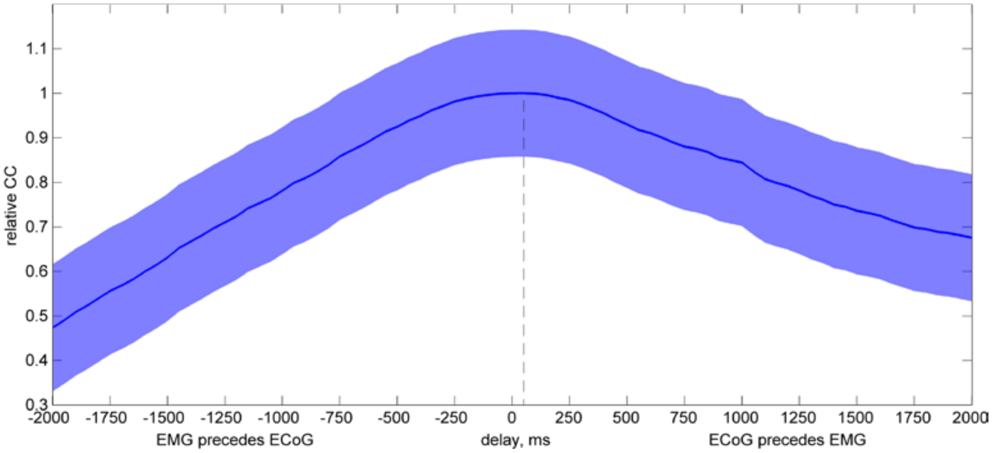

Figure 25. Effect of ECoG-EMG delay on decoder performance, for the mini-grid array in monkey X. Correlation coefficient (CC) between actual EMG and reconstructed EMG for a decoder at a given ECoG-EMG delay was divided by the CC of the same decoder for no EMG-ECoG delay. Those relative CCs were then averaged across all decoders, for recordings involving the mini-grid array. Shown is the mean(+/- 2SD) relative CC as a function of ECoG-EMG delay (negative delays: EMG precedes ECoG, positive delays: ECoG precedes EMG). There was a significant effect of delay on CC (p<0.005); CCs between -50 and 250 ms were significantly higher than CCs at all

other delays (p values between <0.01 and p<0.007). Peak performance was attained at a delay of +50ms (dashed line)

Contribution of ECoG features to decoding

In all arrays, dropping of any one of the 7 ECoG features per channel used in the decoders was associated with a reduction in decoder performance, seen as an increase in the RMSE between the actual and reconstructed EMG activity (Figure 25). Among the 7 features, power in the high gamma range (70-100 Hz) was the feature whose dropping was associated with the largest increase in RMSE, and therefore the one that contributed the most to decoder performance, in all arrays. In contrast, the LMP was the feature that contributed the least to decoder performance, again, in all arrays.

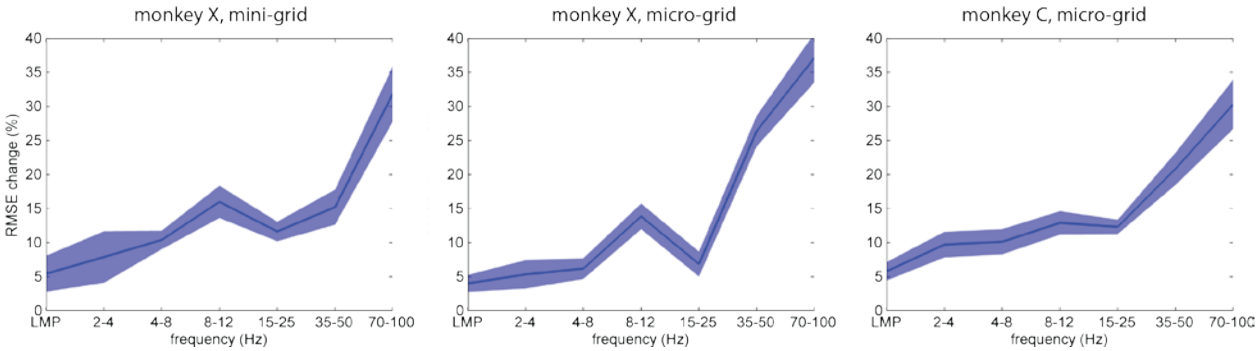

Figure 26. Change in root mean square error (RMSE) of EMG reconstruction when each of 7 ECoG features is dropped from the decoders, from the case when all 7 features are used. Average (+/-SD) change was calculated across all decoders. In all three array types, dropping of the high-gamma (70-100 Hz) feature was associated with the largest increase in RMSE (p<0.001) and of the local motor potential with the smallest (p<0.01).

Effect of channel count

As expected, increasing the number of ECoG channels included in the decoder had a positive impact on decoder performance, in all three arrays (Figure 26). Interestingly, increasing the number of included channels beyond 15 had minimal effect. It should be noted, however, that those were the 15 "best performing" channels.

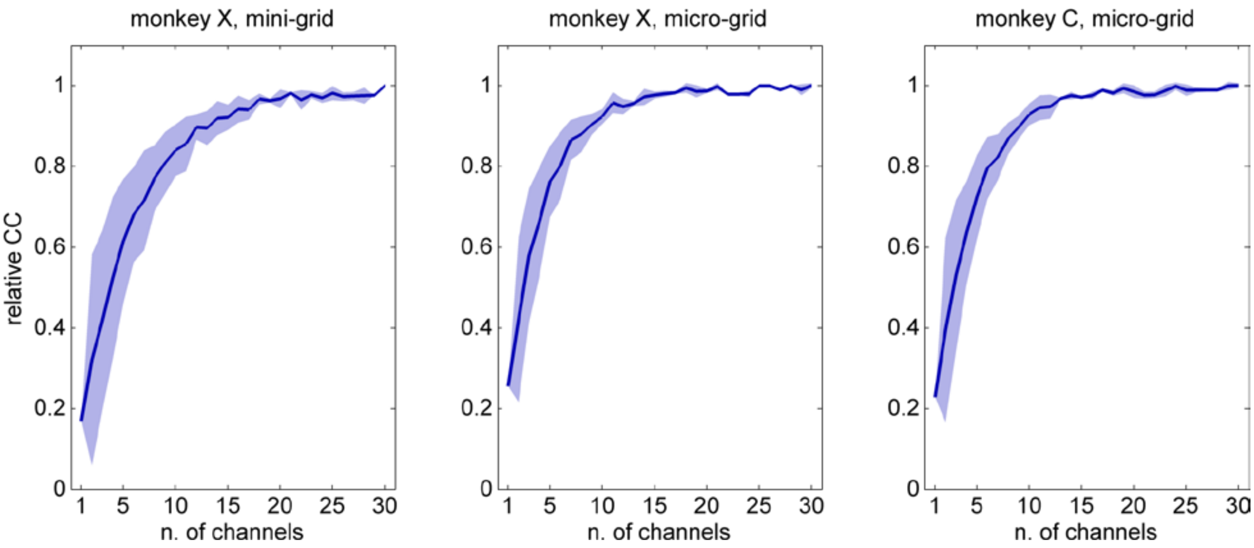

Figure 27. Impact of increasing the number of ECoG channels on decoder performance. Shown is the mean (+/-SD) of the CC between actual and reconstructed EMG for a given decoder, normalized by the CC when all 30 channels are used in that decoder, averaged across all decoders for each array.

Effect of array surface area

The presence of 2 types of arrays over symmetric locations in the 2 hemispheres of monkey X allowed us to directly compare the effect of a number of geometric features of the arrays on decoder performance.

By considering increasingly larger sections of the entire array we found that decoder performance was proportional to the extent of cortical coverage. For the micro-grid array, that relationship was overall linear, but that linearity was interrupted by 4 peaks that corresponded to sections of the array with the largest possible medio-lateral length (the length of the entire array) (Figure 27). For the, larger, mini-grid array decoder performance increased rapidly with increasing coverage up to an area of 70 mm^2; beyond that level, only moderate increases in performance occurred (Figure 28). We then examined separately the effect on decoder performance of increasing the medio-lateral length (parallel to the central sulcus) of the rectangular area covered and of increasing the postero-anterior width (perpendicular to the central sulcus). Increasing either dimension led to improved decoder performance, for both the micro-grid (Figure 29) and the mini-grid array (Figure 30). However, in both arrays, increasing M-L length was more effective than increasing A-P width (Figure 31) and (Figure 32). Furthermore, in the mini-grid array, increasing the M-L length beyond 11-12 mm and the A-P width beyond 5 mm offered little improvement in decoder performance (Figure 32), whereas that relationship in the micro-grid array was more linear (Figure 31).

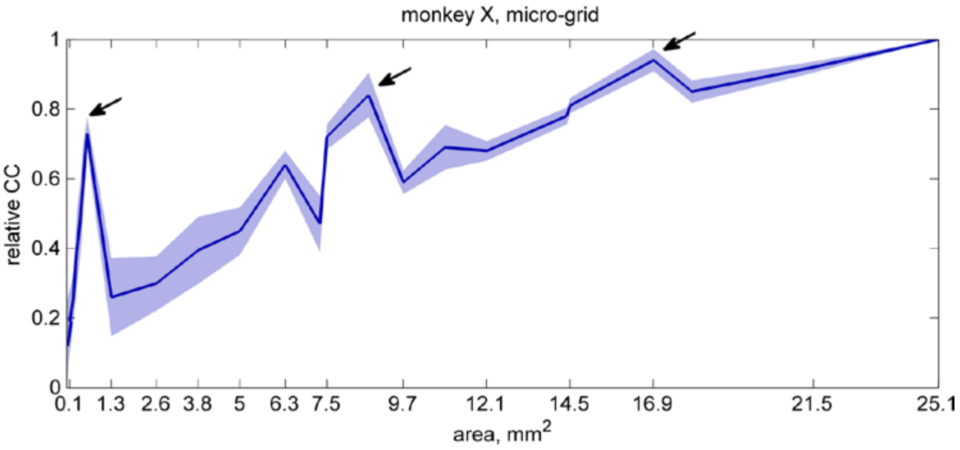

Figure 28. Impact of area of cortical coverage on decoder performance, for the micro-grid array. Shown is the average (+/- SD) ratio of the correlation coefficient (CC) (between actual and reconstructed EMG) for a given area of contiguous cortical coverage to the CC for the maximum coverage. For many coverage area values there were multiple array sections that fit within the overall mini-grid array, thus the need for calculating mean CC values. The arrows pointing at local maxima, denote coverage area values that correspond to 8-electrode-long (longest) array sections. The left-most maximum corresponds to an array section with a width of 1 row of electrodes, the second to a section with 2 rows, etc. The right-most maximum (CC=1) corresponds to the full array.

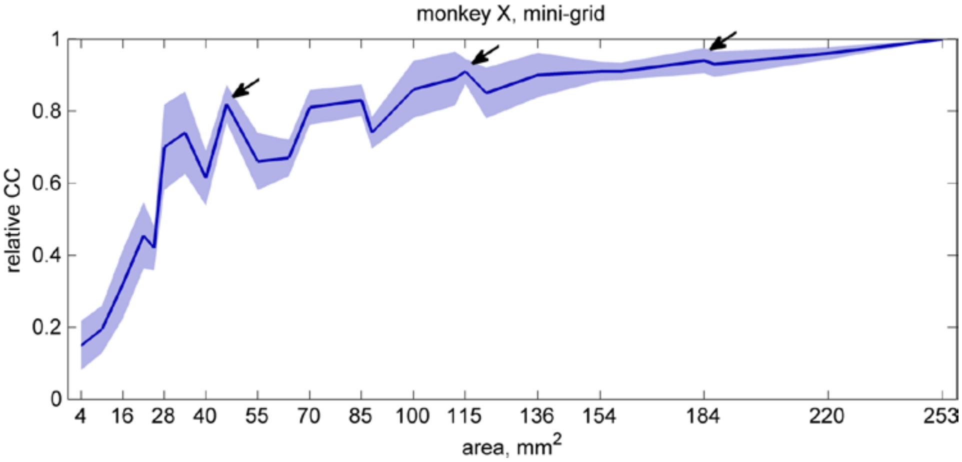

Figure 29. Impact of area of cortical coverage on decoder performance, for the mini-grid array. Shown is the average (+/- SD) ratio of the correlation coefficient (CC) (between actual and reconstructed EMG) for a given area of contiguous cortical coverage to the CC for the maximum coverage. For many coverage area values there were multiple array sections that fit within the overall mini-grid array, thus the need for calculating mean CC values. The arrows pointing at local maxima, denote coverage area values that correspond to 8-electrode-long (longest) array sections. The left-most maximum corresponds to an array section with a width of 1 row of electrodes, the second to a section with 2 rows, etc. The right-most maximum (CC=1) corresponds to the full array.

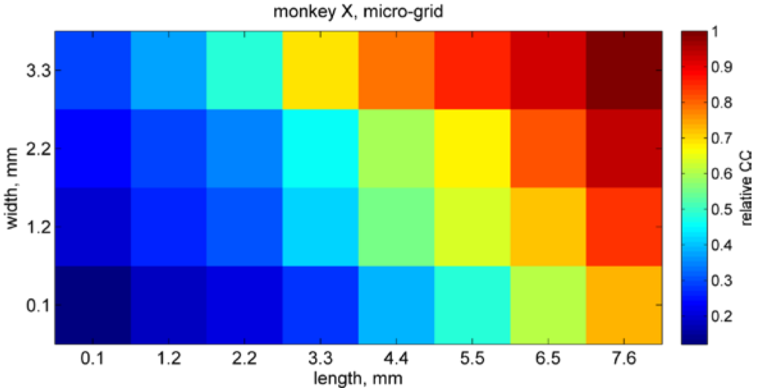

Figure 30. Impact of the length and width of the cortical area covered on decoder performance, for the micro-grid array. Performance is estimated by CC at a given combination of length and width, relative to CC at the full array, and is represented by the color scale. The longer or wider the array, the better the decoder performance.

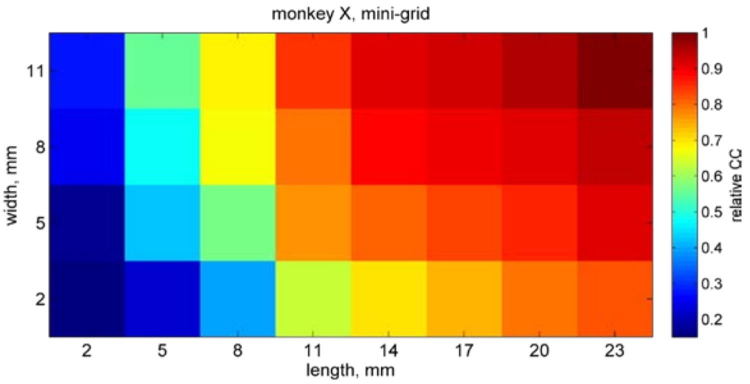

Figure 31. Impact of the length and width of the cortical area covered on decoder performance, for the mini-grid array. Performance is estimated by CC at a given combination of length and width, relative to CC at the full array, and is represented by the color scale. Notice that the CC increases rather abruptly beyond the array length of 11 mm, for all array widths.

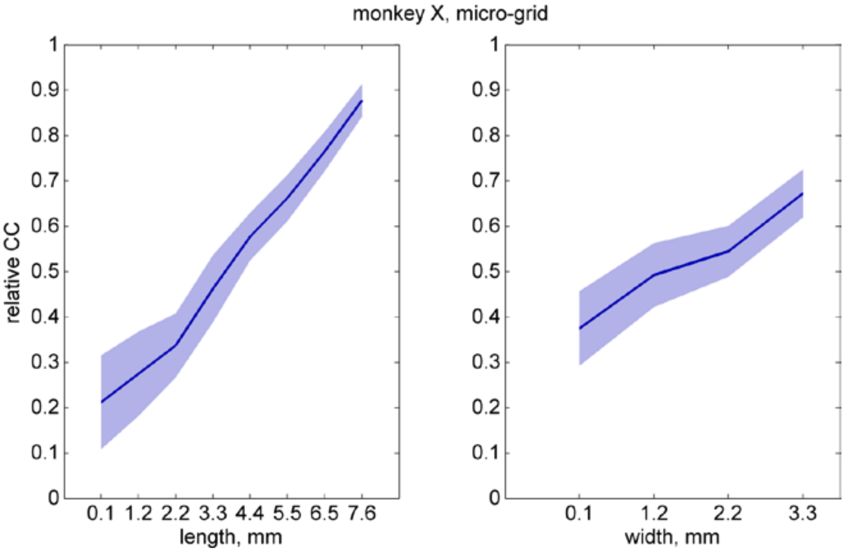

Figure 32. Impact of the length and width of the cortical area covered on decoder performance, for the micro-grid array. Performance for a given array length (left panel) is estimated by the average (+/- SD) CC associated with that length, across all width values, relative to CC associated with the full array; same for a given array width (right panel). Notice the almost linear increase of CC with length or width. As is the case with the mini-grid, increasing the length of the micro-grid has a larger impact on decoder performance than increasing the width.

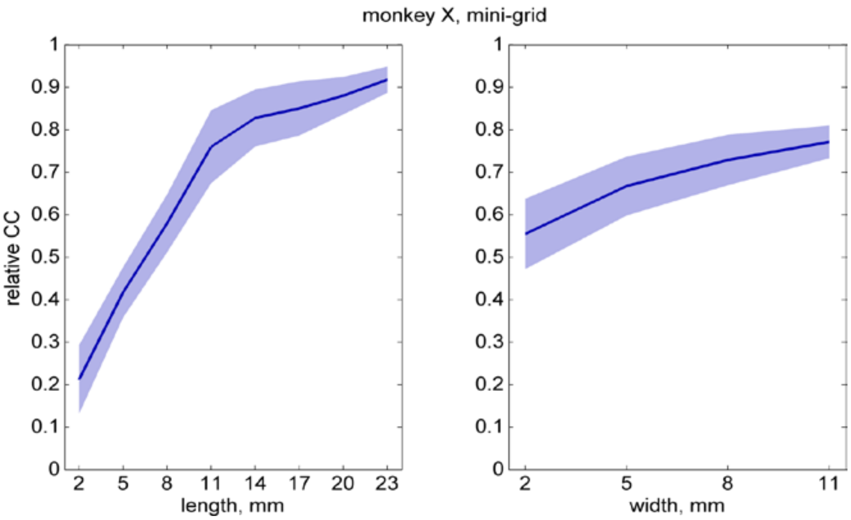

Figure 33. Impact of the length and width of the cortical area covered on decoder performance, for the mini-grid array. Performance for a given array length (left panel) is estimated by the average (+/- SD) CC associated with that length, across all width values, relative to CC associated with the full array; same for a given array width (right panel). Notice the steep increase of CC with length, up to 11-14 mm.

Effect of electrode diameter

We compared the decoder performance of the two types of arrays in monkey X, when an equivalent cortical area (5x11 mm) and the same electrode counts (8) were considered, across a range of implant ages. The micro-grid performed better than the mini-grid array in all 4 muscles examined; micro-grid's performance, in terms of CCs between actual and reconstructed EMG, was about 14% higher (Figure 33).

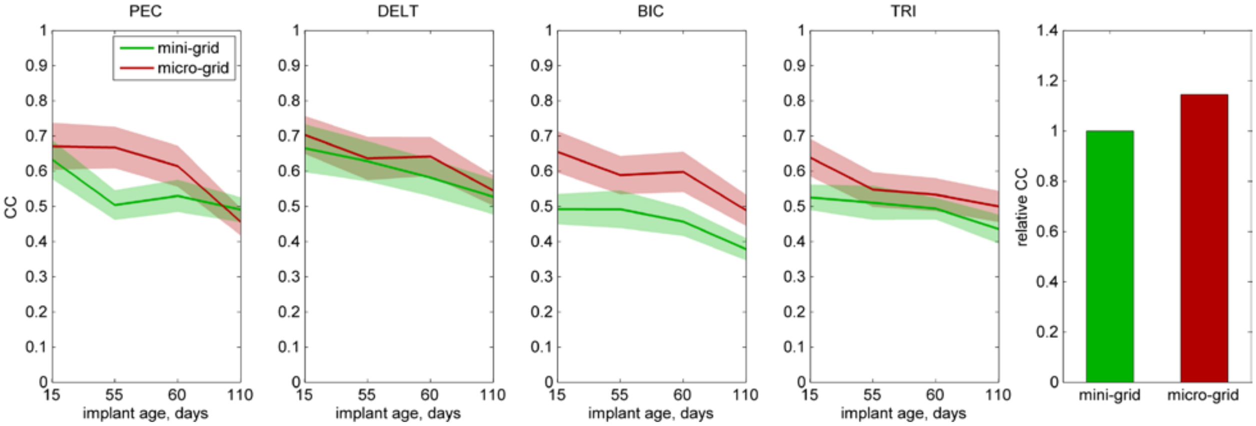

Figure 34. Effect of electrode diameter on decoder performance. Each of the four panels to the left shows decoder performance (mean+/-SD CC between actual and reconstructed EMG activity) of 12 mini-grid (exposed electrode diameter 1 mm) and 50 micro-grid (75 µm) area- and electrode count-matched montages, for each of 4 EMG signals that were common among mini-grid and micro-grid recordings. Performance was evaluated at 4 different implant ages (15, 55, 60 and 110 days after surgery). The far-right panel shows the performance of the micro-grid montages, normalized by that of the mini-grid montages, across all EMG signals and implant ages.

Effect of implant age

Depending on muscle, peak correlation coefficients between actual EMG and reconstructed EMG for decoders trained and tested with data recorded in the same session ("retraining") ranged between 0.64-0.89 for the mini-grid in monkey X (Figure 34), 0.66-0.82 for the micro-grid in monkey X (Figure 35), and 0.42-0.66 for the micro-grid in monkey C (Figure 36). Decoding performance after retraining was highest early after implantation and slowly declined thereafter. For the mini-grid in monkey X, it had decreased by 30% 140 days after it was first measured (Figure 34), whereas for the micro-grid in the same monkey, it had decreased by 25% 90 days after it was first measured (Figure 35). Finally, for the micro-grid in monkey C, it had decreased by 22% 140 days after it was first measured (Figure 36).

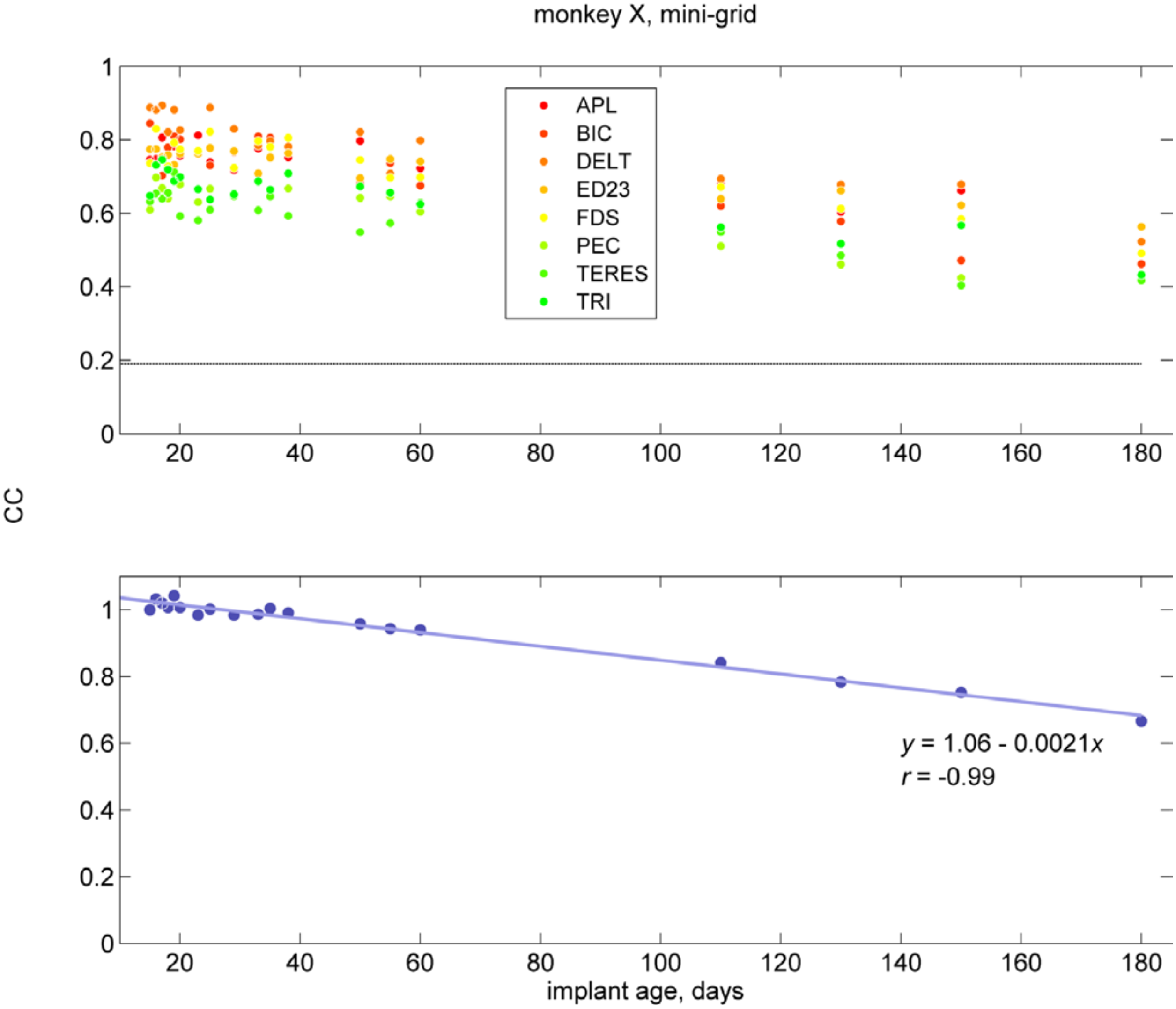

Figure 35. Performance of decoders trained and tested with data from the same recording session, at different implant ages, for mini-grid recordings with monkey X. (Top) Correlation coefficient between actual EMG and reconstructed EMG as a function of implant age, for different EMG signals. Each data point corresponds to the performance of one decoder, trained and tested on different data recorded on the same day. The dotted horizontal line denotes chance level. (Bottom) Average of CC at a given implant age, relative to CC at the earliest age after implantation, across all EMG signals. Also shown are the linear least-squares fit, its equation and the correlation coefficient between relative CC and implant age.

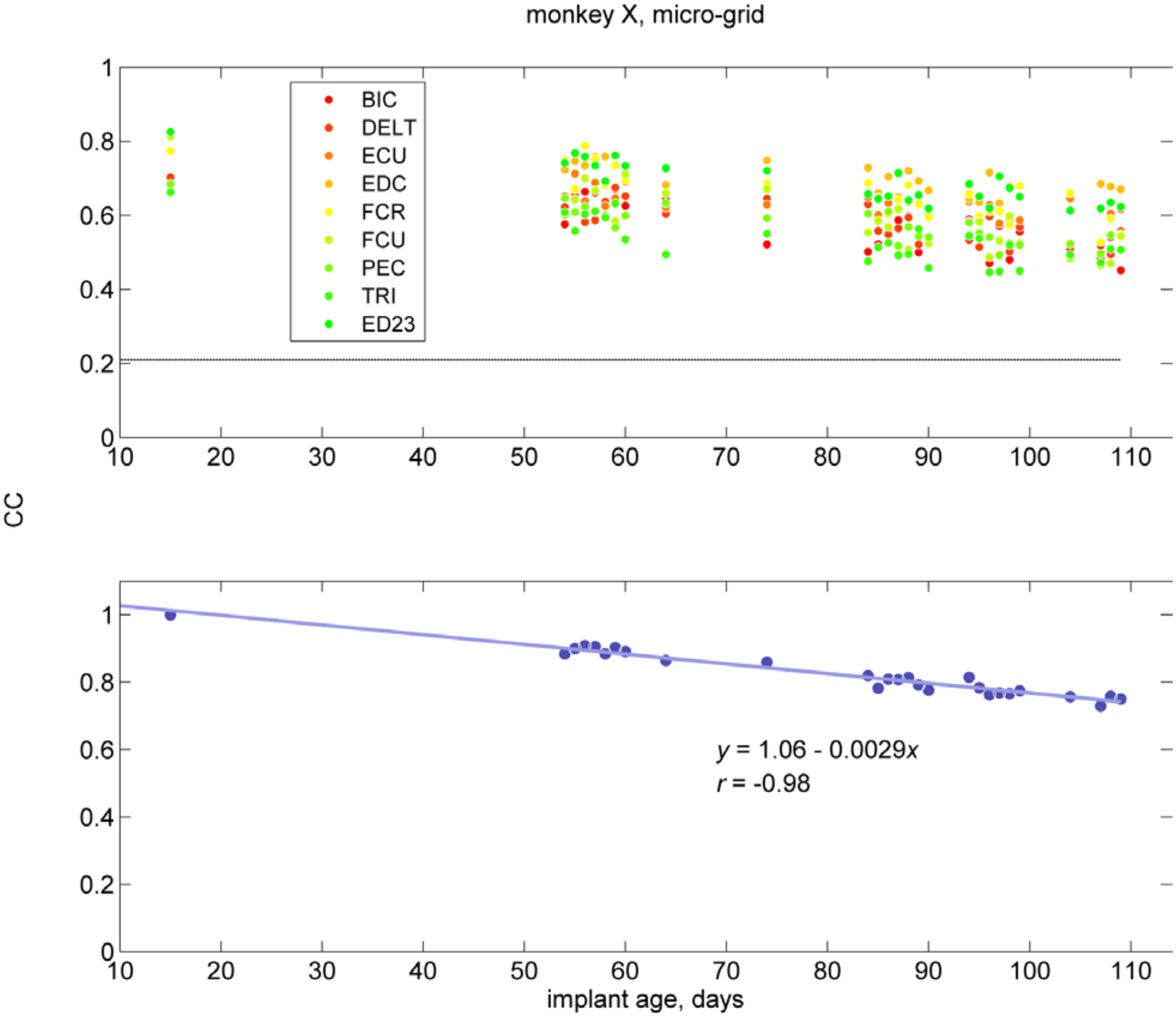

Figure 36. Performance of decoders trained and tested with data from the same recording session, at different implant ages, for micro-grid recordings with monkey X. (Top) Correlation coefficient between actual EMG and reconstructed EMG as a function of implant age, for different EMG signals. Each data point corresponds to the performance of one decoder, trained and tested on different data recorded on the same day. The dotted horizontal line denotes chance level. (Bottom) Average of CC at a given implant age, relative to CC at the earliest time after implantation, across all EMG signals. Also shown are the linear least-squares fit, its equation and the correlation coefficient between relative CC and implant age.

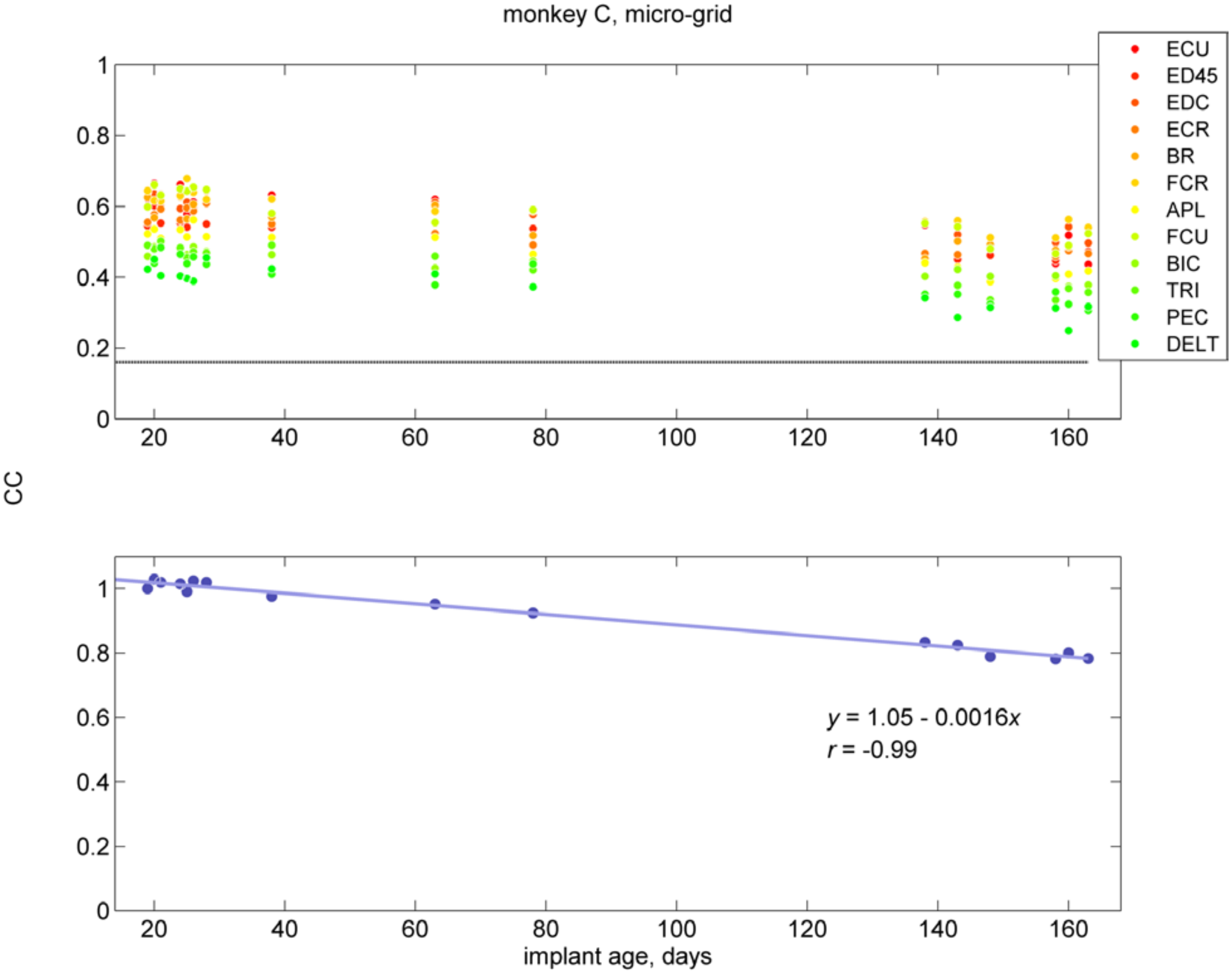

Figure 37. Performance of decoders trained and tested with data from the same recording session, at different implant ages, for micro-grid recordings with monkey C. (Top) Correlation coefficient between actual EMG and reconstructed EMG as a function of implant age, for different EMG signals. Each data point corresponds to the performance of one decoder, trained and tested on different data recorded on the same day. The dotted horizontal line denotes chance level. (Bottom) Average of CC at a given implant age, relative to CC at the earliest time after implantation, across all EMG signals. Also shown are the linear least-squares fit, its equation and the correlation coefficient between relative CC and implant age.

Decoder performance and test-train interval

Decoding performance was inversely proportional to the interval between the train and test sets. Highest performance was attained when training and testing was done on different data from the same recording session (interval of 0 days); it declined by increasing the interval between the train and the test set. It reached chance-levels after 50-60 days for the mini-grid in monkey X (Figure 37), after 35-40 days for the micro-grid in monkey X (Figure 38), and after 40-60 days for the micro-grid in monkey C (Figure 39). The rate of decline in EMG-rEMG CC with increasing the train-test interval was 0.7-1% per day.

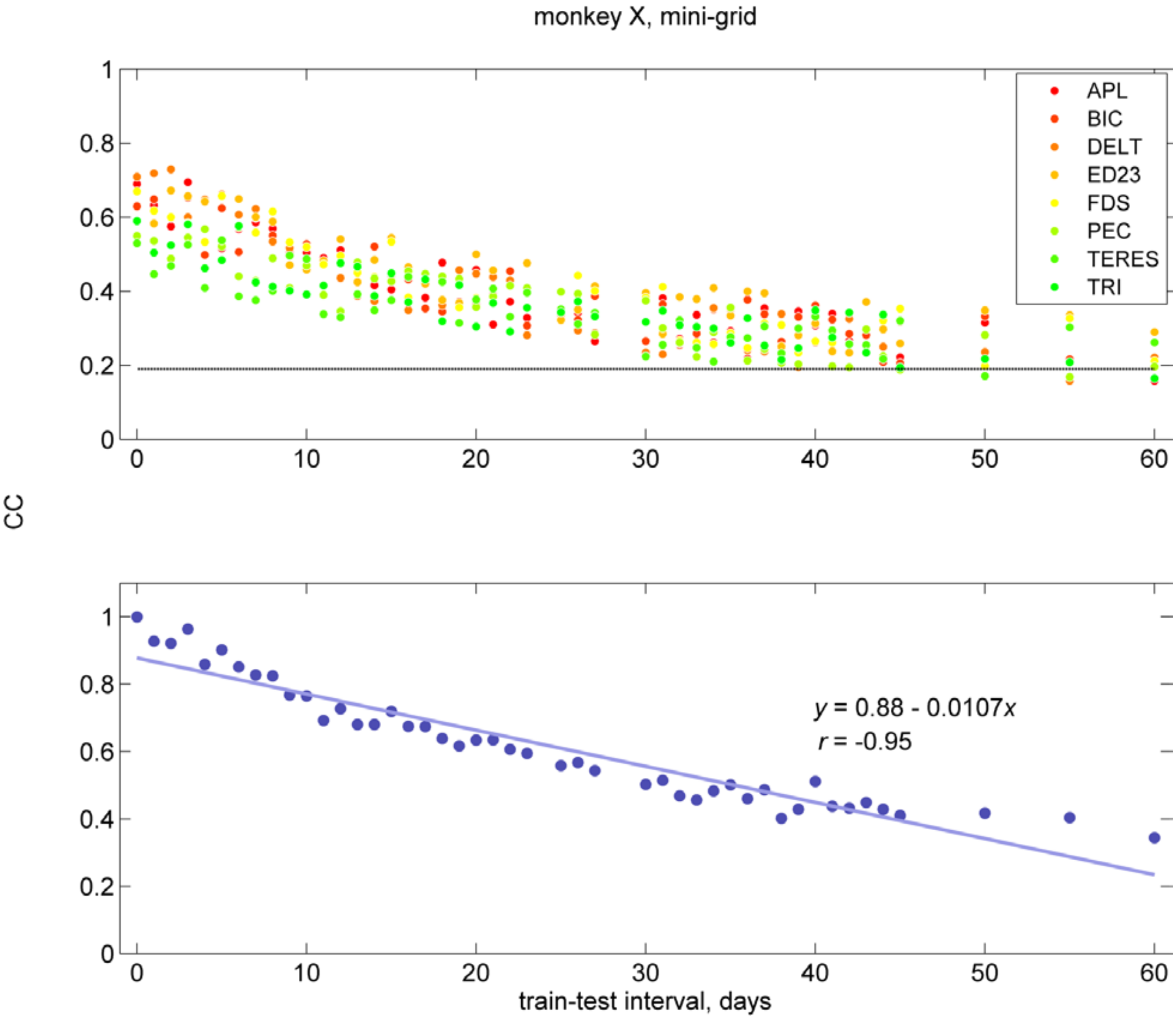

Figure 38. Effect of train-test interval on decoder performance, for the mini-grid array in monkey X. (Top) Correlation coefficient (CC) between actual EMG and reconstructed EMG from decoders that were trained with ECoG and EMG data recorded at different times before or after their testing. Interval "0" corresponds to training and testing performed on different data recorded on the same day. Each data point corresponds to average CC from a variable number of train-test pairs (for example, there were a total of 15 pairs at interval 0, 10 at interval 1 etc), for a given EMG signal. The dotted horizontal line denotes chance level. (Bottom) Weighted average of CC associated with different train-test intervals, relative to CC at time 0, across all EMG signals. Also shown are the linear least-squares fit, its equation and the correlation coefficient between relative CC and train-test interval.

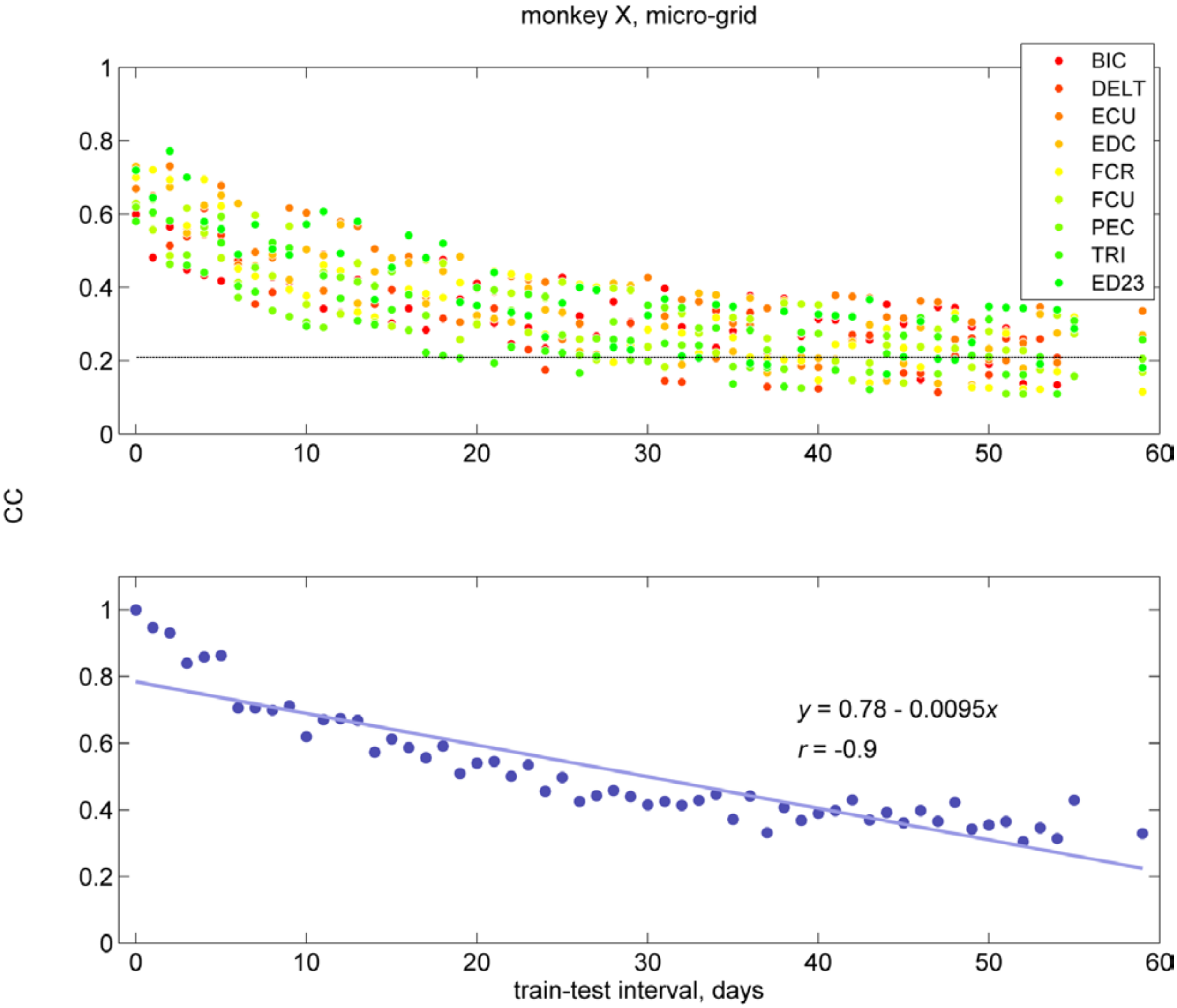

Figure 39. Effect of train-test interval on decoder performance, for the micro-grid array in monkey X. (Top) Correlation coefficient (CC) between actual EMG and reconstructed EMG from decoders that were trained with ECoG and EMG data recorded at different times before or after their testing. Interval "0" corresponds to training and testing performed on different data recorded on the same day. The dotted horizontal line denotes chance level. (Bottom) Weighted average of CC associated with different train-test intervals, relative to CC at time 0, across all EMG signals. Also shown are the linear least-squares fit, its equation and the correlation coefficient between relative CC and train-test interval.

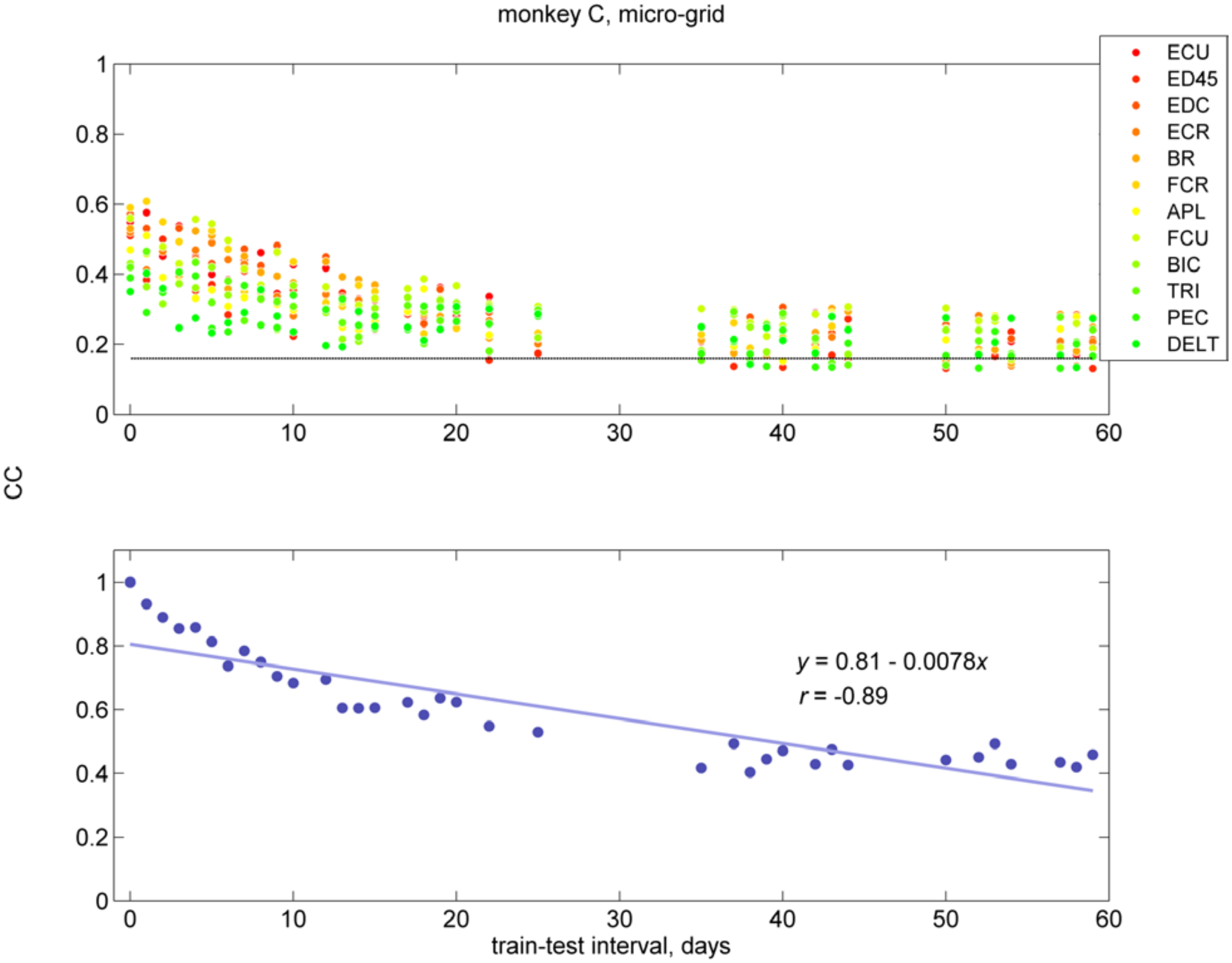

Figure 40. Performance of decoders trained and tested with data from the same recording session, at different implant ages, for micro-grid recordings with monkey C. (Top) Correlation coefficient between actual EMG and

reconstructed EMG as a function of implant age, for different EMG signals. Each data point corresponds to the performance of one decoder, trained and tested on different data recorded on the same day. The dotted horizontal line denotes chance level. (Bottom) Average of CC at a given implant age, relative to CC at the earliest time after implantation, across all EMG signals. Also shown are the linear least-squares fit, its equation and the correlation coefficient between relative CC and implant age.

Discussion

EMG activity-related ECoG changes

We found that different frequency ranges in the ECoG exhibited different behavior relative to EMG activity. Power in low frequencies (LF, <10 Hz) and high frequencies (HF, >30 Hz) increased during times of increased EMG activity, compared to times of rest, whereas the opposite happened with power in intermediate frequencies (IF, 15-25 Hz) (Figure 8). This pattern was seen in both the mini-grid and the micro-grid array (Figure 9), and agrees with the description of movement-related spectral changes seen in human EEG (Pfurtscheller and Lopes da Silva 1999) and ECoG studies (Miller et al. 2007). These changes occurred at around the onset of increased EMG activity and were reversed after the return of the latter to resting levels (Figure 10). Their spatial distribution did not show any preference for specific muscles (compare (Figure 8) and (Figure 11)).

These spectral changes are thought to represent the result of 2 closely associated processes: movement-related desynchronization of the correlated firing of neurons in the beta (15-25 Hz) range, which is manifested as IF suppression, and movement-related increase in neuronal firing rates and/or spiking synchrony that is manifested as an increase in HF power (Zanos 2009) or in a broad-band spectral increase that involves LF as well as HF ECoG components (Miller et al. 2009).

In some electrodes, a rebound of IF power at above resting levels was seen about 200-300 ms after the end of EMG activation (Figure 10); this “post-movement beta rebound” has been described in human

EEG studies (e.g. Pfurtscheller et al. 1996; Salmelin et al. 1995) but, to the best of our knowledge, this is the first time reported in the nonhuman primate. The beta rebound is thought to represent a process of active “inhibition” of the motor cortex and the uncoupling of cell assemblies formed during the planning and execution of movement. In addition to movement, beta rebound follows the termination of motor imagery (Pfurtscheller et al. 2005), and has been suggested as a suitable feature for a “brain switch”, with the aim of detecting a predefined brain state in ongoing brain activity (Pfurtscheller and Solis-Escalante 2009).

Finally, these EMG activity-related spectral changes became less pronounced with time, across all frequencies (Figure 13). This effect must be related to a tissue reaction to the presence of the subdural implant, that has been shown to start developing over a period of 2-4 months after implantation (Griffith and Humphrey 2006; Yuen et al. 1987). Interestingly, no particular frequency range was spared from that effect.

Correlations between ECoG power and EMG activity

The tight temporal relationship between EMG activity and ECoG power could be seen in individual trials and was quantified by calculating correlation coefficients (CCs) between the time course of EMG activity in individual muscles and the time course of ECoG power at different frequency ranges (Figure 7). Those CCs were generally negative for IFs (Figure 14) and positive for LFs and HFs (Figure 15).

As was the case with EMG activity-related ECoG changes, discussed earlier, there was no obvious preference of ECoG activity on a given cortical site for one or more upper extremity muscles, neither any evidence for cosine-like tuning of ECoG activity across different muscles (Figure 16). It is known that a cosine tuning function best captures the relationship between cortical activity, including single neuron activity, LFPs and ECoG power, and upper extremity direction in a reaching task (Anderson et al. 2012; Heldman et al. 2006; Moran and Schwartz 1999). However, there is no evidence that the cosine function is a good approximation for the relationship between cortical activity and EMG activity of upper extremity muscles. In contrast, most studies that attempted to decode EMG activity from cortical signals used linear filters (Carmena et al. 2003; Cherian et al. 2011; Flint et al. 2012b; Nazarpour et al. 2012). The relationship between muscle activity and joint torque or hand position, in a complex, multi-joint task like free reaching and grasping, is far from linear (Brochier et al. 2004; Gonzalez et al. 2010). The linear filter may thus be seen as a "high-level" approximation of a more complex relationship between neural signals and EMG that involves linear and nonlinear components.

Correlations among ECoG power

Even though different ECoG frequencies exhibit distinct relationships with EMG activity and movement, they are not themselves independent of each other. We found that there was significant co-linearity in the time courses of different ECoG frequencies, that formed 2 "clusters": (1) frequencies in the LF and HF ranges were positively correlated among themselves and to each other, and (2) frequencies in the IF range were positively correlated among themselves and negatively correlated to either LFs or HFs (Figure 17 and Figure 18). This suggests that the stereotypical dissociation between IF and LF/HF components seen around movement holds for rest as well. It also suggests that a small number of selected frequency ranges might be enough to capture much of the variability in spectral ECoG changes occurring during naturalistic reaching behavior. Based on these findings, we decided to use power in the following 7 frequency ranges as features for decoding of EMG activity: 2-4 Hz (delta), 4-8 Hz (theta), 8-12 Hz (alpha), 15-25 Hz (beta), 35-50 Hz (low gamma), 70-100 Hz (high gamma).

Such co-linearities were also observed across power signals from separate cortical sites (Figure 19, Figure 20). Power in frequencies in the beta range (15-25 Hz) was the most redundant across both the mini-grid and the micro-grid arrays. Interestingly, peak CCs, at the beta range, in the micro-grid array were smaller than peak CCs in the mini-grid array, which covered a much larger area, even though it is known that EEG and ECoG signal correlation falls with distance (Nunez 2000; Towle et al. 1999). The mini-grid array electrodes have a large diameter (2 mm) and therefore capture summed activity from large populations of neurons. It is conceivable that when large numbers of neurons are contributing to the ECoG signal, local signal differences among neighboring cortical areas are suppressed "suppressed" implies some active process; isn't it more that the local signals contributing less to the recorded ECoG? and the common signal components become more prominent. In sensorimotor cortex, these common signal components are mostly comprised by the widespread beta range oscillations (Murthy and Fetz 1992; 1996b), thus the larger peak CCs over the beta range.

Finally, the presence of all these co-linearities among ECoG power time courses poses certain constraints in the attempt to decode EMG activities. In multiple linear regression, co-linearities among the independent variables often cause the estimated coefficients to be unstable and the predictions by the regression models to be poor. In these cases, the partial least squares (PLS) approach is often used, which was the linear modeling method we adopted (Abdi 2010; Wold et al. 1984).

Decoding of EMG activity

Using linear models with a maximum of 224 independent variables (7 ECoG features x 32 channels), we were able to reconstruct the time course of EMG activity of several upper extremity muscles, at varying levels of accuracy. The average CC between actual and reconstructed EMG (rEMG), at 25-ms temporal resolution, was ~0.7 (R^2=0.49), across all muscles and electrode arrays, with a chance level of 0.2 (R^2=0.04). This figure is slightly lower compared to prior studies that used either spikes or LFPs, or both, to reconstruct EMG activity (Carmena et al. 2003; Cherian et al. 2011; Flint et al. 2012b; Flint et al. 2012c; Nazarpour et al. 2012; Pohlmeyer et al. 2007) add Santucci reference , and even lower than studies that used spikes and/or LFPs to reconstruct kinematics (Donoghue 2008; Green and Kalaska 2011; Nicolelis and Lebedev 2009; Santhanam et al. 2006; Schwartz et al. 2006). The lower performance in EMG decoding than in decoding of kinematic variables may be related to the lower bandwidth of the latter (Mannard and Stein 1973). Similarly, the slightly lower performance than other EMG decoding studies may be, in part, related to the finer temporal resolution used in our study (25 ms, instead of 50 or 100 ms), and therefore higher bandwidth. Another potential reason is the fact that ECoG is probably less representative of neuronal activity, which bears the closest relationship to EMG, than intracortical LFPs; ECoG electrodes lie at a greater distance from cortical neurons and they tend to have larger exposed diameters, which make the recorded fields less spatially specific.

Activities of proximal and distal muscles were decoded at approximately the same accuracy level, in agreement with other similar studies (e.g. Carmena et al. 2003; Flint et al. 2012b). This is compatible with anatomical “mixing” of muscle fields, both in terms of cortical stimulation-elicited muscle responses and of neuronal activity-EMG relationships, for which there is substantial evidence (Craggs et al. 1976; Dum and Strick 2005; Godschalk et al. 1995; He et al. 1995; Raos et al. 2004; Raos et al. 2006; Rathelot and Strick 2006; Sato and Tanji 1989; Senanarong et al. 2004; Stark et al. 2007).

Using an ECoG signal derivation rather than single-ended ECoG signals themselves was deemed important, to avoid contamination by EMG, in high frequencies, or by movement-related artifacts, in low frequencies. Both surface Laplacian (e.g. Fitzgibbon et al. 2013) and common average re-referencing (e.g. Goncharova et al. 2003) are effective at reducing contamination of EEG by non-neural sources. Such re-referencing methods also suppress volume conduction effects (Holsheimer and Feenstra 1977), thereby magnifying the contribution of local cortical activity on the decoding of EMG. We found that these methods were equally effective in that regard.

Maximum decoder performance was reached when a delay of 50-200 ms was introduced between the ECoG and the EMG signals, with ECoG preceding EMG (Figure 24). Several other studies have found that decoder performance is optimal at similar delays between the neural and the kinematic or kinetic signals, with the neural signal preceding (Chao 2010; Cherian et al. 2011; Flint et al. 2012a; b; Kubanek et al. 2009; Miller et al. 2009; Pohlmeyer et al. 2007; Schalk et al. 2007). This suggests that ECoG from sensorimotor cortex contains information about upcoming movement or EMG activity and can be used to control an effector device in a behaviorally useful manner. The CCs between actual and reconstructed EMG activities observed in our study, around 0.7, are likely sufficient to control FES in a BCI setting. Even though no BCI using FES as the output has been used with arm muscles, there are a few examples of FES applied to lower extremity muscles. In a recent study, effective FES was obtained with EEG features that showed smaller CCs to EMGs of individual muscles, in the range of 0.45-0.6 (Do et al. 2012). Furthermore, it is expected that in the closed-loop case, BCI performance would be higher than in the open-loop case (Carmena et al. 2003).

Contribution of ECoG features to decoder performance

In the linear decoders used in this study, HF (>35 Hz) components of the ECoG were the most informative of the time course of EMG activity, in all 3 arrays (Figure 25). This agrees with similar analyses reported elsewhere (Cherian et al. 2011; Flint et al. 2012a; Flint et al. 2012c; Heldman et al. 2006; Kubanek et al. 2009; Schalk et al. 2007). High frequency ECoG has been hypothesized to reflect, or to be correlated with, localized cortical neuronal activity (Crone et al. 2006). The combination of strong correlation to EMG activity (Figure 15) and relative independence across neighboring cortical areas (Figure 19 and Figure 20) likely underlie the consistently increased contribution of HFs in the decoding of kinetic or kinematic variables.

On the other hand, the contribution of the local motor potential (LMP) to decoder performance was surprisingly small, given findings from other reports (reviewed in Schalk and Leuthardt 2011). The reasons for this discrepancy are unclear. It is likely that the Laplacian derivation used in our study, in contrast to the common average reference used in other studies, could be removing a significant portion of this low bandwidth feature. The physiological origin of the LMP is unknown and the LMP has not yet been used in closed-loop BMI applications.

Impact of array geometry on decoder performance

The use of 2 different types of subdural arrays, with different dimensions, electrode densities and electrode sizes, in this study allowed us to explore the impact of a number of features related to the arrays' geometry on the performance of decoders. First, the more electrodes used in the decoders, the better decoder performance was (Figure 26). Interestingly, in all 3 arrays, the inclusion of more than 15 electrodes did not significantly alter performance; the 15 "best" electrodes accounted for about 90% of the latter. Given that the performances of the mini-grid and the micro-grid arrays in monkey X were very similar, it is safe to say that no more than 20 electrodes at a density of 1/mm^2, which was that of the micro-grid array, are needed to decode EMG activity at a reasonable level. Increasing electrode density beyond that level is unlikely to generate significant gains in performance, as the estimated spatial resolution of subdural ECoG is about 1 mm (Freeman et al. 2000). The location of the array might be more important, given that the performance of the micro-grid array in monkey C, which was placed more posteriorly, was inferior to that of the same array type in monkey X.

In both the mini-grid and the micro-grid arrays, medio-lateral (along the central sulcus) coverage of the sensorimotor cortex was more effective than postero-anterior (perpendicular to the central sulcus) (Figure 32) and (Figure 31), suggesting that extensive coverage along the sulcus is more desirable than extensive coverage across the gyrus. This is possibly related to the fact that many cortico-motoneuronal (CM) cells lie along the posterior bank of the central sulcus (Fetz and Cheney 1980) and Smith & Fetz2, and that firing of CM cells has a higher correlation to EMG activity than firing of non-CM cells (Griffin et al. 2008). Furthermore, it has been found that intracortical local field potentials exhibit lower correlation coefficients to each other and, therefore, less redundancy, along the medio-lateral direction than along the antero-posterior direction (Murthy and Fetz 1996a). This finding suggests that in designing more efficient ECoG arrays for the sensorimotor cortex of the monkey, those should be elongated, and should be placed along the central sulcus.

Finally, we found that small diameter electrodes (75 µm, micro-grid array) were associated with better decoder performance than large diameter electrodes (2 mm, mini-grid array), when electrode count, electrode density and cortical coverage area had been factored out (Figure 33). Larger surface electrodes sum neural activity from larger cortical areas, potentially undersampling the cortical signals. In addition, a large, metal, electrode placed on the cortex will create an equipotential surface underneath the electrode, which may affect the weak electrical fields in the superficial layers produced by neuronal activity.

Impact of implant age and test-train interval on decoder performance

The cortical and muscle implants were functional for a total of 4-6 months. During that time, we were able to test the impact of (cortical) implant age, as well as of a wide range of test-train intervals, on decoder performance. We found that performance of the decoders after re-training declined linearly with implant age, decreasing by ~5% per month for the mini-grid array (Figure 34) and by ~8% per month for the mico-grid array (Figure 35). One of the main tissue responses to the presence of subdural arrays is thickening of the dura around and beneath the array (Yuen et al. 1987), essentially encasing the array in connective tissue and increasing its distance from the cortical sources of the recorded signals. Doesn't this affect the high-frequency components, which contribute more to the decoder, more because they become harder to record the lower frequency components? The higher rate of decline for the micro-grid array might be related to the larger impact of source-electrode distance on recordings through small diameter electrodes than through larger diameter electrodes (Nelson et al. 2008). An additional reason for worsening performance with increasing implant age is the declining quality of EMG signals. Our experience has shown that subcutaneous muscle implants perform well up to 3-6 months after surgery. After that time EMG quality degrades, something that would affect decoder performance independently of age-related changes in the cortical signals.

Decoders trained and tested on separate days performed worse as the train-test interval increased. The linear rate of decline was 0.7-1% per day, resulting in the decoders performing at chance levels after 40-60 days. This performance decline was steeper than that reported in a long-term study in which kinematic parameters were decoded from cortical signals up to 6 months after decoder training (Chao 2010). One of the reasons for such a discrepancy might be related to the much higher bandwidth of EMG compared to that of kinematics. In fitting a high bandwidth, noisy signal with linear decoders with large numbers of independent variables, as in our case, there is good chance for overfitting (Abdi 2010). A decrease of decoder efficacy over time was also observed with neural populations and movement kinematics (Wessberg et al. 2000). Finally, this decay of open-loop decoder accuracy could be countered by closed-loop BMI control (Carmena et al. 2003).

Chapter 3: Effects of repetitive electrical cortical surface stimulation on the electrode-tissue interface, cortical excitability and spontaneous cortical activity

Introduction

Electrical cortical surface stimulation (ECS), the delivery of electrical stimuli to the cortex through subdural or epidural electrodes, has a long history in experimental and clinical neurosciences. It was the first method used to explore the association between cortical location and motor movement. Bartholow was the first to test and document the motor effects of ECS in humans, at the end of 19th century (Morgan 1982). His observations were precursors to more detailed human cortical mapping studies by Penfield (Penfield 1950; Penfield and Boldrey 1937), who coined the term “cortical homunculus”. Sherrington, in the late 19th and early 20th century, first provided a detailed description of the motor responses elicited by ECS in nonhuman primates, compiled response localization maps of the cerebral hemispheres and gave a first account of how stimulation itself alters cortical excitability (Sherrington 1911). At a later time, Woolsey described the primate motor homunculus as a composite of the maps of many individuals and made observations on the inter-subject variability and the temporal stability of those maps (Woolsey et al. 1952).

For several decades, recording and stimulating through surface electrodes has seen primarily clinical use, in the pre-operative planning (Duffau 2007) and intra-operative monitoring (Berger et al. 1990) of cortical resection surgeries for tumor or intractable epilepsy. Over the past decade however there has been increased interest in electrocorticographic (ECoG) potentials, among researchers of human neurophysiology (Hatsopoulos and Donoghue 2009b) and brain-machine interfaces (Schalk and Leuthardt 2011). ECoG has advantages over other commonly used methods for studying brain activity, as it combines minimal invasiveness with increased spatial and temporal resolution, over EEG and fMRI respectively. On the other hand, brain stimulation in the context of BMIs has recently emerged as a method to deliver “sensory” feedback signals directly into the brain, by-passing an injured efferent pathway (Dobelle 2000; O'Doherty et al. 2011; O'Doherty et al. 2012; Romo et al. 2000; Romo et al. 1998) or to induce activity-dependent cortical plasticity which could “re-wire” an injured cortical area (Jackson et al. 2006a; Rebesco et al. 2010). Surface electrodes are theoretically an attractive means of accessing the cortex for both recording and stimulation in clinical BMI systems, but the extent to which they can chronically deliver ECS safely and effectively delivered is unknown. There is very little knowledge of the effects of prolonged ECS on the properties of the electrode-tissue interface, on cortical excitability and on cortical activity.

Methods

Experiment timeline

Bipolar stimulation was delivered through subdural or epidural electrodes, with the monkey sitting quietly in a primate chair. Several short-term (6 minutes) and prolonged (30 minutes) stimulation sessions were performed. On each session involving one of the subdural arrays, the tested electrode received stimulation at a constant rate (2, 3, 4 or 5 Hz). Stimulus intensity was at 80% of MEPT, defined as the minimum current intensity at which at least 50% of stimuli led to an identifiable MEP response. A total of 5 electrodes were tested on the mini-grid subdural array, and 4 on the micro-grid subdural array, at all 4 stimulation rates. On each session involving the epidural array, a different electrode received ECoG activity-dependent stimulation for 30 minutes, at a variable rate (average rate across sessions: 1.9-2.7/sec). Stimulus intensity was at 80% of MEPT. A total of 11 epidural electrodes were tested.

Electrode impedance and in some cases, MEPT were measured on most electrodes (stimulating and non-stimulating) of the tested array, before and at various times after stimulation. Ten to thirty minute-long ECoG signal recordings were also performed at those times. In the short-term stimulation sessions, only impedance was measured, immediately before and after stimulation, and 1, 2 and 3 minutes later. In the prolonged stimulation sessions, impedance was measured and ECoG was recorded immediately after stimulation, and 12-24 and 24-48 hours later. MEP thresholds were determined in a subset of the prolonged stimulation sessions with the micro-grid subdural array (at stimulation rates of 2 and 5/sec).

Four additional stimulation sessions with the micro-grid subdural array were performed, in which suprathreshold stimuli were delivered at a constant rate (2, 3, 4 or 5/sec) for a total of approximately 7500 stimuli, while MEPs were being recorded.

Behavioral task

The monkey sat calmly in a primate chair, in front of a computer screen, with both its forearms comfortably resting at the monkey’s sides, flexed at the elbow; both wrists were restrained. In one variation of this task, one hand rested inside a manipulandum connected to a 3-D torque transducer. The transducer registered radial/ulnar deviation, flexion/extension, and pronation/supination wrist torques. The three torque components (R/U, F/E and P/S) controlled the vertical position, the horizontal position and the rotation of a rectangular cursor, respectively. The monkey was rewarded for not producing any wrist torques, by holding the cursor inside a “resting” target box. This setup was used for testing and measuring isometric wrist torques elicited by cortical stimulation through electrodes in the contralateral hemisphere, before and after a conditioning session.

In the second variation of this task the monkey had an accelerometer (MMA7341L, Pololu Robotics and Electronics) taped to the back of each hand. A cursor, one for each hand, represented the root mean squared output of each accelerometer. The monkey was rewarded for not generating arm acceleration, by holding the cursor inside a “resting” target box.

Implants

Details on the arrays, muscle implants, the surgical procedures, and the cortical and EMG recording techniques are given in chapter 1.

Electrical stimulation

Electrical stimuli were delivered to a given cortical electrode through a biphasic stimulus isolator (BSI-1, BAK Electronics, Stanford, FL), driven by a pulse generator (Master-8, A.M.P.I., Jerusalem, Israel). The pulse generator was triggered by a computer running Simulink-based custom-made software. Each stimulus was a biphasic, symmetric pulse, of 0.2ms pulse width. Stimulation was bipolar; neighboring electrodes were always used.

Measurement of electrode voltage

Electrode voltage was monitored by recording the voltage developed by the stimulator between the active electrode and the stimulation return, during delivery of the constant current stimulus pulses (Figure 1). The input resistance of the amplifier was 2 GOhm, much higher than the electrode resistance.

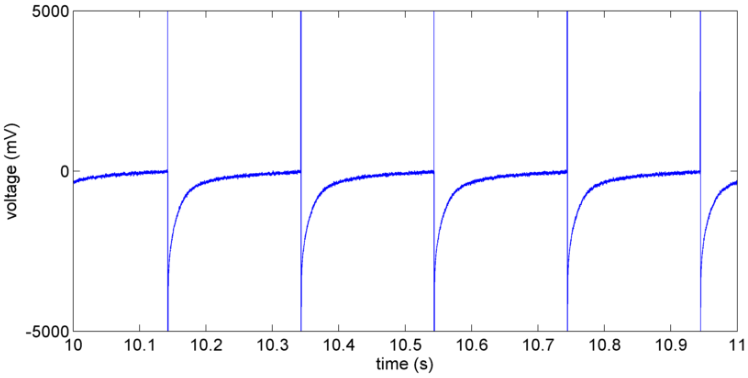

Figure 41. Voltage developed across a subdural electrode during delivery of constant-current, symmetric, biphasic pulses. Stimulation parameters: pre-stimulation electrode impedance 35 KOhm, current intensity 2.4 mA, pulse

width 0.2 ms, stimulation rate 5 sps. The voltage trace is truncated for reasons of clarity; in this case, peak voltage amplitude was 65 V.

Measurement of electrode impedance

A standard technique for performing electrode impedance spectroscopy was used (Barsoukov and Mcdonald 2005). Briefly, a low intensity (1 µA) sinusoid current of slowly changing frequency (from 2 Hz to 1 KHz, covered in 60 sec), was delivered in constant-current mode between the active electrode and the stimulation return. The current trace, as well the trace of the voltage developed between the active electrode and the return were registered by an amplifier. At very low current intensities the electrode can be assumed to operate under linear conditions. The electrode impedance at a specific frequency can then be calculated with Ohm's law (Figure 2, Figure 3). All impedance values used in this paper were evaluated at 1KHz.

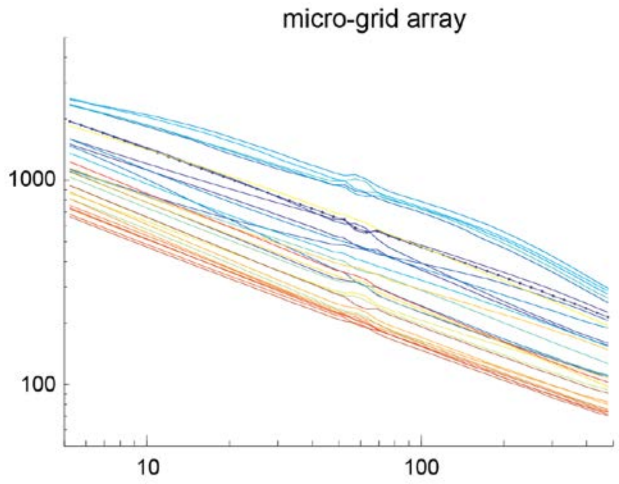

Figure 42. Electrode impedance spectrum for several electrodes of the micro-grid subdural array.

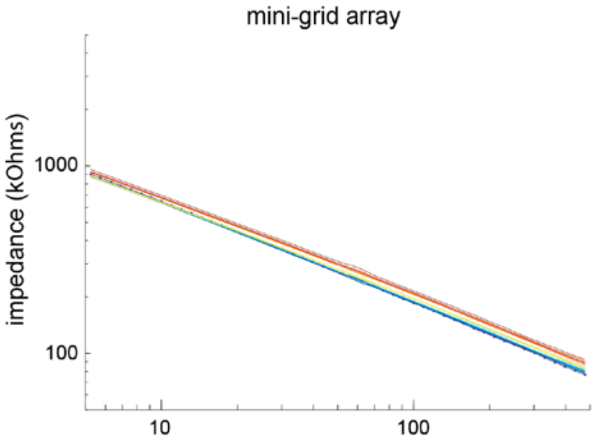

Figure 43. Electrode impedance spectrum for several electrodes of the micro-grid subdural array.

Stimulation for testing evoked torques/motor-evoked potentials (MEPs)

Stimuli for testing thresholds for evoked torques or MEPs were delivered when the monkey performed the "arm resting" task. Evoked isometric torques were elicited by trains of stimuli delivered to selected electrodes. Each train consisted of 17 biphasic pulses, at 333/sec. Stimulus-evoked torques were registered and digitized by a personal computer, and displayed on a screen. Current intensity was progressively increased; 5-10 stimulus trains per current intensity step were delivered.

Motor-evoked potentials were elicited by single-pulse stimuli delivered to selected electrodes, at a rate of 2/second, at progressively increasing current intensities. Evoked EMG activities from the contralateral arm and forearm were recorded and MEPs were displayed in real-time. A total of 50-75 stimuli per current intensity step were delivered.

In each case, stimulus intensity-response curves were compiled. Response was defined as the peak-to-trough amplitude of the average MEP on a selected muscle (the same for each tested electrode), between 5 and 20ms after the stimulus, or the peak-to-trough amplitude of the average evoked pronation-supination torque, between 30 and 150 ms after the end of the stimulus train. MEP responses elicited at times when the monkey was generating EMG activity at the time of stimulus delivery were excluded by the analysis.

Estimation of ECoG signal power

The data from each 10 to 30-minute-long ECoG recording were segmented into 5-sec-long epochs (24000 samples per channel). The power spectral density (PSD) function of the signal from each epoch was estimated using the periodogram method, between 4 and 100 Hz. Frequencies below 4 Hz were not included in the analysis because they were particularly affected by movement artifacts; frequencies above 100 Hz were not included either because they were assumed to be close to the noise floor. The average power spectrum of a signal from a given electrode across an entire file was generated by taking the mean of spectra across all epochs. Spectral components around 60 Hz (line noise) were replaced by linear extrapolation between the corner frequencies 58 and 62 Hz.

In order to quantify the effects of stimulation on ECoG signal power at different frequencies, we grouped together frequencies that are thought to be generated by distinct physiological mechanisms (Buzsaki and Draguhn 2004). The PSD function of ECoG signals follows an inverse power law (1/f) (Freeman et al. 2000) which is thought to be the result of the physical architecture of neuronal networks and the limits in the speed of neuronal communication imposed by conduction velocity and synaptic delays(Nunez 1995). The slope of this 1/f relationship depends on ambient noise, recording conditions and reflects random spectral variability that is not related to electrical stimulation (Figure 4, top).

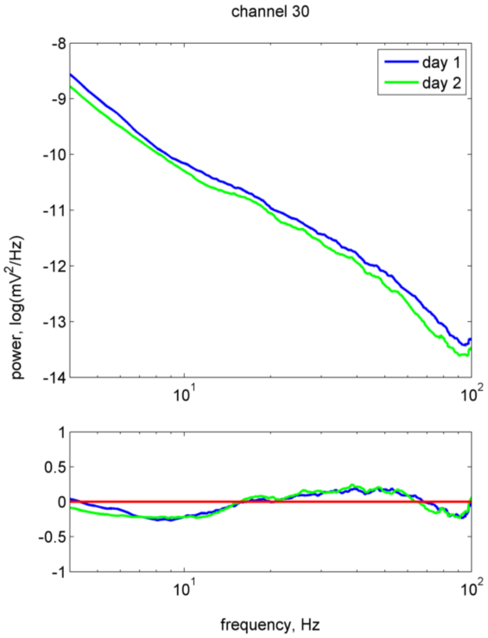

Figure 44. Spectral whitening reduces random variability in power spectra. (Top) Power spectra of the signal from a subdural array electrode, from 2 consecutive days. No stimulation has occurred between the 2 recordings. (Bottom) Whitened power spectra.

In order to remove the 1/f component from the PSD (spectral whitening), we first fitted the 1/f function to the PSD:

$$y = a + b\frac{1}{f^n}$$

Fitting was performed using the Matlab Curve Fitting Toolbox, with a nonlinear least squares regression model; bounds for the value of *n* were set to [0,5]. The fit line tracked the 1/f trend in the original PSD (Figure 5, top). The whitened spectrum was generated by subtracting the fit line from the original PSD (Figure 5, middle). The frequency axis was then segmented into 5 frequency ranges: 4-8 Hz (theta), 8-12 Hz (alpha), 15-25 (beta), 25-35 (low gamma), 65-100 (high gamma). The whitened spectrum, at a given frequency, represents the amount of PSD power exceeding or being less than the 1/f component, at that frequency. Averaging the whitened spectrum across each of these frequency ranges produced one ECoG power value per range (Figure 5, bottom). The random variability introduced by the 1/f slope is minimized in the whitened spectrum (Figure 4, bottom).

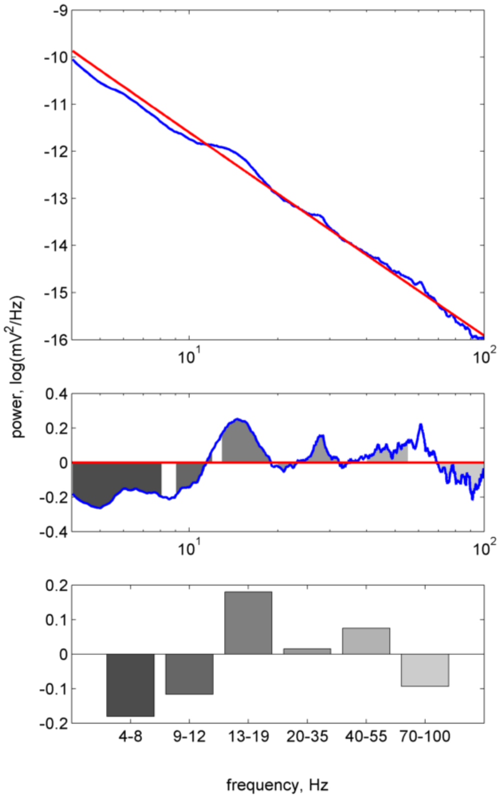

Figure 45. Power spectral density (PSD) function and spectral whitening of an ECoG signal. (Top) Log-log plot of the average PSD function of the signal from an ECoG electrode during a 30-min-long recording (blue line), and the 1/f fit to it (red line). For details on the fit function, see text. (Middle) The PSD function after whitening, by subtracting the 1/f component from the original PSD. Shown are the spans of 6 frequency ranges: theta (4-8 Hz), alpha (9-12 Hz), low beta (13-19 Hz), high beta (20-35 Hz), low gamma (40-55 Hz), high gamma (70-100 Hz). (Bottom) Average "whitened" signal power across the 6 ranges. A positive (or a negative) value represents power that exceeds (or is less than) that of the 1/f component at that frequency range.

Histology

The animal was sedated with intramuscular Ketamine HCl (20 mg/kg) and Nembutal (100 mg/kg) was administered IV to induce a surgical anesthetic plane. Transcardial perfusion was accomplished using room temperature saline (0.9% normal) followed by 10% neutral buffered formalin via a gravity feed apparatus. The brain was removed; tissues were sectioned, digitally imaged (NIKo Cool-pix), and subsequently processed for histology. Routine histological tissue sections (7µm) were stained with Hematoxylin and Eosin and evaluated. Additional sections were stained with glial fibrillary acidic protein (GFAP) stain and luxol fast blue (LFB) stain. Photomicrographs were obtained using a Nikon Digital Sight DSU1 and were processed through NIS-Elements F 2.20 software.

Results

Transient increase in electrode impedance with short-term stimulation

During the short-term stimulation sessions, electrode impedance increased transiently. This increase was observed in the micro-grid array (Figure 6), as well as the mini-grid array (Figure 7). These increases involved both stimulated and non-stimulated electrodes. Impedance increase was generally higher for the micro-grid than the mini-grid (Figure 8). Impedance returned to pre-stimulation levels at about 3 minutes after the end of short-term stimulation (Figure 8).

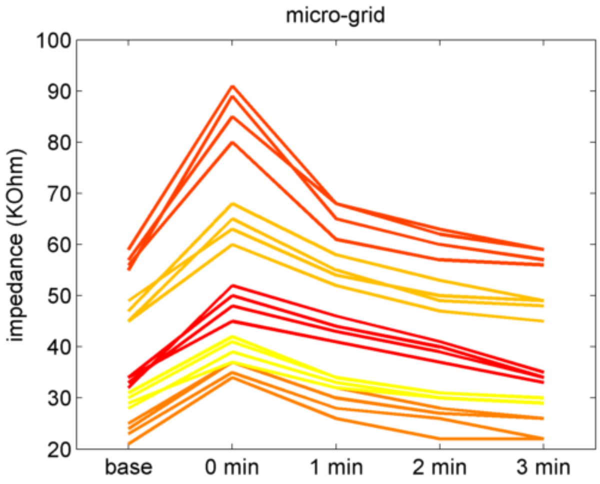

Figure 46. Changes in electrode impedance during short-term (6 min) stimulation, in several electrodes of a micro-grid subdural array. Different colors correspond to different stimulated electrodes.

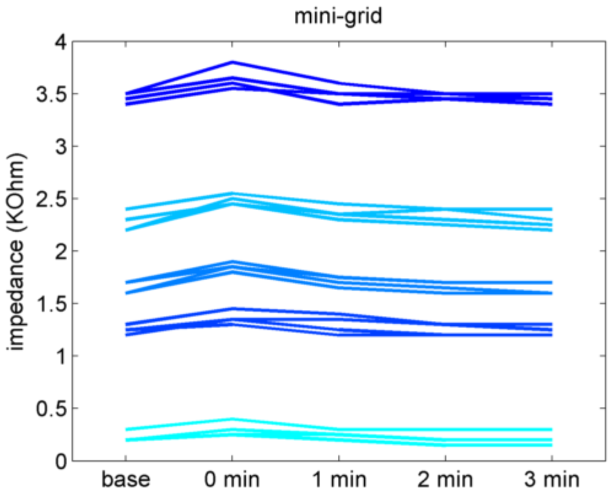

Figure 47. Changes in electrode impedance during short-term (6 min) stimulation, in several electrodes of a mini-grid subdural array. Different colors correspond to different stimulated electrodes.

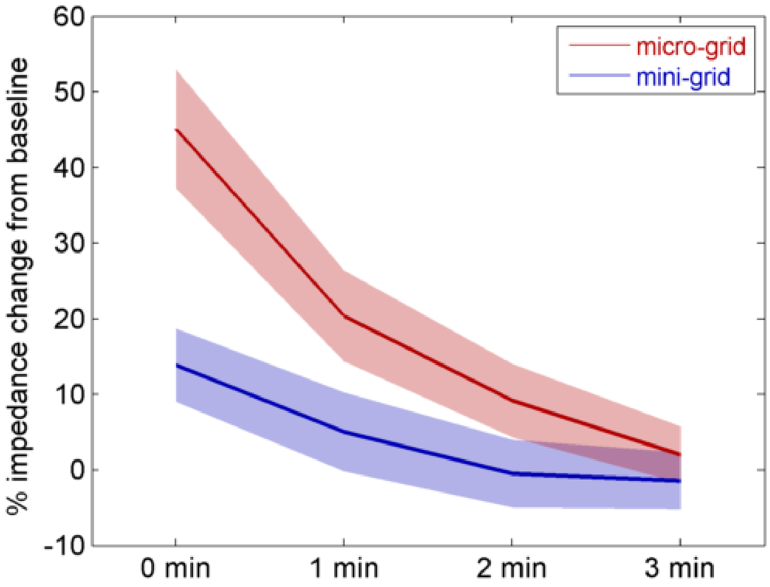

Figure 48. Average change in electrode impedance with short-term stimulation, with respect to baseline levels, for the 2 tested subdural arrays. The change in electrode impedance, with respect to baseline levels, was significant immediately after stimulation (p<0.01), at 1 minute post-stimulation (p<0.01) and at 2 minutes post-stimulation (p=0.07). It was not significant at 3 minutes post-stimulation (p NS). The change in impedance for the micro-grid array was significantly larger than for the mini-grid array immediately after stimulation (p<0.01), at 1 minute post-stimulation (p<0.01) and at 2 minutes post-stimulation (p=0.03).

During stimulation, these transient impedance changes manifested themselves as a gradual increase in the peak electrode voltage, with successive stimuli (Figure 9). This increase was more noticeable during stimulation through the micro-grid array, and involved primarily the second, charge-balancing phase (Figure 10). The change in peak electrode voltage reached a plateau after 400-500 stimuli for micro-grid electrodes, whereas no obvious plateau was seen for mini-grid electrodes, within the 6 minutes that these sessions lasted.

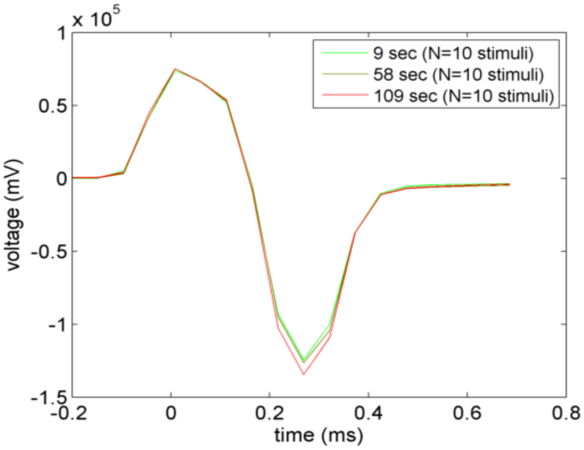

Figure 49. Averages of 10 consecutive, electrode voltage sweeps, at different times in a stimulation session through a micro-grid array electrode.

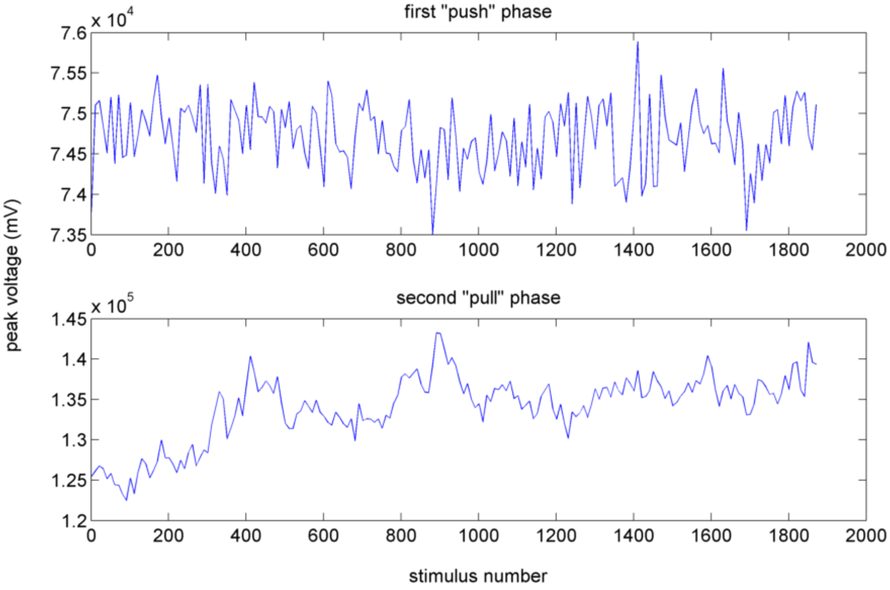

Figure 50. Dependence of peak electrode voltage on the number of stimuli delivered, during short-term stimulation at a constant rate of 5 Hz, through a micro-grid array electrode. Peak voltage is shown separately for the first ("push") phase (top panel), and the second ("pull", or charge-balancing) phase (bottom panel). Each point represents average voltage from 10 successive stimuli. Peak electrode voltage during the second phase seems to plateau after about 400-500 stimuli.

Long-lasting drop in electrode impedance with prolonged stimulation

In prolonged stimulation sessions, electrode impedance dropped, in all electrode arrays. That drop was specific to the stimulating electrode in the epidural array (Figure 11), but occurred on additional, non-stimulating, electrodes in both the mini-grid (Figure 12) and the micro-grid (Figure 13) subdural arrays. There was no difference in the impedance change for prolonged stimulation between the different stimulus rates.

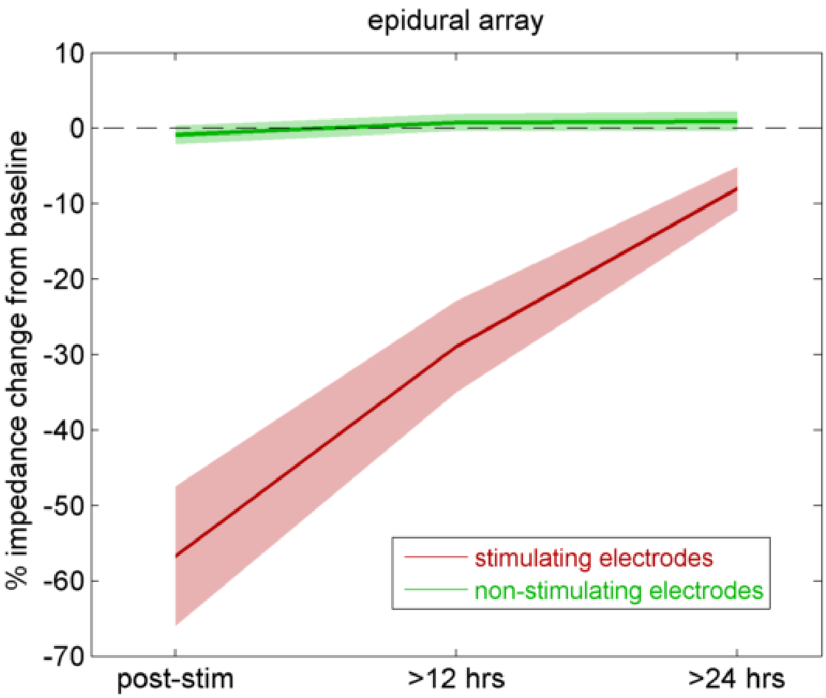

Figure 51. Average (+/- 2SE) changes in impedance of epidural stimulating and non-stimulating electrodes, at various times after the end of prolonged (>3 hrs) stimulation: immediately after stimulation ("post-stim"), at least 12 hours later and at least 24 hours later. Impedance immediately after stimulation was significantly lower than pre-stimulation at the stimulating electrodes ($p<0.001$) but not at the non-stimulating electrodes (p NS) . There was a statistically significant effect of time of measurement on the impedance of the stimulating electrodes ($p<0.001$); impedance gradually returned to baseline levels within 24-48 hours after stimulation.

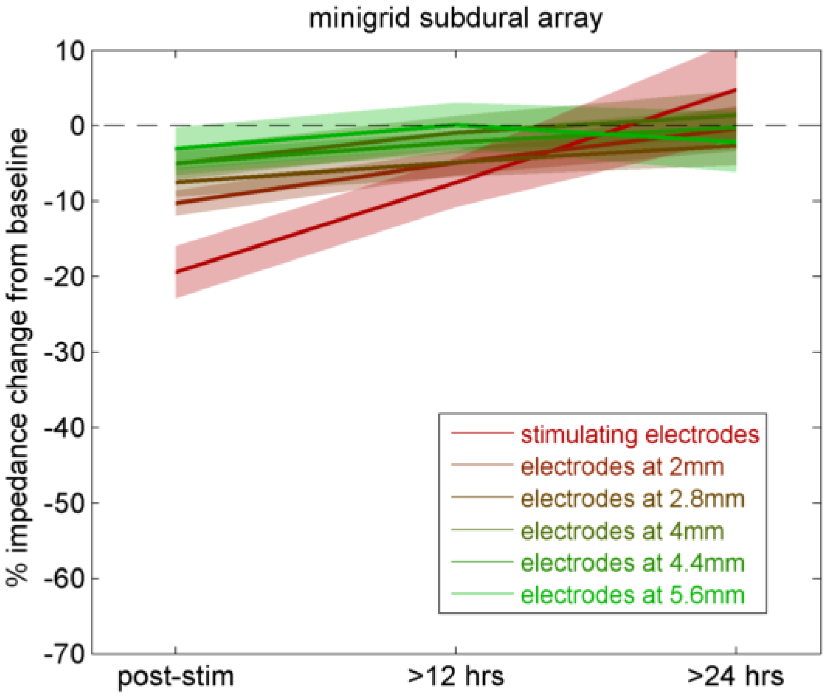

Figure 52. Average (+/- 2SE) changes in impedance of mini-grid subdural electrodes at various distances from the stimulating electrode, at various times after the end of prolonged (>3 hrs) stimulation sessions: immediately after stimulation ("post-stim"), at least 12 hours later and at least 24 hours later. Impedance immediately after stimulation was significantly lower than pre-stimulation, for electrodes at all distances (p between 0.03 and <0.001). Electrodes at smaller distances from the stimulating electrode showed larger impedance changes (p=0.008). There was a statistically significant effect of time of measurement on impedances of electrodes at all distances (p=0.01), with the largest change from baseline occuring immediately after stimulation.

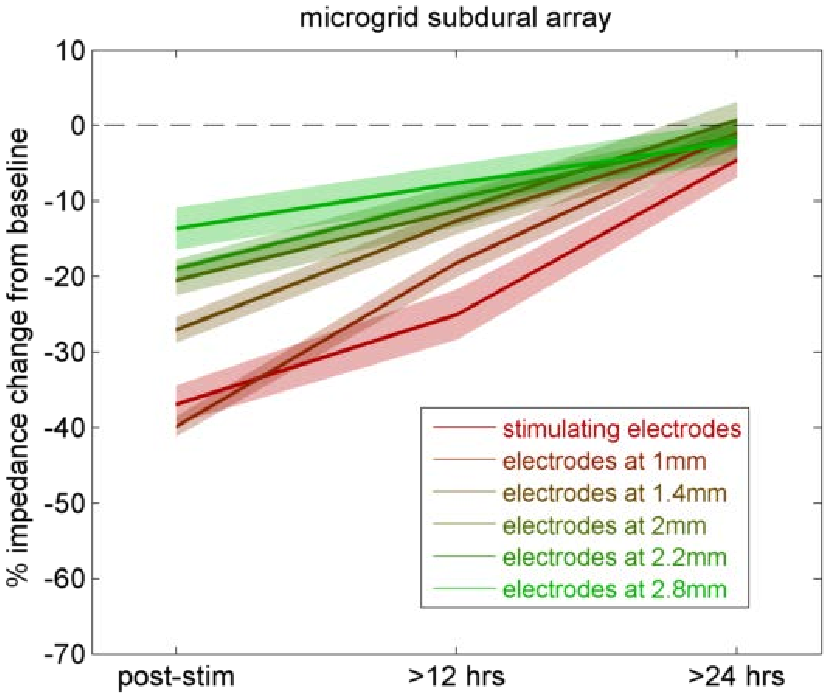

Figure 53. Average (+/- 2SE) changes in impedance of micro-grid subdural electrodes at various distances from the stimulating electrode, at various times after the end of prolonged (>3 hrs) stimulation: immediately after stimulation ("post-stim"), at least 12 hours later and at least 24 hours later. Impedance immediately after stimulation was significantly lower than pre-stimulation, for electrodes at all distances (p between 0.03 and <0.001). Electrodes at smaller distances from the stimulating electrode showed larger impedance changes (p<0.001). There was a statistically significant effect of time of measurement on impedances of electrodes at all distances (p<0.001), with the largest change from baseline occuring immediately after stimulation.

Long-lasting increase in MEP thresholds with prolonged stimulation

Prolonged, repetitive cortical stimulation of the micro-grid subdural array led to a significant increase in MEPT. This increase was maximal immediately after stimulation (35-55%); it became progressively smaller within 48 hours, but had not returned to pre-stimulation levels by the end of that period (Figure 14). It was largest at the stimulating electrodes and became progressively smaller for electrodes at increasing distances from those. A stimulation rate of 2 Hz was associated with a marginally larger MEPT increase than a stimulation rate of 5 Hz; the difference was not statistically significant (Figure 15).

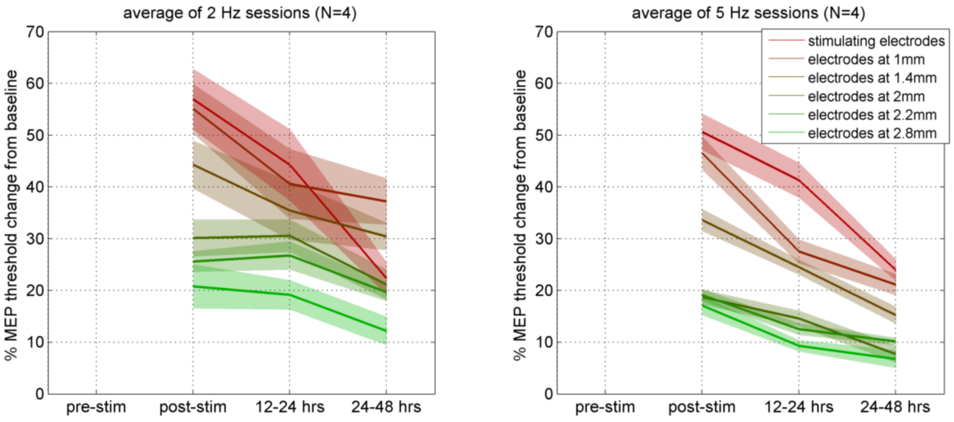

Figure 54. Change in MEP thresholds (MEPT) during prolonged repetitive cortical stimulation, for different stimulation rates. Average % change in MEPT from pre-stimulation level, for electrodes at different distances from stimulating electrode, for a stimulation rate of 2 Hz (left panel) or 5 Hz (right panel). The change in MEPT was larger for the 2-Hz rate compared to that for the 5-Hz rate, for all electrode distances (p between 0.001 and 0.055).

When cortical stimulation was delivered at threshold-intensity, a progressive decrease in the amplitude of the MEP was seen over the course of 30 minutes (Figure 16). This progressive decrease was seen in all stimulation rates tested (2, 3, 4 and 5 Hz).

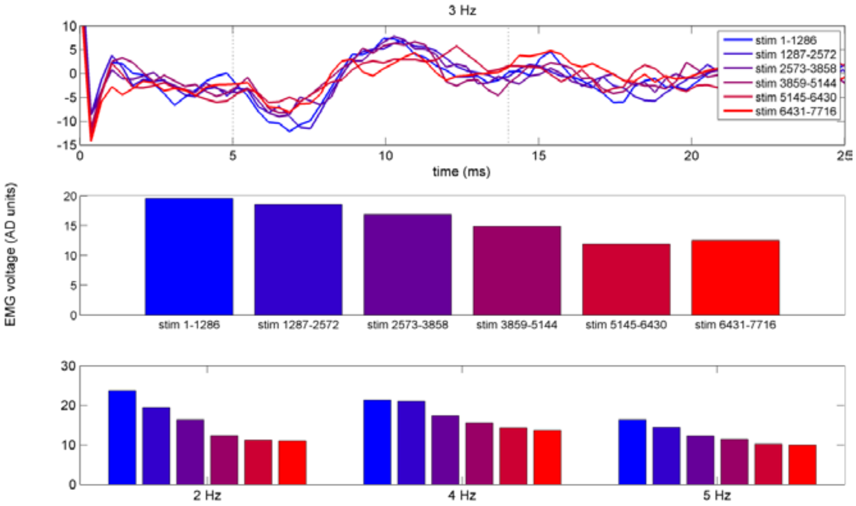

Figure 55. Time evolution of MEPs and their amplitude during the duration of repetitive, threshold-intensity, cortical surface stimulation through a subdural array. (Top): Average MEPs during different time periods of a stimulation session, in which stimuli were delivered at a rate of 3Hz. The bright blue sweep was compiled from the first 1286 stimuli, the bright red from the last 1286 stimuli in that session. The two vertical dashed lines denote the segment of the sweep over which MEP amplitude was calculated. (Middle): Average MEP amplitudes during the same stimulus count periods. MEP amplitude was calculated as the sum of the first (negative) and second (positive) phase of the average MEP, for that time period. (Bottom): Average MEP amplitudes during similar stimulus count periods (each bar representing approximately 1280 stimuli), in 3 separate sessions where repetitive stimulation was delivered at rates of 2, 4 and 5 Hz.

Long-lasting changes of spontaneous ECoG signal power with prolonged stimulation

Prolonged repetitive stimulation led to changes in the power of the recorded ECoG signals, in several frequency ranges (Figure 17). Those changes occurred on the stimulating electrodes, as well as on many non-stimulating electrodes (Figure 18).

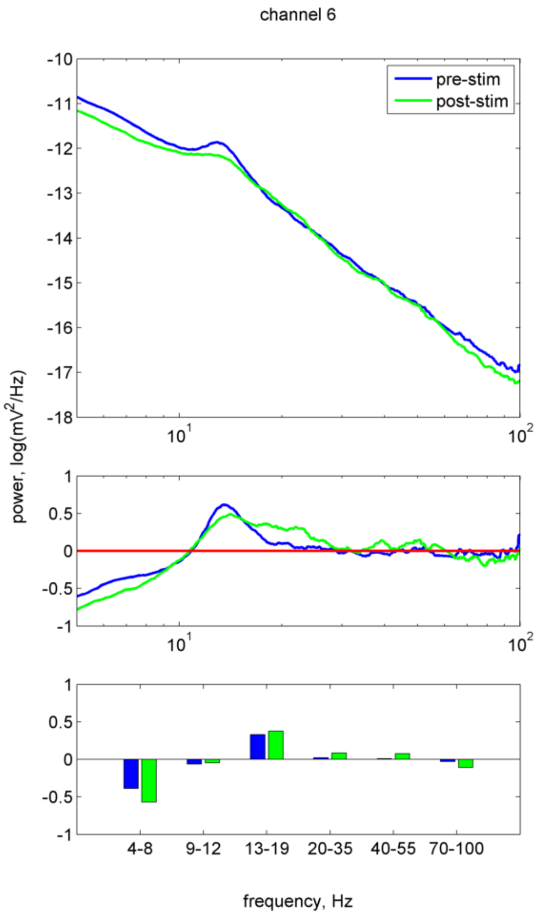

Figure 56. Power spectrum change on a stimulating electrode, after a prolonged stimulation session. (Top) Power spectra before (pre-stim) and after (post-stim) stimulation. (Middle) Whitened spectra. (Bottom) Average whitened spectral power across 6 frequency ranges, before and after stimulation.

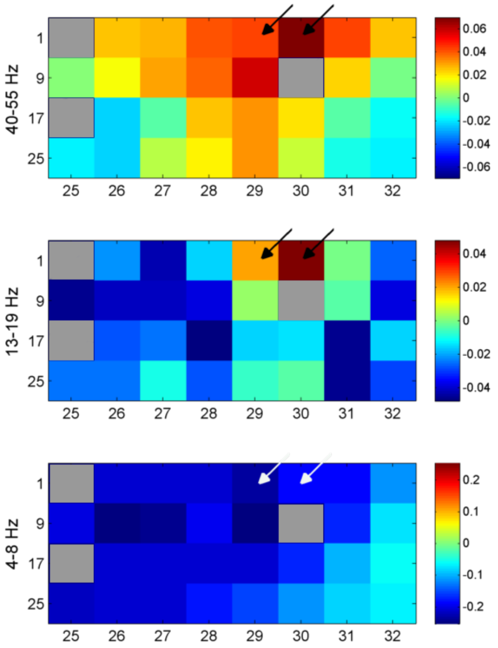

Figure 57. Change in power across an entire array, with bipolar stimulation between 2 neighboring electrodes (arrows, at electrodes 5 and 6). Power changes in three different frequency ranges are shown: 4-8 Hz (bottom), 13-19 Hz (middle), 40-55 Hz (top). Cold colors denote decrease in power, warm colors denote increase in power. Grey squares correspond to electrodes with no ECoG signal. Inter-electrode distance in the mini-grid subdural array is 2 mm. This is from the same experiment as the one in the previous figure.

ECoG power changes on nearly all frequency ranges were maximal immediately after stimulation, and returned closer to pre-stimulation levels 24 hours later. In addition, not all frequencies were affected in the same way. Signal power in the theta (4-8 Hz), alpha (9-12 Hz), low beta (13-19 Hz) and high beta (20-35 Hz) decreased on average, while power in the low gamma (40-55 Hz) and high-gamma (70-100 Hz) ranges increased (Figure 19). Similar effects were seen in the subdural mini-grid and the subdural micro-grid array.

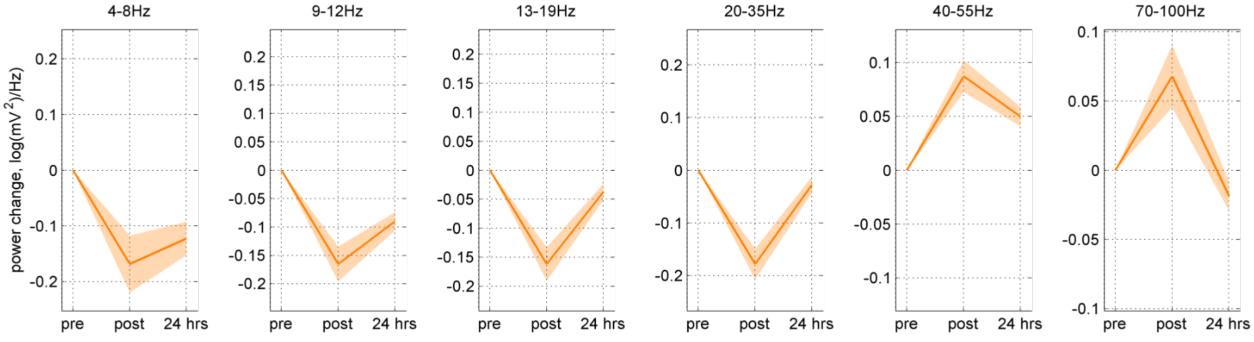

Figure 58. Change in ECoG signal power in an epidural array as a function of time relative to stimulation. Each curve represents the average (+/- 2SEM) change in power relative to its pre-stimulation level, immediately after stimulation (post) and 24 hours later. Each panel corresponds to power in a different frequency range. A total of 27 experiments went into calculating the pre-post change, and 9 into the pre-24 hours change. Power changes immediately after stimulation were significantly different than zero for all frequency ranges ($p<0.001$). Power changes at 24 hours after stimulation were still significantly different than zero for all ranges ($p<0.001$), except high gamma ($p=0.067$).

Finally, ECoG power changes, in all frequency ranges, were maximal on the stimulating electrodes, becoming progressively smaller on electrodes at increasing distances from the stimulating ones. This effect was seen in the epidural (Figure 20), as well in the subdural arrays. Independently of frequency, power change fell to 20% of its peak magnitude, at the stimulating electrodes, at a distance of 5-7 mm from the stimulating electrodes for the epidural array (Figure 20), at a distance of 4-5 mm for the subdural mini-grid array, and at a distance of 2-2.5 mm for the subdural micro-grid array.

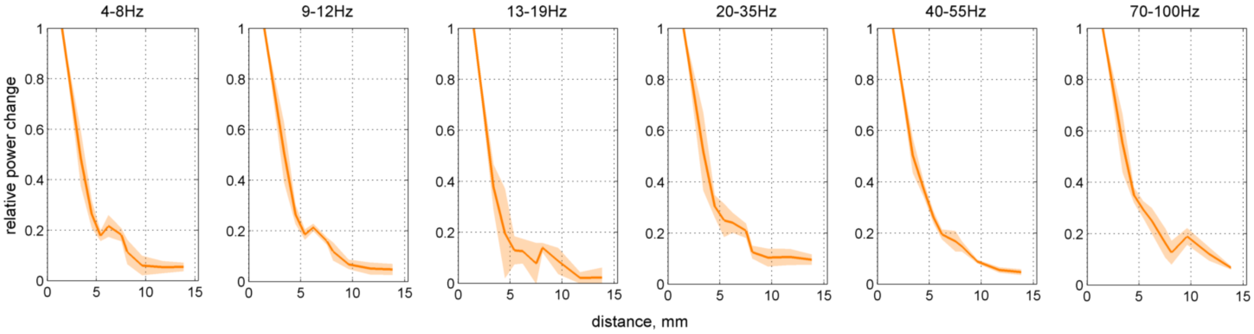

Figure 59. Change in ECoG signal power in an epidural array as a function of distance from the stimulating electrodes. Each curve represents the average (+/- 2SEM) change in power at a certain distance from the mid-point between the 2 neigboring stimulating electrodes, normalized by the average change in power on the 2 stimulating electrodes. The different panels correspond to different frequency ranges. The relative power change showed a strong dependance on distance (p<0.001 for all frequency ranges). It fell to the 20% of its peak magnitude at the stimulating electrodes at around 5-7 mm from them.

Histological changes around subdural arrays

Two sets of specimens were examined. One set came from cortex underneath the subdural micro-grid array that had received stimulation, and the second from cortex underneath the subdural micro-grid array that had not been stimulated.

At gross necropsy, both subdural implants were found to be encased by proliferative, fibrous tissues contiguous with the dura (2 cm in length and 0.5cm in thickness) and epidural space. Inflammatory exudate was present within the calvarial implant and epidural space surrounding the arrays, but it was effectively walled off from the parenchyma of the brain by proliferative tissue. Tissues encasing the older array were thicker than those encasing the newer array. Histology of the para-array proliferative tissue demonstrated marked dural thickening by dense fibrous tissue. Within fibrous tissues, there were multifocal lymphoid aggregates organized into follicles, aggregates of hemosiderin laden macrophages, and regions of severe inflammatory cell infiltrates composed predominantly of plasma cells admixed with neutrophils, lymphocytes, histiocytes, and multinucleated giant cells (MNGC's). Implant material present within histological sections demonstrated a MNGC foreign body inflammatory response.

Luxol fast blue staining showed no gross-scale differences in the degree of myelination or neuronal density between the cortical area beneath the electrode array that received stimulation ("lesion") and cortical tissue underneath the array that had not received stimulation ("control") (Figure 21). Glial fibrillary acidic protein staining showed slightly increased glial tissue at the lesion (Figure 22), whereas H&E staining showed no gross-scale differences in neuronal density between the lesion and the control (Figure 23).

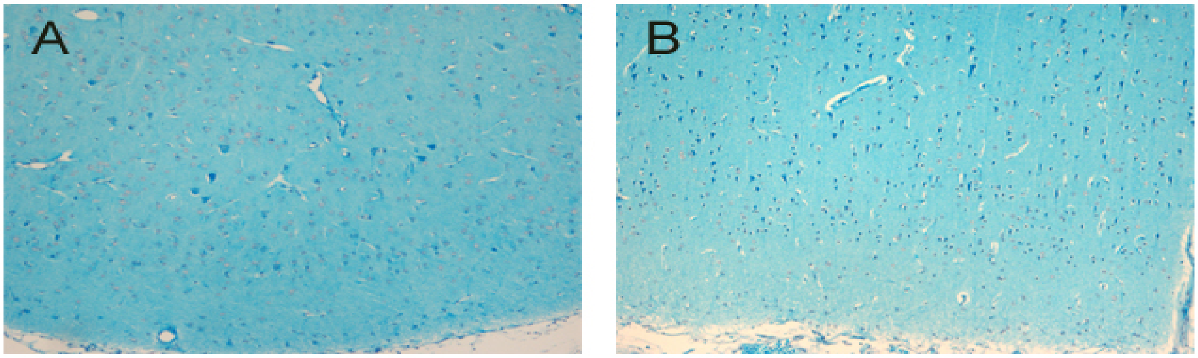

Figure 60. Luxol fast blue stain of cortical tissue of sections (A) from immediately beneath the subdural array, and (B) from a distant to the array site. There is no gross difference in myelination or in neuronal density between the two sections. Both taken at effective x100 magnification.

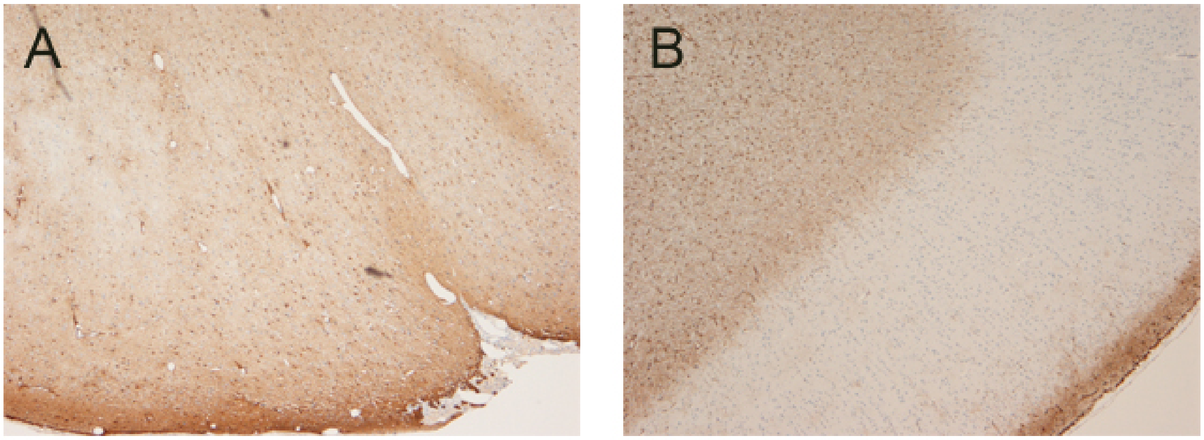

Figure 61. GFAP stain of cortical tissue of sections (A) from immediately beneath the subdural array, and (B) from a distant to the array site. There is increased GFAP reactivity in the section from the implanted site, something that suggests astrocytic activation. Both taken at effective x40 magnification.

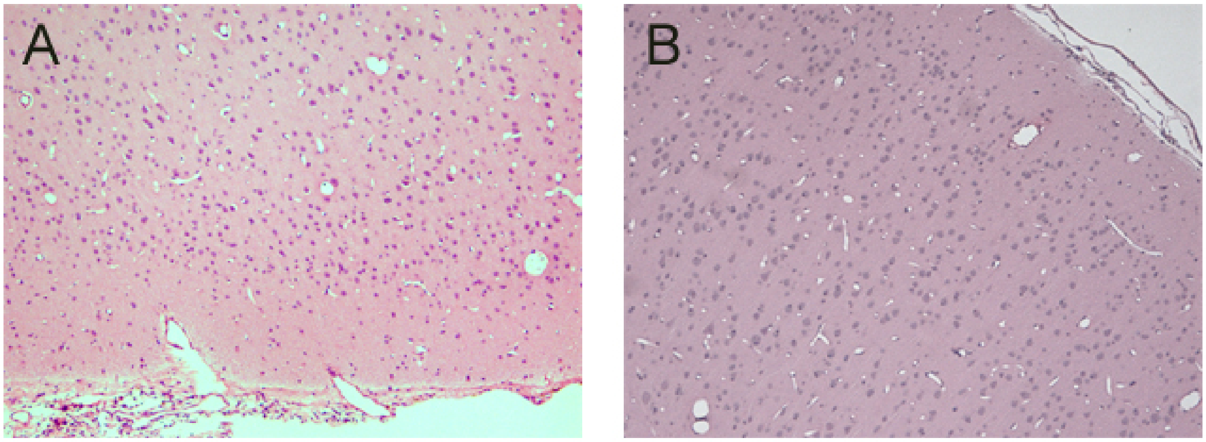

Figure 62. H&E stain of cortical tissue of sections (A) from immediately beneath the subdural array, and (B) from a distant to the array site. There is no gross different in neuronal density between the two sections. Both taken at effective x100 magnification.

Discussion

Effect on the electrode-tissue interface

We found that stimulation caused a transient increase in electrode impedance. This change was manifested as a gradual, within 3-4 minutes, increase in the peak voltage developed by the stimulator (V_{STIM}), in order to deliver each current pulse through the stimulated electrode. When the duration of stimulation was short (6 minutes), impedance returned to pre-stimulation levels within 2-3 minutes. This transient increase in impedance likely reflects the gradual charge accumulation across the capacitive element of the stimulating electrode, similar to the “ratcheting” of electrode potential during improperly charge-balanced electrical pulsing (Merrill et al. 2005). In our case, charge balancing was attempted through the delivery of symmetric, biphasic pulses, which is not ideal under stimulation conditions that exceed the charge-buffering capacity of the electrode. Consistent with this hypothesis, these short-term impedance changes on micro-grid electrodes, with an exposed diameter of 75 µm (small charge-buffering capacity) were significantly larger than on mini-grid electrodes, with an exposed diameter of 2 mm (large charge-buffering capacity). The presence of these short-term impedance changes during stimulation might be indicative of non-Faradaic reactions and should ideally be addressed in long-term stimulation studies. The next section (“effect on cortical excitability”) includes additional discussion on this issue.

After prolonged stimulation (>30 minutes), impedance on the stimulating electrode dropped. That drop was sustained, as it lasted for up to 24 hours post-stimulation. This effect has been described both in vitro (Newbold et al. 2004; Newbold et al. 2010; Newbold et al. 2011) and in vivo (Charlet de Sauvage et al. 1997; Lempka 2010; Weiland and Anderson 2000). In all of those studies, impedance dropped rapidly after stimulation and returned to pre-stimulation levels 12-36 hours later. The mechanism for this impedance change is not clear. An increase in cell membrane permeability through electroporation has been proposed by several authors (Charlet de Sauvage et al. 1997; Ghosh et al. 1993; Newbold et al. 2011; Stolwijk et al. 2011; Wegener et al. 2002). The gradual polarization of the electrode might “clean” the electrode surface of adsorbed proteins and cells, which are considered responsible for causing most of the electrode-tissue interface impedance (Lempka 2010). Electroporation requires large fields, in the order of several hundreds to thousands of V/cm^2. In our experiments, the maximum peak voltage developed during bipolar stimulation was 60-70 V, for stimulus intensities around 5 mA. Given that the interelectrode distance in the micro-grid was 1mm, the generated field was in the 600-700 V/cm^2 range, which is compatible with the occurrence of electroporation phenomena.

In experiments conducted with subdural arrays, the impedance drop was not confined to the stimulating electrode pair. It was largest on the stimulating electrodes and became progressively smaller on electrodes at increasing distance from them. In contrast, the impedance drop was specific to the stimulating electrode pair in epidural arrays. Different current spread with subdural and epidural stimulation might explain this difference. In bipolar stimulation, current density under each stimulating electrode depends on electrode separation; larger separations are associated with steeper decline in current density at increasing distance from the stimulating electrode (Nathan et al. 1993a; Nathan et al. 1993b). Since bipolar stimulation was performed always between adjacent electrodes, the larger interelectrode distance in the epidural arrays (3 mm) compared to that in the subdural arrays (1-2 mm) would explain a more specific, to the stimulating electrode pair, pattern of impedance changes. Another reason may be the different volumes at which current densities above the electroporation threshold are distributed in the subdural and epidural case. Simulations have shown that stimulation through epidural disc electrodes generates a much more spatially limited current spread, both in terms of area and depth, than stimulation through subdural electrodes (Kim et al. 2011). This is probably related to the larger radial distance, as well as the presence of dura and CSF-filled subdural space, between the electrode and the cortex, in the epidural case.

The variations in absolute electrode impedance after stimulation could be related to which electrodes impedance was measured at and/or which electrodes received stimulation. Resolving this requires the construction of a multi-variable linear model, with impedance as the independent variable, and electrode IDs (stimulated or non-stimulated) as two of the dependent variables. Further analysis is needed on this issue.

Finally, it is worth noting that the impedance changes described here are unlikely to be confounded by impedance increases that occur on implanted electrodes with time and are related to reactive tissue response (Williams et al. 2007). It has been found that impedance changes related to tissue reaction occur over the first 2-3 weeks after initial implantation (Ludwig et al. 2006; Vetter et al. 2004). In our case, systematic stimulation began after more than 2 months post-implantation, during which time impedance changes due to tissue reaction should have stabilized.

Effect on cortical excitability

We found that motor-evoked potential thresholds (MEPTs) increased on micro-grid electrodes. The increase in MEPT was maximal immediately after the 30-minute-long stimulation and lasted for 48 hours. It is unlikely that the drop in impedance can explain the rise in MEPT. Constant current stimulators adjust stimulation voltage in order to deliver the same amount of current independently of changes in electrode impedance, unless the required stimulation voltage exceeds the voltage compliance of the stimulator. That would be an, unlikely, result of a rise, rather than a drop in electrode impedance.

Sherrington first described how electrical stimulation itself changed the threshold for evoking movement; he attributed those changes to “facilitation” and “fatigue” of a stable cortical representation (Brown and Sherrington 1912; Leyton and Sherrington 1917). The rise in MEP threshold can be explained, at least in part, by a stimulation-induced decrease in neuronal excitability (termed SIDNE).

SIDNE has been demonstrated with intracortical electrodes (McCreery et al. 1990; McCreery et al. 1997) and with retinal electrodes (Ray et al. 2006). In one of those studies, continuous, high-frequency (20 Hz) intracortical stimulation for 24 hours, at charge densities similar to those used in our study, produced depression of the excitability of pyramidal tract neurons lying close to the stimulating electrode; that depression lasted for 1-4 days (McCreery et al. 1986). In a related study (McCreery et al. 2002) reported that this depression of neuronal excitability can be seen after shorter (4-7-hour long) stimulation sessions, when stimulation is delivered simultaneously through several neighboring microelectrodes, but not when a single electrode is pulsed. They theorized that that could be the result of overlapping electric fields. In our experiments, stimulation was delivered through 2 neighboring surface electrodes, a setup that resembles the multi-electrode intracortical stimulation scheme of the previous study. The mechanism for such an effect is unclear, but it has to be acting on a long-term time scale. It might be related to the production of a chemical agent that exerts its inhibitory action when its concentration exceeds a certain threshold, thus the absence of this effect in single-electrode stimulation (McCreery et al. 2002). It might also be related to a stimulation-induced release of glutamate, which is known to lead to excitotoxic phenomena (Lipton and Rosenberg 1994). It might, finally, be related to a direct toxic effect of large electric fields on neurons (see discussion below).

The amplitude of the effect was marginally related to stimulation rate: 2-Hz stimulation was associated with a larger, but marginally significant, increase in MEPT than 5-Hz stimulation. When, in separate sessions, stimuli were delivered at suprathreshold intensity, the amplitude of MEPs at the end of a 2-Hz stimulation session had shown a larger decrease from baseline than a 5-Hz session (Figure 16). The effect of stimulation rate on stimulation-induced cortical inhibition or excitation is not clear. Some studies have shown that stimulation rates below 100-150 Hz lead to increased excitability (Priori and Lefaucheur 2007; Yazdan-Shahmorad et al. 2011a) (but see (McCreery et al. 2002)), whereas higher rates are associated with cortical inhibition (Anderson et al. 2007; Tranchina and Nicholson 1986;

Yazdan-Shahmorad et al. 2011a). In a different cortical stimulation modality, repetitive transcranial magnetic stimulation (rTMS) at very low frequency (1 Hz) causes prolonged depression of cortical excitability (Chen et al. 1997), whereas rTMS at higher rates (>3-5 Hz) leads to cortical excitation (Pascual-Leone et al. 1994). It is unclear, however, whether repetitive cortical surface stimulation has a similar effect on cortical excitability as rTMS.

Our results are compatible with a reduction in cortical excitability seen at low stimulation rates. What could be the mechanism for a rate-dependent effect? According to a model (Tehovnik et al. 2006; Tolias et al. 2005; Tranchina and Nicholson 1986), delivery of a depolarizing stimulus is immediately followed by a brief increase in the probability of firing, and later by a longer lasting decrease in the probability of firing. This could be related to the different local distributions and kinetics of excitatory and inhibitory postsynaptic potentials in the immediate vicinity of single pyramidal cells: local excitatory PSPs appear first after an action potential of a pyramidal cell but last for a brief period, whereas the more numerous inhibitory PSPs appear later but last longer (Douglas and Martin 2004; 2007). Stimulating at very low frequencies would allow more inhibition to manifest itself, whereas at higher frequencies the balance would shift towards excitation. At very high frequencies (>100-150 Hz), synapses might fail to depolarize fast enough to follow the stimulus train, resulting in recurrent hyperpolarization (Anderson et al. 2007).

A long-lasting rise in MEPTs could also be, partially, explained by stimulation-induced loss of cortical neurons. Several studies have examined the effect of chronic electrical stimulation on cortical histology (Geddes and Roeder 2003b; McCreery et al. 2010; McCreery et al. 1990; van Kuyck et al. 2007; Weiland and Anderson 2000; Wilks et al. 2009). They determined that for certain ranges in the stimulation parameters, neuronal injury and loss of neurons close to the stimulating electrodes occur. It has been proposed that neuronal loss might be caused by stimulation-induced production of cytotoxic chemical species (McCreery 2004). These species are generated when charge injection exceeds the capacitive (charge storage) limit of the electrode and increasingly involves net electrode transfer (charge dissipation) across the electrode-tissue interface. Depending on the electrode material, which determines the kinetics of the electron transfer reactions, the net effect of charge dissipation can be either reversible oxidation, or irreversible corrosion. Both these “Faradaic” reactions are damaging to the tissue.

“Safety margins” for charge injection depend on a variety of factors, including electrode material, exposed electrode area, impedance, stimulus waveform shape, stimulation frequency, duty cycle type (continuous or intermittent) and duration of stimulation (Shannon 1992; Weiland and Anderson 2000). Pure platinum electrodes have been shown to undergo Faradaic reactions at relatively low charge densities, whereas platinum-iridium alloys at higher charge densities (Geddes and Roeder 2003b). Charge densities used in our experiments ranged between 0.0035 and 0.1 Cb/cm^2 for the micro-grid array (made of platinum-iridium), and between 2.5 x 10^{-7} and 2 x 10^{-6} Cb/cm2 for the mini-grid array (made of platinum). The charge densities used in the micro-grid stimulation experiments exceeded the safety limits by a wide margin (Shannon 1992). Therefore, it is very likely that the increase in MEP thresholds seen in the micro-grid stimulation experiments was, at least in part, due to stimulation-induced neuronal loss. In contrast, charge densities in the mini-grid experiments were likely within safe limits. Neural injury may have only been a small contributing factor to the moderate increases in MEP thresholds seen in the mini-grid stimulation experiments.

Interestingly, no apparent decrease in neuronal density was seen in the cortical area underneath the micro-grid array, in one of the animals that was examined histologically. It is unclear whether neuronal loss that would lead to increased MEP thresholds would manifest itself histologically. The discrepancy may, however, be due to the stain used; H&E is a cellular stain, and even though it generally stains large pyramidal cells in the deep layers well, it is missing a larger proportion of the smaller cells in the more superficial molecular and granular layers (Bancroft and Gamble 2007). Those layers might be affected more by cortical stimulation, as they are physically closer to the subdural stimulating electrodes.

Effect on spontaneous cortical activity

The immediate, stimulus-evoked, effects of electrical stimulation, especially intracortical, on neuronal activity are well documented (Histed et al. 2009; Jankowska et al. 1975; Logothetis et al. 2010; McCreery et al. 1986; Stoney et al. 1968; Strick 2002; Tehovnik 1996; Tehovnik et al. 2006; Tolias et al. 2005). In short, each pulse activates, both directly and synaptically, cells and fibers within a small volume around the electrode; distant cells can be activated trans-synaptically, provided they have connections to the stimulated site. Regarding the stimulus-evoked effects of ECS, (Gwinn et al. 2008) reported that ECoG power increased immediately after brief, 50-Hz stimulus trains, until about 5 sec later; that increase involved primarily high frequencies (>40 Hz). Similarly, (van 't Klooster et al. 2011) found that ECS caused a transient (about 50 ms long) increase in the power of high-frequency ECoG. (Valentin et al. 2002) described high-frequency cortical responses, spikes and ripples, evoked by single pulse ECS. Finally, a small number of studies characterized the high-frequency after-discharges that follow ECS (Lesser et al. 1999; Lesser et al. 1984). Here, we report that power of high frequencies increases after prolonged stimulation as well, in which case it is more persistent, as it doesn’t return to pre-stimulation levels until at least 24 hours later. At the same time, power in low frequencies drops.

It has been suggested that high frequency ECoG potentials might be reflecting preferentially neuronal and synaptic activity in the outer cortical layers (e.g. Zanos 2009 and references therein). On the other hand, ECoG signals in frequencies below 30 Hz are thought to reflect activity in longer range cortico-cortical and thalamo-cortical oscillating circuits, both of which involve the large pyramidal cells of the deeper cortical layers (Steriade 2005). According to modeling and experimental studies, cathodal stimulation of the cortical surface preferentially excites neurons and fibers that extend parallel to the electrode surface and has minimal effect on neural elements that extend perpendicular to the electrode surface (Manola et al. 2007; Nitsche and Paulus 2000; Wongsarnpigoon and Grill 2008; Yazdan-Shahmorad et al. 2011a; Yazdan-Shahmorad et al. 2011b). Superficial layers contain neuronal elements that are oriented mostly parallel to the cortical surface, whereas the deeper, pyramidal layers contain elements that lie mostly perpendicular to the cortical surface (Braitenberg and Schuz 1991; Brodmann 2009).

The pattern of ECoG power changes observed in our experiments could be explained if, in addition to producing SIDNE (discussed in the previous section), the net effect on the underlying cortex of bipolar stimulation resembles that of cathodal stimulation. Cells in superficial layers, contributing to high ECoG frequencies, get excited by surface stimulation and power in those frequencies increases. Cells in deeper layers, contributing to lower ECoG frequencies, are subjected to the effects of SIDNE without receiving sufficient excitatory drive from surface stimulation and, as a result, power in those frequencies decreases.

The effects of bipolar stimulation on the cortex underlying each of the two electrodes resemble those of anodal or cathodal unipolar stimulation, depending on which electrode is used as anode or cathode. In our experiments, bipolar stimulation was delivered through neighboring electrodes (1, 2 or 3 mm apart). In this case the two fields overlap to a large extend and it is harder to predict theoretically what the net effect of stimulation will be on the underlying cortex (Nathan et al. 1993a; Wongsarnpigoon and Grill 2008). Our findings suggest that the effects on cortical physiology of bipolar stimulation through neighboring electrodes, a technique commonly used in clinical practice (Duffau 2007), might resemble those of cathodal, unipolar stimulation.

Finally, it is worth noting that these effects were observed when stimulation was delivered independently of cortical activity and while the monkeys were resting. It is not clear whether similar effects would have occurred had stimulation been delivered during free behavior, in which case some stimuli would have been delivered during movement. The effect of stimulation on cortical excitability is dependent on the level of cortical excitability at the time of stimulation (Pell et al. 2011): larger, percentage-wise, suppression in excitability is seen when excitability is already high. Based on that, stimulation delivered during movement would be expected to produce more pronounced suppression in cortical excitability.

Chapter 4: Changes in cortical connectivity induced by cycle-triggered stimulation during cortical oscillations

Introduction

Cortical plasticity encompasses the molecular, cellular, synaptic and circuit processes that lead to changes in the structure and function of cortical networks and in the functional relationship of those networks with sensory stimuli or motor responses. An essential feature of cortical plasticity is its dependence on modification of synapses between neurons (synaptic plasticity). Synaptic plasticity is neural activity-dependent. That means that sensory stimuli or motor responses, through their associated neural activations, can themselves induce or alter cortical plasticity, by changing the efficacy of synaptic transmission between neurons. At the synaptic level, one type of synaptic plasticity requires tight temporal association between pre- and post-synaptic neuronal activity. Synaptic plasticity can be induced experimentally by appropriate delivery of electrical stimulation of the pre- and/or post-synaptic neurons.

Activity-dependent cortical plasticity is prominent during development, resulting in the normal maturation of neural circuits. It is, however, not limited to development; it persists throughout the organism's lifetime. It is the substrate for learning and memory, the basis for the organism's ability to adapt in response to a changing environment. Adult plasticity is also central to functional recovery after an injury that involves the nervous system. In this last case, activity-dependent plasticity is part of an array of adaptive responses that can limit the sensory or cognitive deficit or motor disability caused by the injury.

We are interested in methods for inducing and controlling cortical plasticity *in vivo*, by delivering electrical stimuli to the cortex, contingent upon the detection of different types of cortical neural activity. A mode of cortical activity whose function remains controversial is cortical oscillations, the periodically modulated level of activity of neurons in one or more cortical areas. Cortical oscillations have been suggested to play a role in synaptic transmission and in vivo synaptic plasticity. Using oscillatory signals to trigger the delivery of electrical stimulation could elucidate the role of oscillations in cortical function and the in vivo mechanisms of cortical plasticity. In addition, such methods could contribute to the development of treatments for the consequences of neural injury. In order to increase the clinical relevance of these methods, we deploy minimally invasive electrode arrays to record cortical activity and to deliver electrical stimuli to the cortex.

Background

Cortical oscillations and synaptic transmission

An oscillatory wave in the 8-12 Hz range was the first electroencephalographic pattern described, in Berger's original work on the human EEG in 1923. Since then, a variety of cortical oscillatory phenomena have been described in different animal species, in almost every cortical and subcortical structure, under different arousal, behavioral, cognitive and pathological conditions (e.g. Niedermeyer 2005). Oscillations can be found in single cell membrane potentials and firing patterns, extracellular local field potentials and potentials recorded from the surface of the brain or from the scalp. The cortex, with its densely interconnected neuronal networks and its extensive recurrent connections with subcortical structures exhibits a wide range of oscillations, from 0.05 Hz to 500 Hz (Buzsaki and Draguhn 2004). The average amplitude of oscillatory components in the cortical field potential is inversely proportional to their frequency (Freeman et al. 2000). This property may be related to the different sizes of cortical networks recruited by oscillations at different frequencies: large neuronal populations at lower frequencies, smaller neuronal ensembles at higher frequencies (Csicsvari et al. 2003; Grenier et al. 2001).

Cortical oscillations can influence computation in local networks (e.g. Havenith et al. 2011) and affect long-range communication between cortical sites (e.g. Fries 2005; Rubino et al. 2006). Depending on their frequency, oscillations may play a role in coordinating the formation of ensembles of neurons across smaller or larger cortical areas that result in the formation of functional neural networks of various scales (Canolty et al. 2010; Engel et al. 1991a; Fetz et al. 1991; Harris 2005; Jackson et al. 2003; Lakatos et al. 2008; Varela et al. 2001). The relationship between oscillations in the extracellular field and ongoing neuronal activity has been documented in various cortical areas, and for oscillations of different frequencies. That relationship is usually that of “phase preference”: cell activity tends to occur during certain, preferred, phases of the ongoing oscillations and to be sparse during other, anti-preferred, phases. Phase of low frequencies, like theta (2-4 Hz), has been found to modulate neuronal activity in the hippocampus and its temporal relationship with activity of cells in the neocortex (Sirota et al. 2008). Phase of higher frequencies, like gamma (>30 Hz), modulate cell activity and cell to cell interactions in the hippocampus (Colgin et al. 2009), parietal cortex (Pesaran et al. 2002) and visual cortex (Engel et al. 1991a; Engel et al. 1991b; Womelsdorf et al. 2007).

Intermediate frequency oscillations, in the beta range (15-25 Hz), have been similarly documented in various cortical areas, including the visual cortex, the primary auditory cortex and, particularly, the sensorimotor (SM) cortex (Engel and Fries 2010). Murthy & Fetz (Murthy and Fetz 1996a; b) were among the first to describe those oscillations in the local field potential from the SM cortex and their association with changes in neuronal activity. First, they found that episodes of phase-coherent beta oscillations occurred across large areas of the SM cortex. During these oscillatory episodes, many SM cells tended to fire at or shortly before the (negative) trough of the field potential. During those episodes, entrained neurons tended to fire synchronously; such cells were often found over large distances in SM cortex, many of them in different hemispheres. Similar findings have been reported by several groups (Baker et al. 1999; Canolty et al. 2012; Canolty et al. 2010; Donoghue et al. 1998; Rubino et al. 2006).

Even though the cellular and network mechanisms for these oscillations are unclear, coherent oscillatory activity in the beta range may have an effect on synaptic transmission and, possibly, synaptic plasticity. By obtaining simultaneous recordings of extracellular fields and spikes and intracellular membrane potentials in the SM cortex of awake monkeys, (Chen 1993b; Fetz et al. 1991) showed that spike-triggered, subthreshold membrane potentials showed larger deflections when spikes occurred during oscillatory episodes in the beta range than when they occurred outside such episodes. This means that, during oscillations, there was an increased number of synchronous post-synaptic potentials, mostly excitatory. Additionally, LFP cycle-triggered averages of membrane potential trajectories showed that during these oscillatory episodes, the membrane potential of individual cells was generally in-phase with the extracellular oscillatory potential, whereas outside the episodes the correlation between intracellular and extracellular potential was much weaker (Chen 1993a). This again pointed to an increased number of synchronous postsynaptic potentials during oscillatory episodes that entrained cells in the network-wide oscillation. Beta oscillatory episodes might, therefore, represent times when network activity has an enhanced effect on the excitability of single cells, through the temporal summation of synchronous postsynaptic potentials (Okun et al. 2010).

In order to directly test that hypothesis, we triggered the delivery of cortical stimulation at a cortical site (C_{STIM}) on different phases of the ongoing beta oscillation at another, nearby, site (C_{TRIG}), during episodes of increased beta amplitude in two awake macaque monkeys. Repeated association of a negative ("depolarizing") beta phase in C_{TRIG}, indicating increased presynaptic activity, with stimulus-induced postsynaptic depolarization of C_{STIM}, would be expected to produce synaptic potentiation of connections from C_{STIM} to C_{TRIG}. In contrast, association of a positive ("hyperpolarizing") beta phase in C_{TRIG} (indicating decreased presynaptic activity) with stimulus-induced postsynaptic depolarization in C_{STIM}, would be expected to produce synaptic depression.

In order to estimate changes in the efficacy of synaptic transmission between C_{TRIG} and C_{STIM}, we used two methods, one based on cortical excitability and the other on spontaneous cortical activity.

Assessing cortical connectivity via cortically-evoked potentials

Synaptic interactions between 2 neurons (from A to B) can be directly inferred by calculating cross-correlograms (CCs) of spike trains generated by the 2 cells, or by compiling averages of membrane potential of cell B, triggered on spikes from cell A (Fetz et al. 1991). In the latter case, an A→B excitatory synaptic projection would manifest itself as an excitatory post-synaptic potential (EPSP) in cell B, at some time after spikes of A. An indirect way of measuring synaptic interactions is to deliver electrical stimuli in the vicinity of cell A, while recording the membrane potential of cell B, or simply its extracellular spikes. Stimuli will activate cell A, which in turn will generate EPSPs in cell B and increase the probability of cell B firing. This technique has been used to infer mono- or polysynaptic projections between different cortical areas e.g. (Asanuma and Rosen 1973; Curtis 1940; Fanardjian and Papoyan 1995; Hess et al. 1996; Sil'kis and Bogdanova 1999).

Similarly, stimulus-evoked extracellular fields can be used to study projections between cortical areas (Curtis 1940; Kikuchi et al. 2012; Luppino et al. 1993; Matsumoto et al. 2012; Matsumoto et al. 2007; Richardson and Fetz 2012). In nonhuman primates, cortically-evoked potentials (CEPs) have been shown to occur between brain areas that have known anatomical connections, e.g. between homologous motor cortices of the two hemispheres (Curtis 1940; Richardson and Fetz 2012), or between ipsilateral supplementary and primary motor cortices (Luppino et al. 1993; Richardson and Fetz 2012). In humans, CEPs, evoked and recorded through surface cortical electrodes, have also been shown to occur between anatomically connected areas, e.g. between anterior and posterior language areas (Enatsu et al. 2013), between supplementary and primary motor cortices (Kikuchi et al. 2012; Matsumoto et al. 2007), and between parietal and frontal regions (Matsumoto et al. 2012).

We hypothesized that the occurrence of stimulation-induced changes in the magnitude of such CEPs would imply that stimulation has altered the efficacy of synaptic transmission between the site at which the CEP is elicited towards the site from which the CEP is recorded.

Assessing cortical connectivity via phase coherence

Another method for assessing connectivity between two cortical areas, using spontaneously occurring field potentials, is coherence, first applied to scalp EEG recordings (e.g. Freeman 1961; Gevins et al. 1981; Livanov et al. 1964). Coherence is a measure of the similarity between two extracellular field signals at a given frequency, by quantifying how consistent their phase difference at that frequency is, independently of signal power (Carter 1987; Rosenberg et al. 1989; Schlogl and Supp 2006). It provides a measure of the strength of association between neuronal activities at two different sites (Rosenberg et al. 1989; Schlogl and Supp 2006) and, therefore, their effective connectivity. Because, in the classic case, coherence is computed from longer records of spontaneous cortical activity, it allows us to evaluate whether potential connectivity changes have an effect on naturally-occurring, rather than stimulus-evoked, cortical activity and whether they are persistent in time.

We hypothesized that the degree of coherent field activity from two sites is representative of the efficacy of synaptic transmission between them; it follows that stimulation-induced changes in field coherence would reflect concomitant modification of the synaptic connection between these two sites.

Methods

Two animals were used in this study, both of them male pigtailed macaques (Macaca nemestrina), aged 3 and 4 years old and weighing 5.8 and 6.3 kg, respectively.

Behavioral tasks

Each monkey was trained in two tasks that were performed at different stages of the experiment.

Visually-cued bimanual task

The monkey sat in a primate chair, in front of a computer screen, with both its forearms comfortably resting on the sides and flexed at the elbows. Both wrists were restrained and an accelerometer (MMA7341L, Pololu Robotics and Electronics) was taped to the back of each hand. A cursor, one for each hand, represented the root mean squared output of each accelerometer. At the beginning of each trial, both cursors had to be held inside a “rest box” at the bottom of the screen, by not moving either hand. The visual cue consisted of either the left or right rest box moving from the bottom of the screen to the top of the screen. The monkey then had to make a hand movement (usually consisting of a wrist extension) to move the cursor to the target box, without having to hold it in the target: once the cursor was moved into the target box the trial was over. During that time, the monkey had to keep its other hand still with the cursor in its rest box. The monkey needed to successfully complete four trials in a row before it received an applesauce reward. Left- and right-movement trials were randomly interleaved. The monkey performed this task during the baseline ECoG recording sessions, before and after conditioning.

Arm-resting task

The monkey sat calmly in the primate chair and was rewarded for not generating hand movements. That was accomplished by keeping both hand acceleration-controlled cursors inside their respective “rest boxes” for at least 10 seconds. The monkey performed this task during the conditioning stimulation sessions.

Surgical procedures and implants

All procedures were approved by the University of Washington Institute for Animal Care and Use Committee. On the day of surgery, each monkey was anesthetized with sevoflurane gas.

Epidural implants

A midline scalp incision was made and the scalp was resected. The epidural electrodes were implanted through individual 0.5mm burr holes drilled with a stereotaxic drill. In monkeys I and K the electrodes were located over the primary motor cortex (M1). In monkey I, there were additional electrodes over the supplementary motor cortex (SMA). Monkey I received a total of 9 M1 electrodes and 3 SMA electrodes on each hemisphere. Monkey K received a total of 9 M1 electrodes on the left hemisphere.

The epidural electrodes were made with 9mm cut length of platinum rod (AM Systems #711000, 0.254 mm diameter) insulated with heat-shrink Pebax (Small Parts #B0013HMWJQ). Pebax was cut so that the exposed tip was ~0.5 mm. Correspondingly, the surface area of the exposed electrode tip was ~0.06 mm^2.

Recording

The ECoG recordings comprised signals from all cortical electrodes. Those were recorded single-ended (relative to tissue ground) using two 16-channel ZC-16 headstages (Tucker-Davis, Alachua, FL) and two 16-channel, DC-coupled g.USB amplifiers (g.tec medical engineering Gmbh, Schiedlberg, Austria). Sampling of signals was done at 24 bit resolution, sampled at 4.8 Ksamples/sec, with no filtering. Data from the amplifiers were streamed to a personal computer through a USB link, then stored and visualized in real-time using a Simulink-based (MathWorks, Natick, MA) graphical user interface, developed in-house. A trigger signal, sampled simultaneously on each of the amplifier units, was used to align recordings at the analysis stage.

Electrical stimulation

Electrical stimuli were delivered to a pair of cortical electrodes (bipolar stimulation) through a biphasic stimulus isolator (BSI-1, BAK Electronics, Stanford, FL), driven by a pulse generator (Master-8, A.M.P.I., Jerusalem, Israel). The pulse generator was triggered by the computer running Simulink-based custom-made software. Each stimulus was a biphasic, symmetric pulse, of 0.2ms pulse width.

Closed-loop stimulation

The closed-loop system comprised an amplifier, a personal computer (PC) and the stimulator (Figure 1). ECoG signals were recorded by the amplifier and collected by and stored on a PC. The PC was simultaneously running custom-made Simulink software that implemented a real-time display, a 4th-order band-pass (BP) filter and a dual time-amplitude window discriminator (Figure 2). By selecting the ECoG channel and the corner frequencies of the BP filter, and appropriately setting the timing and amplitude parameters for the discriminator, the investigator was able to program the PC to generate triggers on specific phases of ongoing ECoG oscillations of a specific frequency, on a given channel. Those triggers were used in real-time to trigger the delivery of single-pulse, conditioning stimuli to a pair of cortical electrodes. When no oscillatory episodes occurred, test stimuli, of the same amplitude, duration and shape as the conditioning stimuli, were delivered at a constant rate of 2 Hz (Figure 3). The timing of all conditioning and test stimuli was registered; the exact sequence of those stimuli would then be repeated during a subsequent, control, stimulation session.

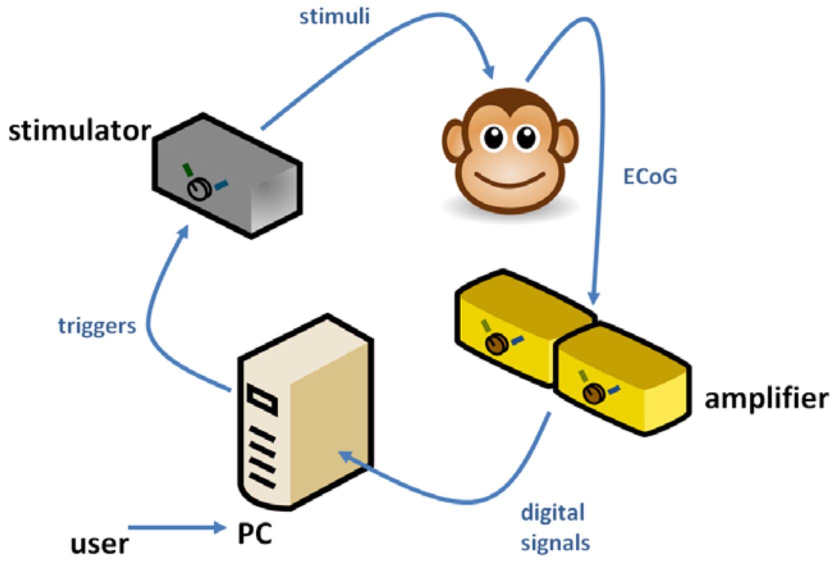

Figure 63. Schematic diagram of the closed-loop recording and stimulation system. ECoG signals are recorded on an amplifier, and transferred in real time to a personal computer. The user, in real time, sets the parameters for the detection of ECoG oscillations. Upon the detection of those oscillations, the computer triggers the stimulator which, in turn, delivers stimuli to the monkey's brain.

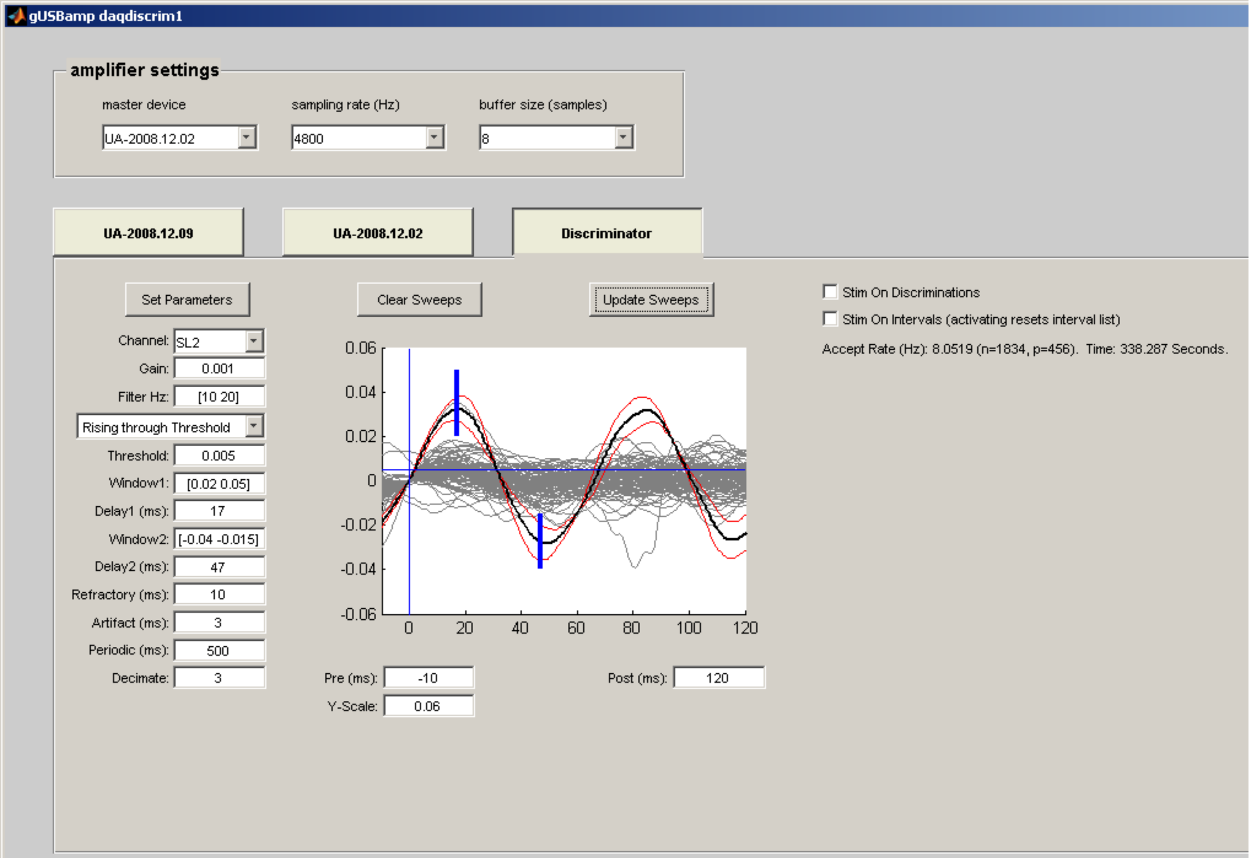

amplifier settings

master device: UA-2008.12.02
sampling rate (Hz): 4800
buffer size (samples): 8

Channel: SL2
Gain: 0.001
Filter Hz: [10 20]
Rising through Threshold
Threshold: 0.005
Window1: [0.02 0.05]
Delay1 (ms): 17
Window2: [-0.04 -0.015]
Delay2 (ms): 47
Refractory (ms): 10
Artifact (ms): 3
Periodic (ms): 500
Decimate: 3

Pre (ms): -10
Post (ms): 120
Y-Scale: 0.06

☐ Stim On Discriminations
☐ Stim On Intervals (activating resets interval list)

Accept Rate (Hz): 8.0519 (n=1834, p=456). Time: 338.287 Seconds.

Figure 64. Screenshot of the graphical user interface used to set parameters for the detection of ECoG oscillations in real time. At the top, there are settings related to the recording and data transfer. The "discriminator" tab involves a number of settings to the left, a display window in the middle, and a set of switches to the right. The user can select the amplifier channel on which the discriminator operates and set the gain, the corner frequencies of a band-pass filter, a number of variables for the dual time-amplitude window discriminator and the period of test triggers, which are delivered periodically when no detection events occur. In this example, the discriminator generates triggers at the trough of ~17 Hz oscillations that occur on that channel.

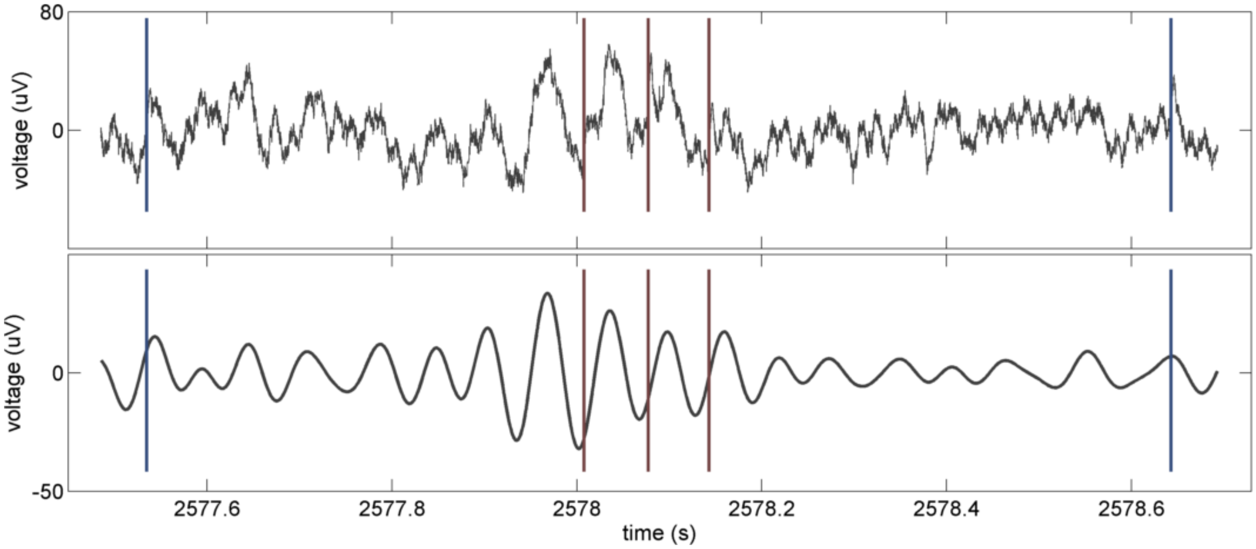

Figure 65. Burst of 3 conditioning stimuli, triggered from beta band (~18 Hz) ECoG oscillations from site placed over the SMA. (Top) Raw ECoG signal showing the 3 conditioning stimuli (red vertical lines), occurring around the trough of successive beta band cycles; the test stimuli (blue vertical lines) delivered before and after the burst are also shown. Stimulus artifacts were blanked out from the raw traces. The CEPs occurring immediately after most of the stimuli can be seen as well. (Bottom) Band-pass filtered ECoG (12-25 Hz corner frequencies) as "seen" by the discriminator algorithm. Only oscillatory episodes exceeding a threshold triggered stimuli. Notice the variability in the phases of the beta oscillation at which the conditioning stimuli are delivered.

Experiment timeline

Activity-dependent conditioning experiments

Before any conditioning experiment, “CEP connectivity maps” were generated, by identifying on which cortical sites cortical potentials were evoked when a given site was stimulated. That was done to select pairs of C_{TRIG}-C_{STIM} for the closed-loop experiments: for a given C_{STIM}, $_{CTRIG}$ site was selected randomly among those sites on which CEPs had been consistently evoked during the “mapping” procedure. Oscillatory activity on C_{TRIG} was used to trigger the delivery of single-pulse stimulation of C_{STIM}. Each of the stimuli delivered to C_{STIM} elicited CEPs at several recording sites, including C_{TRIG}. Since the amplitude of those CEPs reflects the effective connectivity between C_{STIM} and the recording sites with CEPs, we were able to simultaneously perform the conditioning and test its effects.

Each experiment (Figure 4) started with a 15 to 30-minute-long “pre-stimulation” baseline recording session of all ECoG signals, while the monkey was engaged in the cursor-tracking task. The conditioning stimulation session followed, that comprised 3 stages: (1) continuous test stimuli, 2 Hz rate, for 5 min, (2) activity-dependent conditioning (cycle-triggered and test stimuli), for 30 min, (3) continuous test stimuli, 2 Hz rate, for 5 min. ECoG activity at all cortical sites, except the two that received stimulation, was simultaneously recorded. The stimulation session was followed by a 15 to 30-minute-long “post-stimulation” baseline recording. For most of the conditioning sessions, control stimulation sessions were performed on separate days. Control stimulation consisted of the same sequence of stimuli delivered during the associated conditioning session, this time independently of ongoing oscillatory activity.

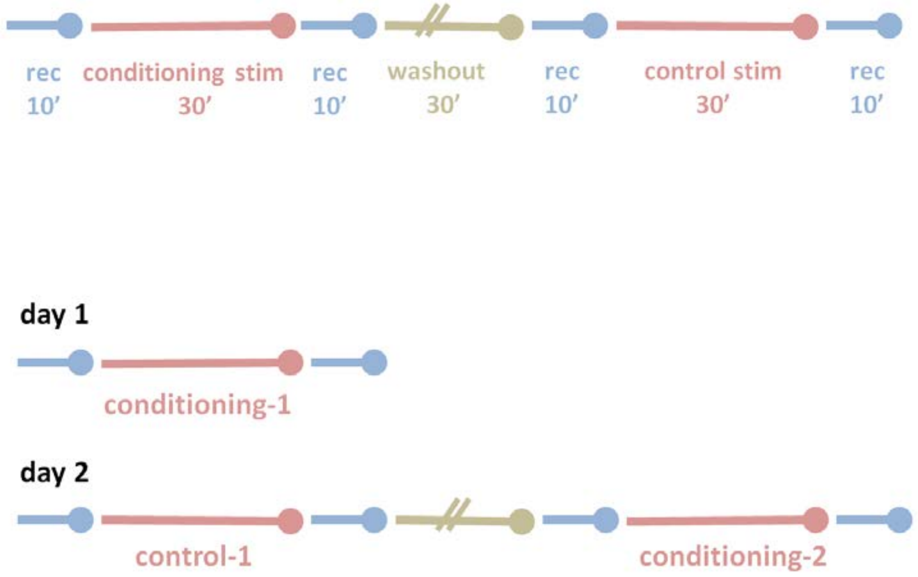

Figure 66. Schematic of the timeline of a typical closed-loop experiment. See text for details. Abbreviations: rec: recording session, stim: stimulation session.

Analysis

Cortically-evoked potentials

Stimulus-triggered sweeps of Laplacian-derived ECoG activity on all sites, except the ones that received stimulation, were compiled. From selected subsets of those sweeps, stimulus-triggered averages of evoked ECoG activity (cortically-evoked potentials, CEPs) were generated; those CEPs were then used to assess the effects of conditioning on effective connectivity. To assess the effect of bursts of conditioning stimuli, cortical responses to test stimuli delivered immediately before bursts were compared to responses to test stimuli delivered immediately after bursts. Bursts of 2, 3, 4 or 5 successive stimuli, i.e. with inter-stimulus intervals less than 75 ms, were studied separately. To assess the duration of conditioned effects, we registered cortical responses to test stimuli delivered 0.5, 1, 1.5 and 2 seconds after the conditioning burst.

To assess whether there was a significant difference in the CEP amplitudes between two sets of test stimuli and, if so, at which times after the stimulus, we used a randomization-based, non-parametric method for making within-subject, between-condition, event-related potential comparisons (Greenblatt and Pflieger 2004).

Because of the presence of stimulus artifact in the first 1-4 ms after the stimulus in approximately 30% of the experiments, the amplitude of a CEP was defined as the maximum (positive or negative) deflection from baseline (0 to 5 ms pre-stimulus) between 8 and 30 ms post-stimulus, i.e. the amplitude of the second phase of the CEP (Figure 5).

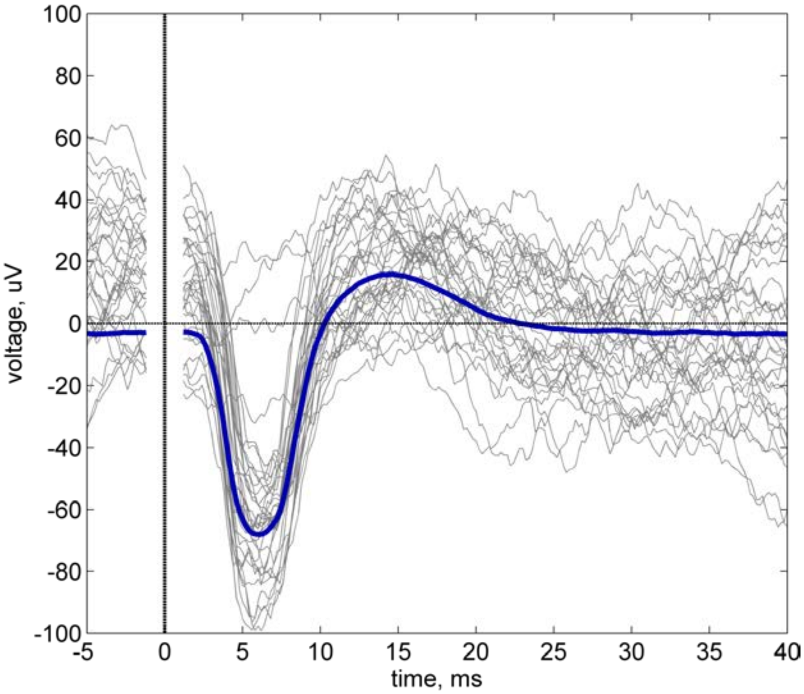

Figure 67. Typical example of individual cortical responses to cortical stimuli and the cortically-evoked potential calculated by averaging approximately 1400 of those (blue curve). Time t=0 corresponds to stimulus delivery. In this example, MEP amplitude was calculated as the maximal positive deflection from baseline at around 15 ms latency.

Coherence

Before any analysis, raw ECoG signals were visually inspected and segments affected by artifacts were removed; channels showing artifacts were also excluded. A third-order, zero-phase, band-pass elliptic filter, with corner frequencies between 1 Hz and 1200 Hz was applied, to remove very slow oscillations and prevent aliasing.

Coherence is defined for pairs of signals, recorded at pairs of sites. We first created a pool of trials by arbitrarily segmenting the entire recording into 1-s long segments. We then estimated the magnitude squared coherence Cxy(f) spectrum for a pair of signals, for each trial. The coherence is a function of the power spectral density Pxx(f) and Pyy(f) and the cross-power spectral density Pxy(f):

$$Cxy(f) = \frac{|Pxy|^2}{Pxx * Pyy}$$

The power spectral density function was computed using Welch's averaged periodogram method with 50% overlapping Hamming windows, of 1024 samples each.

By averaging Cxy over all trials we obtained an estimate of the coherence spectrum for that pair of sites, across frequencies between 1 Hz and 1200 Hz.

In order to assess the amount of coherence attributed to random signal variability, since for any pair of non-infinite random signals the coherence will on average be non-zero, we used a randomization-based method (Maris et al. 2007). One of the two signals in each pair was shuffled in the time domain, while the other signal was left unchanged. Coherence was then computed as described above. This was performed a total of 100 times, resulting in a population of mean "random" coherence spectra. The lower and upper 95% percentiles of random coherence values for a given frequency were used as the confidence intervals, for that frequency. Coherence values that exceed the confidence intervals were considered significantly different than what would be expected by chance.

We wanted to calculate the difference in the mean coherence spectra of a given pair of sites between recording sessions (i.e. before and after stimulation). At the same time we wanted to assess at what frequencies that difference exceeded chance levels. For that, we initially assigned each trial from each of the two conditions (recording sessions), randomly to one or the other condition. We then computed the random difference spectrum, by subtracting the mean, over all trials, spectra from the two "surrogate" conditions. To construct a distribution of the random difference spectrum we performed that procedure 100 times; 95% confidence intervals (for all frequencies) were then calculated for the "real" difference in the mean coherence spectra between the two conditions.

We then calculated the scalar coherence (Cs) for a number of frequency ranges: 2-4 Hz (delta), 4-8 Hz (theta), 8-13 Hz (alpha), 15-25 Hz (beta), 30-50 Hz (gamma), for each trial (i) and pair of sites (xy):

$$\mathrm{Cs}(i) = \frac{1}{N}\sum_{\varphi 1}^{\varphi N} Cxy(n)$$

where n=ϕ_1 …,ϕ_n are the N discrete coherence values within that frequency range. Scalar coherence is the average of the coherence values at each of the frequencies within a given frequency range.

In order to assess whether conditioning had an effect and, if so, what the time course of that effect was, on scalar coherence of pair of sites, we segmented each of the two recording sessions (before and after conditioning) into 5 time segments, of the same duration. From each of those segments, we extracted as many 1-second-long trials as possible and calculated the scalar coherence for each trial. Using repeated measures ANOVA, we were able to assess whether scalar coherence, at a given frequency range, was stable across all 5 segments of the pre-conditioning recording; likewise, we were able to assess whether scalar coherence changed with time during the duration of the post-conditioning recording. Finally, by comparing scalar coherence during the last pre-conditioning segment with that during the first post-conditioning segment, we were able to assess the effect of conditioning on coherence; that comparison was done using t-test. Since scalar coherence was computed for a total of 5 frequency ranges, the statistical significance level for each comparison was Bonferonni-corrected.

Stimulus phase difference

The stimulus phase difference (SPD) for an oscillatory episode, between C_{TRIG} and another control site (C_{CON}) was calculated as the average of the phase differences associated with individual stimuli in that episode (Figure 6). The phase difference for an individual stimulus was calculated using the time shift between the two oscillatory signals, at C_{TRIG} and C_{CON}, at the time of stimulation and the average period of the corresponding cycle of the two signals. The average SPD between C_{TRIG} and C_{CON} for a given experiment was then calculated as the mean of SPDs for all bursts in that experiment.

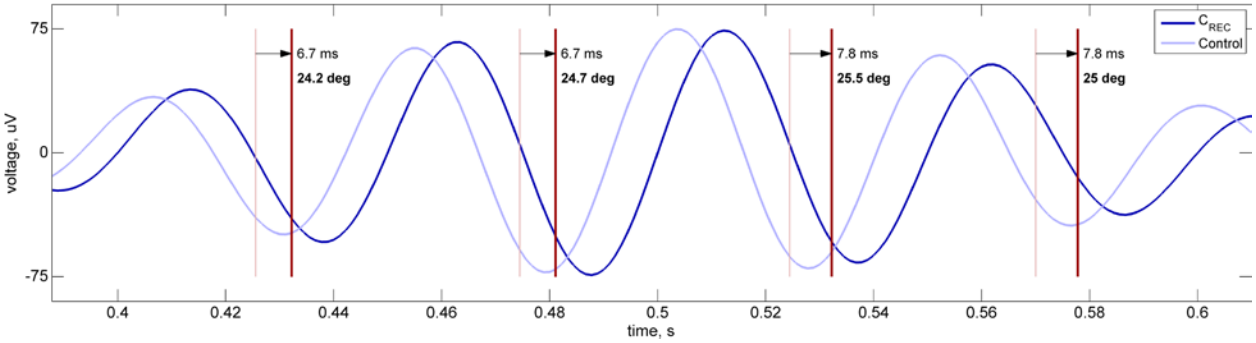

Figure 68. Method for calculating stimulus phase difference between the triggering site (Crec) and another, control site (Ccon), for an oscillatory episode. Shown are the (filtered) voltage traces from Crec and Ccon, which lied at a radial distance of 18mm from $C_{TRIG,}$ along with the times when 4 stimuli were delivered at a phase of approximately 230 degrees (dark red vertical lines). The time shift between Crec and Ccon was calculated for each stimulus (shown in regular font, next to each stimulus). The Crec-Ccon phase difference for each stimulus was then computed using the time shift and the average period of the corresponding cycle for Crec and Ccon (shown in bold font, next to each stimulus). The Crec-Ccon phase difference ($\Delta\phi$) for this oscillatory episode was taken as the average of the phase differences for individual stimuli. In this case $\Delta\phi$=25.05 deg.

Results

Oscillatory episodes

Synchronous beta band oscillations occurred in both monkeys, over M1 and SMA sites (Figure 7). An average of 1300 (range 780-1870) conditioning and 2940 (range 2580-3360) test stimuli were delivered per experiment. There was an average of 615 bursts per experiment, of which about 85% included 2 or 3 successive stimuli (Figure 8).

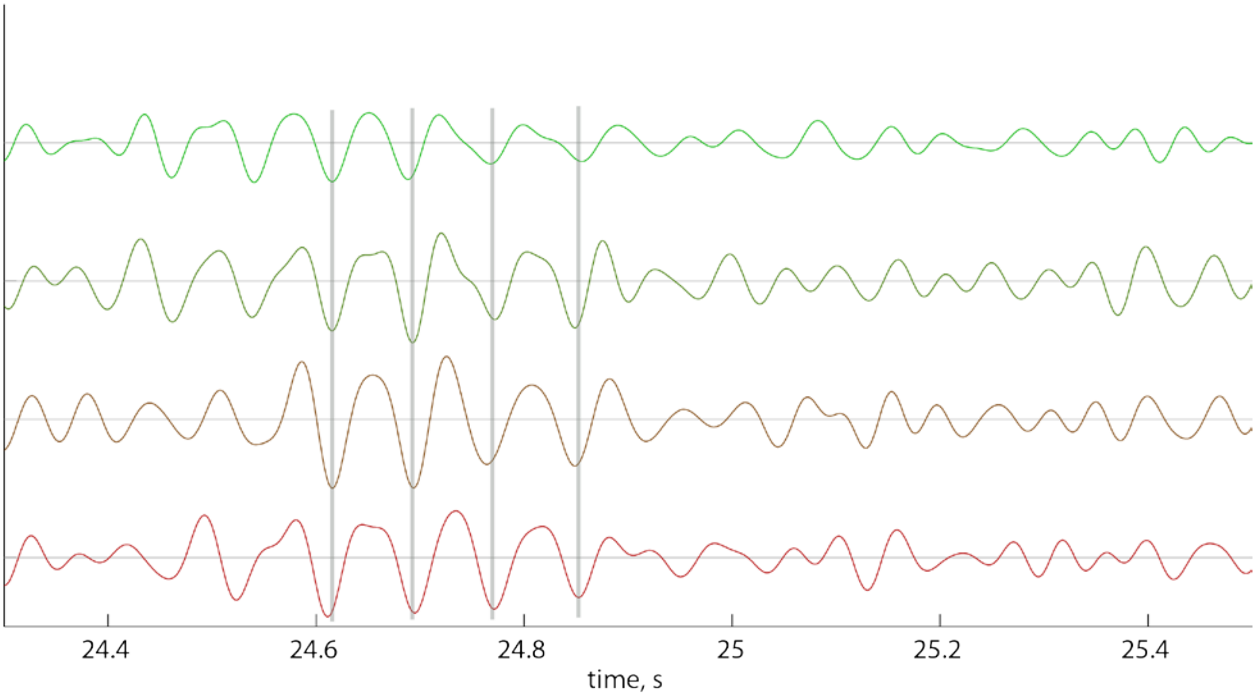

Figure 69. A single episode of synchronous, in-phase beta (~19 Hz) oscillations from 4 neighboring sites in M1 (3 mm inter-electrode distance).

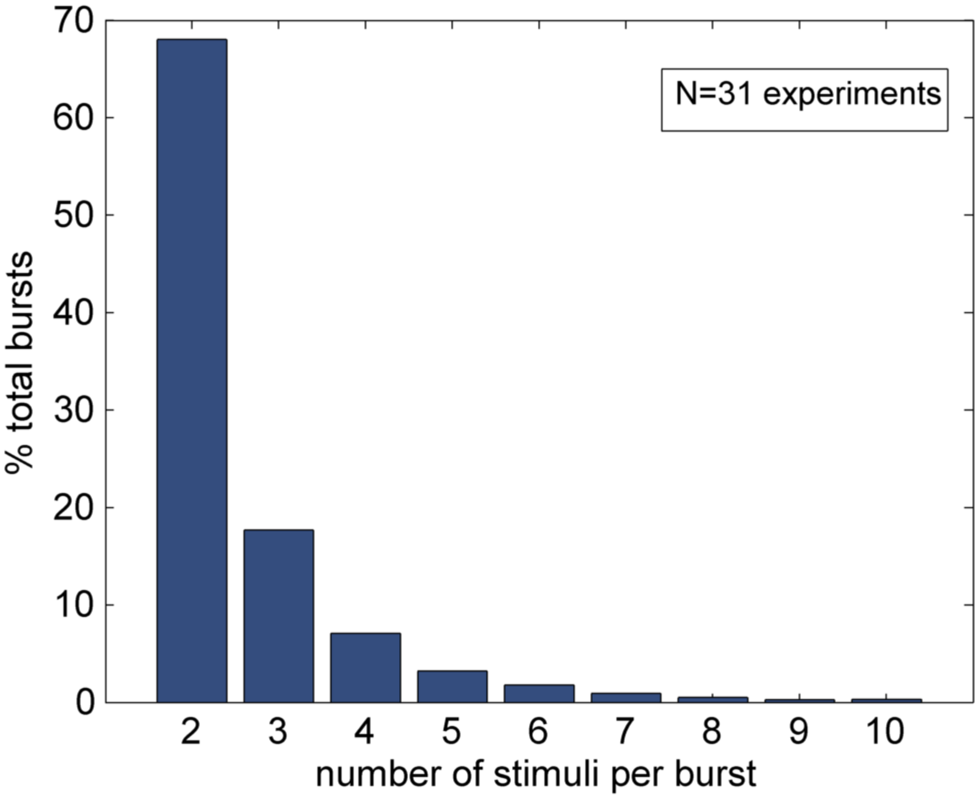

Figure 70. Distribution of bursts with different numbers of conditioning stimuli across 31 experiments with monkey I.

Effects on CEPs

In many cases, when conditioning stimuli were triggered from the depolarizing phase (trough) of beta cycles, the CEP response on the triggering site to the test stimulus following a burst was larger compared to that evoked by the test stimulus before the burst; that was especially the case with bursts of more than two consecutive stimuli; this effect was not seen in control experiments (Figure 9). CEP responses to successive test stimuli after a burst became progressively smaller, typically reaching the amplitude of the CEP response before the conditioning burst within 2 seconds (Figure 10).

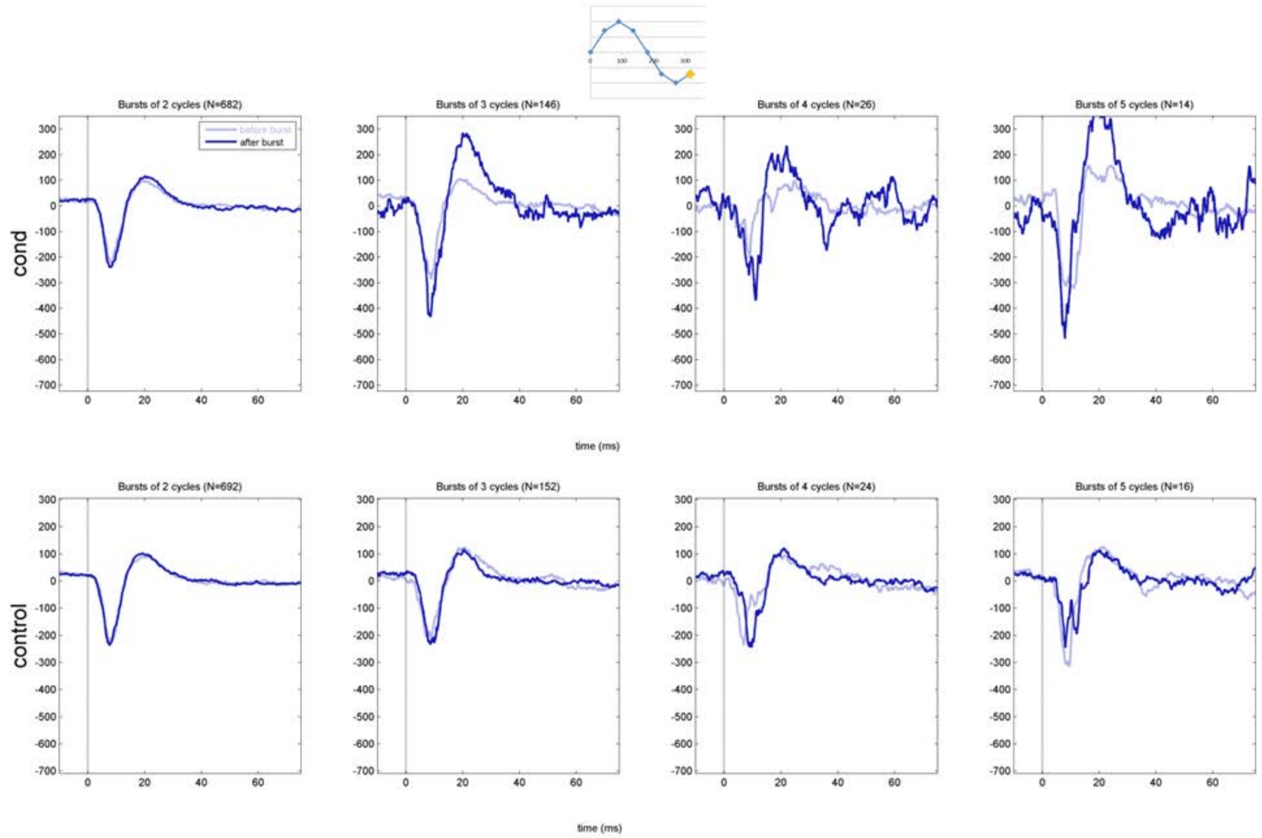

Figure 71. Effect of conditioning with stimuli triggered from the depolarizing phase (trough) of beta cycles on effective connectivity. (Top) Each panel shows the CEP response, on the triggering site, to test stimuli immediately before (pale blue) and after (bright blue) bursts of 2, 3, 4 or 5 successive conditioning stimuli. In this particular example, the triggering site was in M1, the stimulated site was in SMA, and stimuli were delivered at a beta phase of 320 degrees. The amplitude of the CEP response (maximum positive deflection from baseline, between 8 and 30 ms post-stimulus), for bursts of 3 cycles, increased by a "CEP ratio" of ~3.1. (Bottom) Same figures as top row, but compiled from the control experiment. There was no appreciable change in the amplitude of the CEP (CEP ratio 1.01).

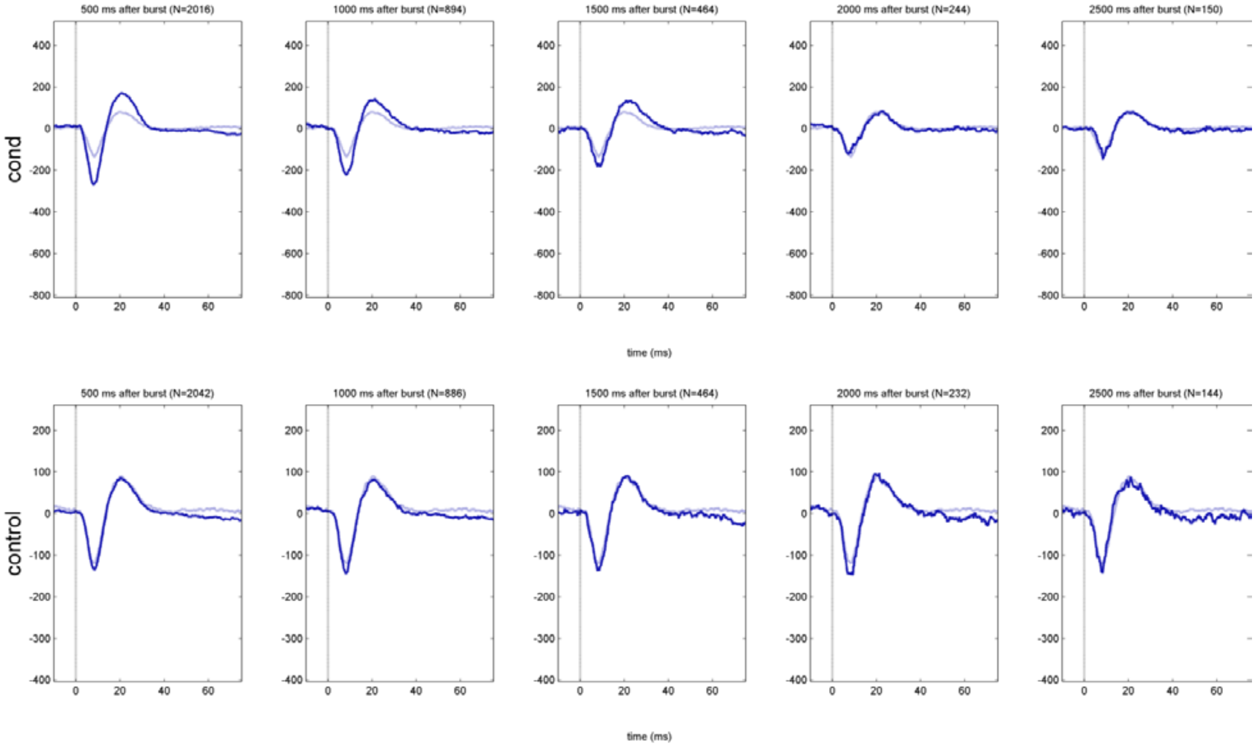

Figure 72. Duration of the potentiating effect on CEP amplitude of conditioning on the depolarizing phase of beta cycles. (Top) Each panel shows the CEP response to the first, second, etc. successive test stimulus after a conditioning burst (bright blue), compared to the CEP response to the last test stimulus before the burst (pale blue). In this particular example, the triggering site was in SMA, the stimulated site was in M1, and stimuli were delivered at a beta phase of 135 degrees. CEP amplitude returned to the level before the conditioning burst after 1.5-2 seconds. (Bottom) Same figures as top row, but compiled from the control experiment.

In some cases, when conditioning stimuli were triggered from the hyperpolarizing phase of the beta cycles, the CEP response was smaller after a conditioning burst. Again, this effect was stronger for bursts of more than two successive stimuli and was absent, or minimal, with control experiments (Figure 11). In these cases, the amplitude of the CEP returned to the level before the conditioning burst within 2 seconds (Figure 12).

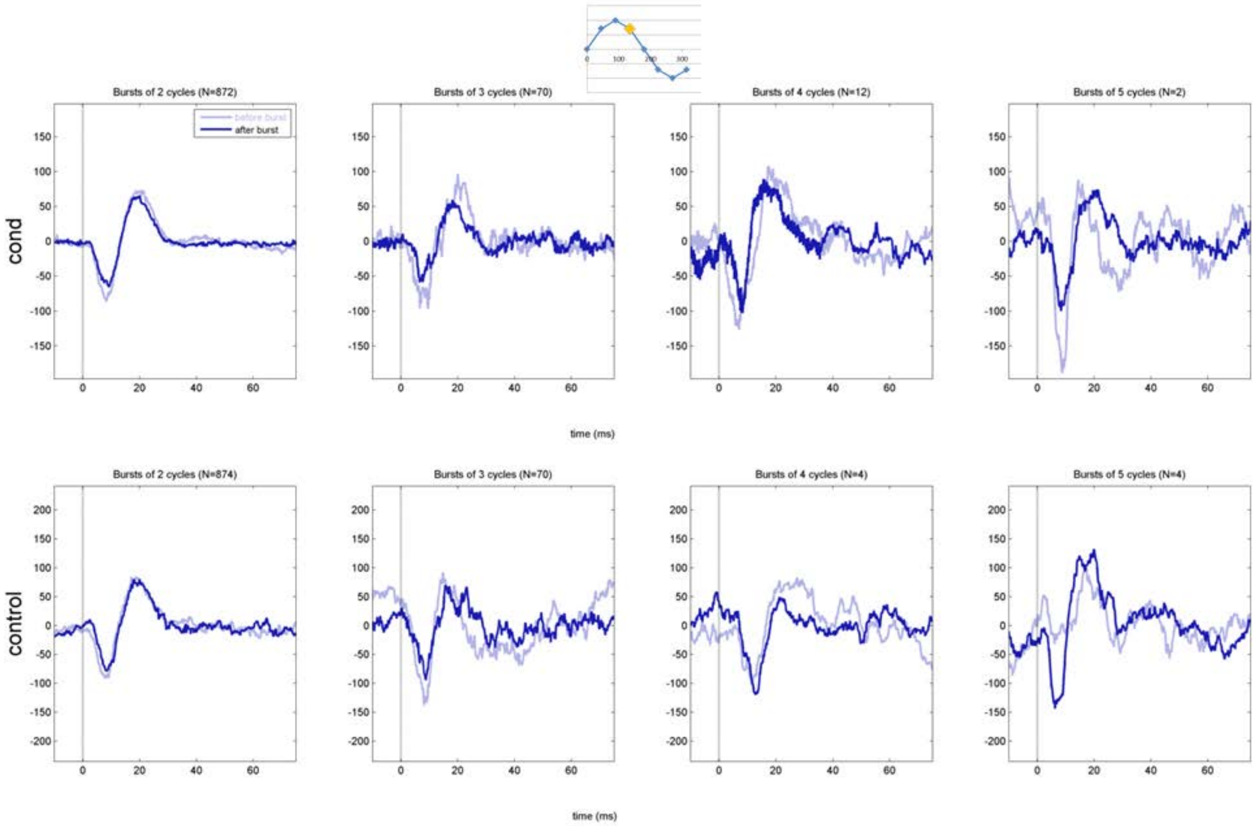

Figure 73. Effect of conditioning with stimuli triggered from the hyperpolarizing phase (peak) of beta cycles on effective connectivity.

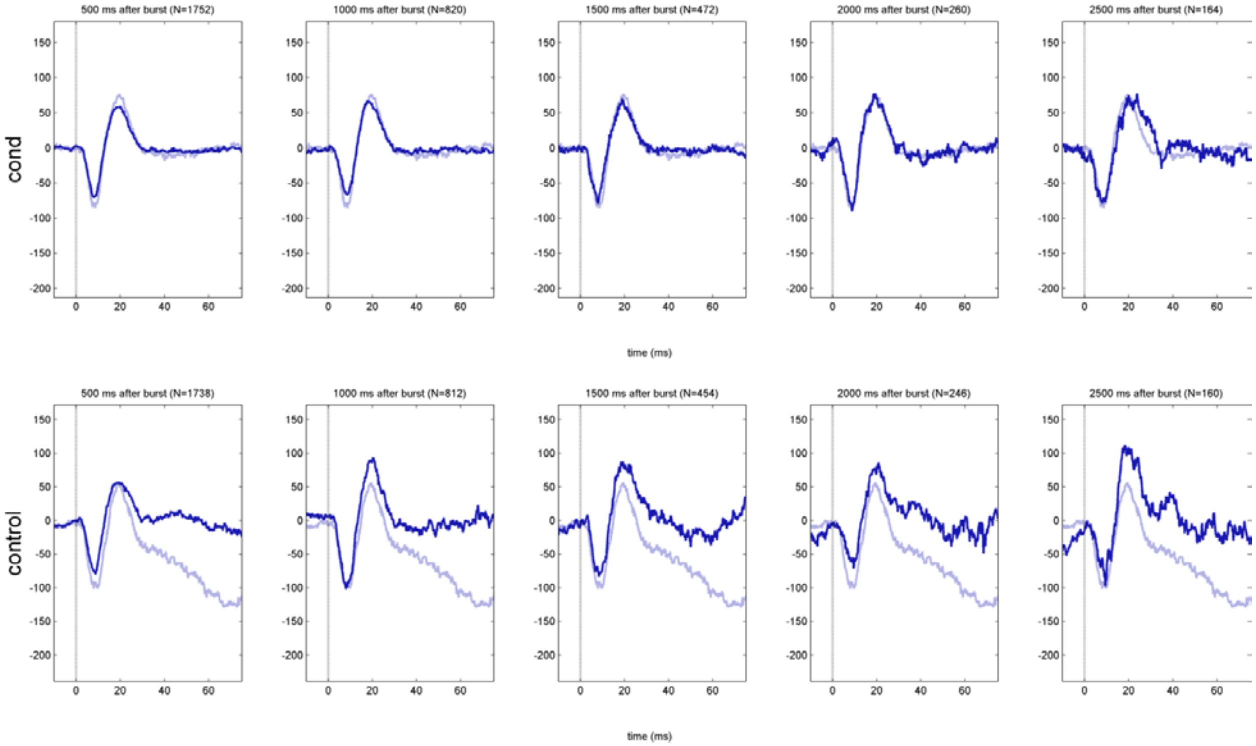

Figure 74. Duration of the inhibiting effect on CEP amplitude of conditioning on the hyperpolarizing phase of beta cycles.

Across 31 experiments, depolarizing-phase stimulation (DPS) was associated with a CEP ratio (ratio of CEP amplitude after 3-cycle bursts to CEP amplitude before those bursts) of more than 1 (CEP potentiation), whereas hyperpolarizing-phase stimulation (HPS) with a CEP ratio below 1 (CEP depression) (Figure 13). There was an inverse relationship between CEP ratio and the distance between C_{TRIG} and C_{STIM}: the shorter the distance, the larger the change in CEP amplitude in conditioning experiments, for both DPS (Figure 14) and HPS (Figure 15). The amplitude of the CEP elicited by consecutive test stimuli after the end of a burst progressively approached that of the pre-burst CEP. This was again true for both DPS (Figure 16) and HPS (Figure 17). The duration of the change in CEP was generally between 1.5-2 seconds.

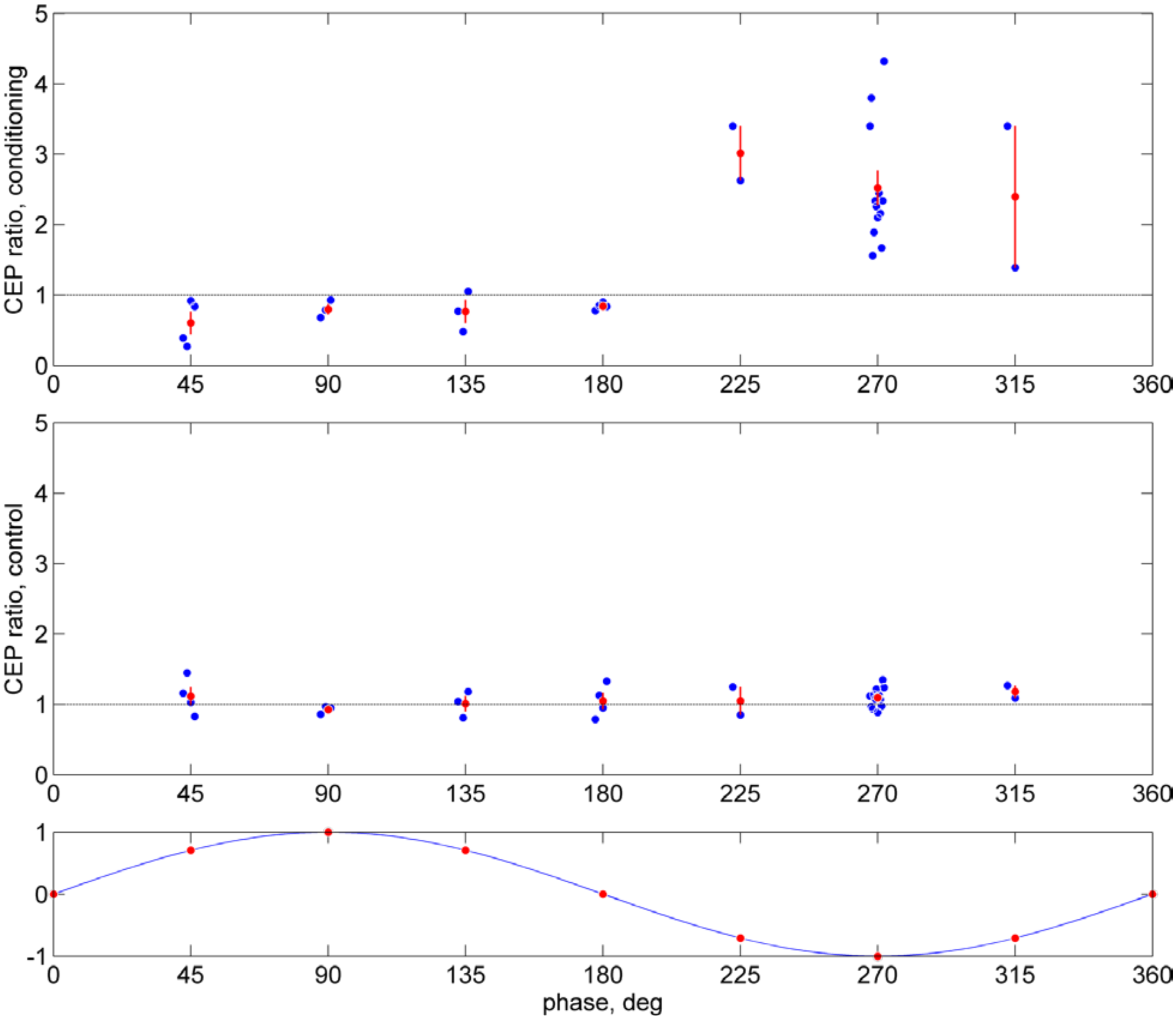

Figure 75. CEP ratio as a function of the phase at which cycle-triggered stimulation was delivered, for all experiments with monkey I. CEP ratio in this case was defined as the ratio of CEP amplitude of the CEP after all 3-cycle bursts in a given experiment, to CEP amplitude before the same bursts. (Top) CEP ratios for the conditioning experiments. Each blue circle corresponds to one experiment. Each red circle corresponds to the average of all experiments for that stimulation phase; red line to the SEM. (Middle) CEP ratios for the control experiments. (Bottom) Stimulation phases used in the conditioning experiments.

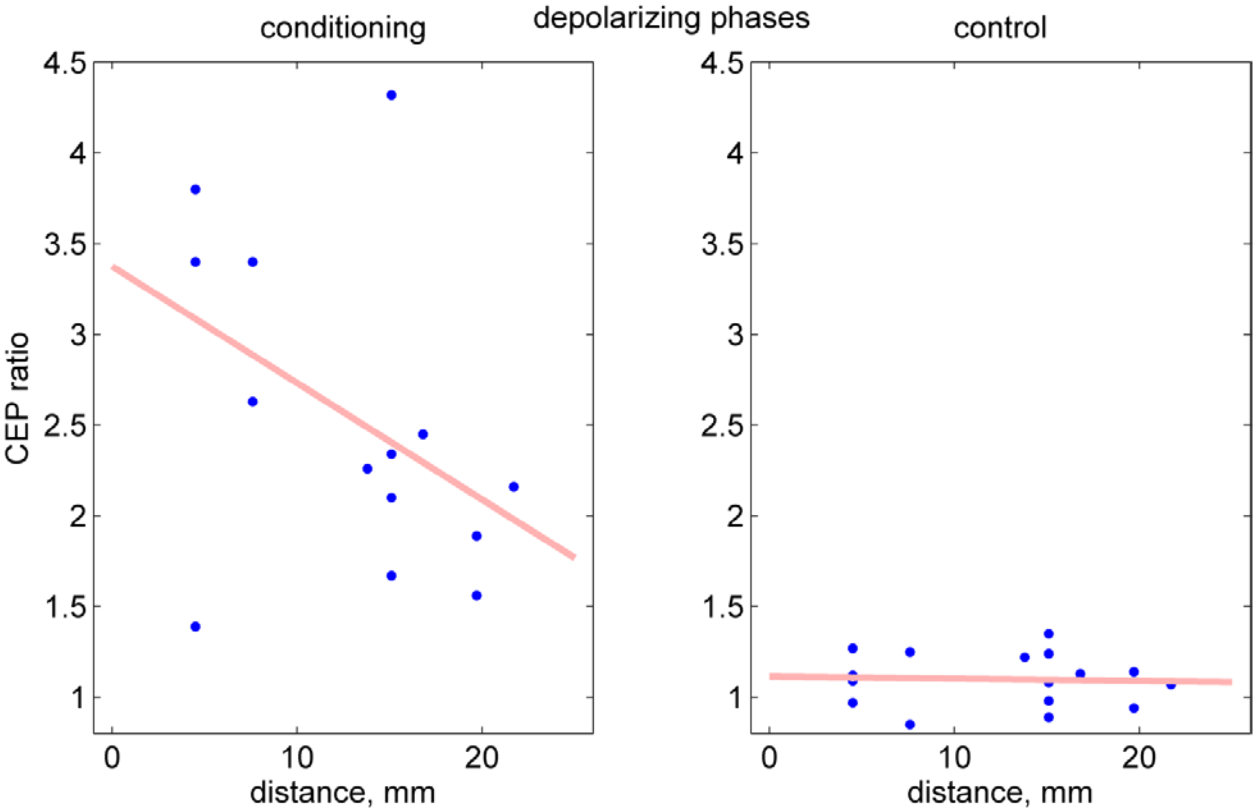

Figure 76. CEP ratio as a function of distance of the triggering site from the stimulated site, for DPS experiments (stimulation phase of 225, 270, and 315 degrees). (Left) Conditioning experiments. (Right) Control experiments.

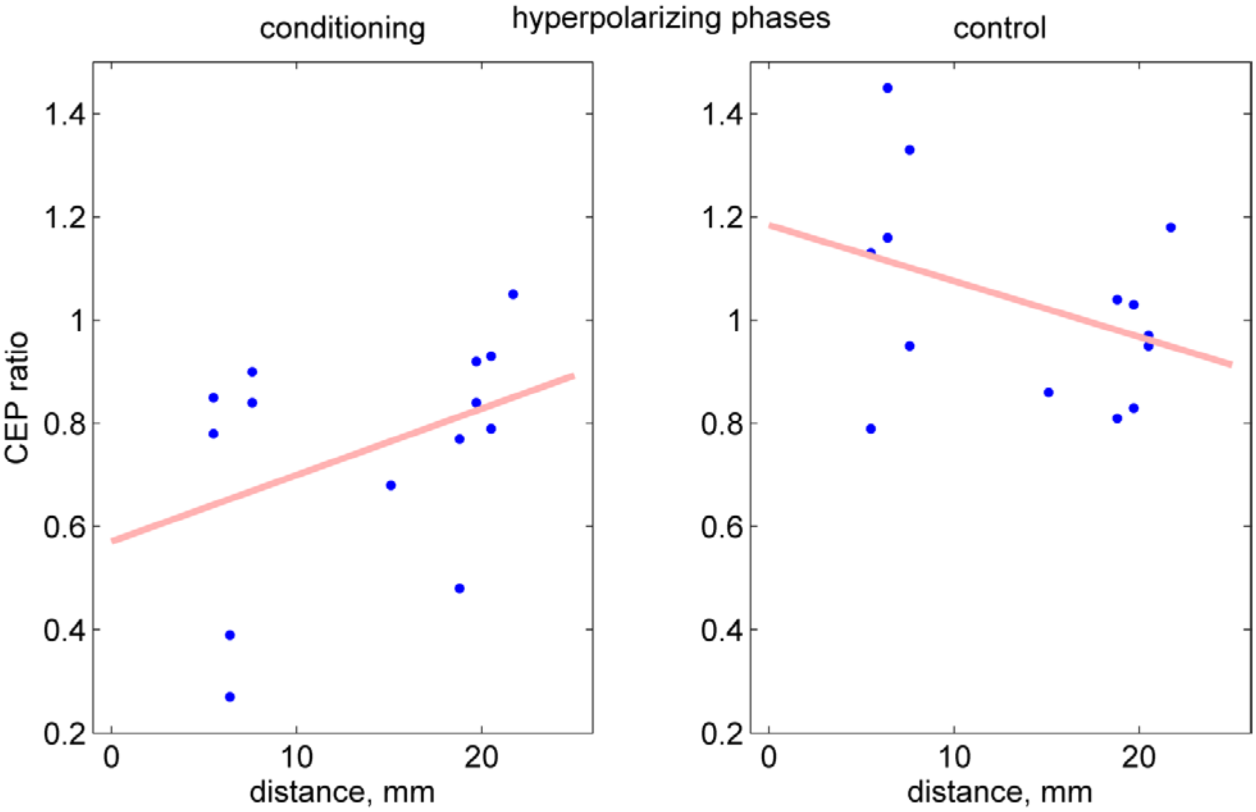

Figure 77. CEP ratio as a function of distance of the triggering site from the stimulated site, for HPS experiments (stimulation phase of 45, 90, 135 and 180 degrees). (Left) Conditioning experiments. (Right) Control experiments.

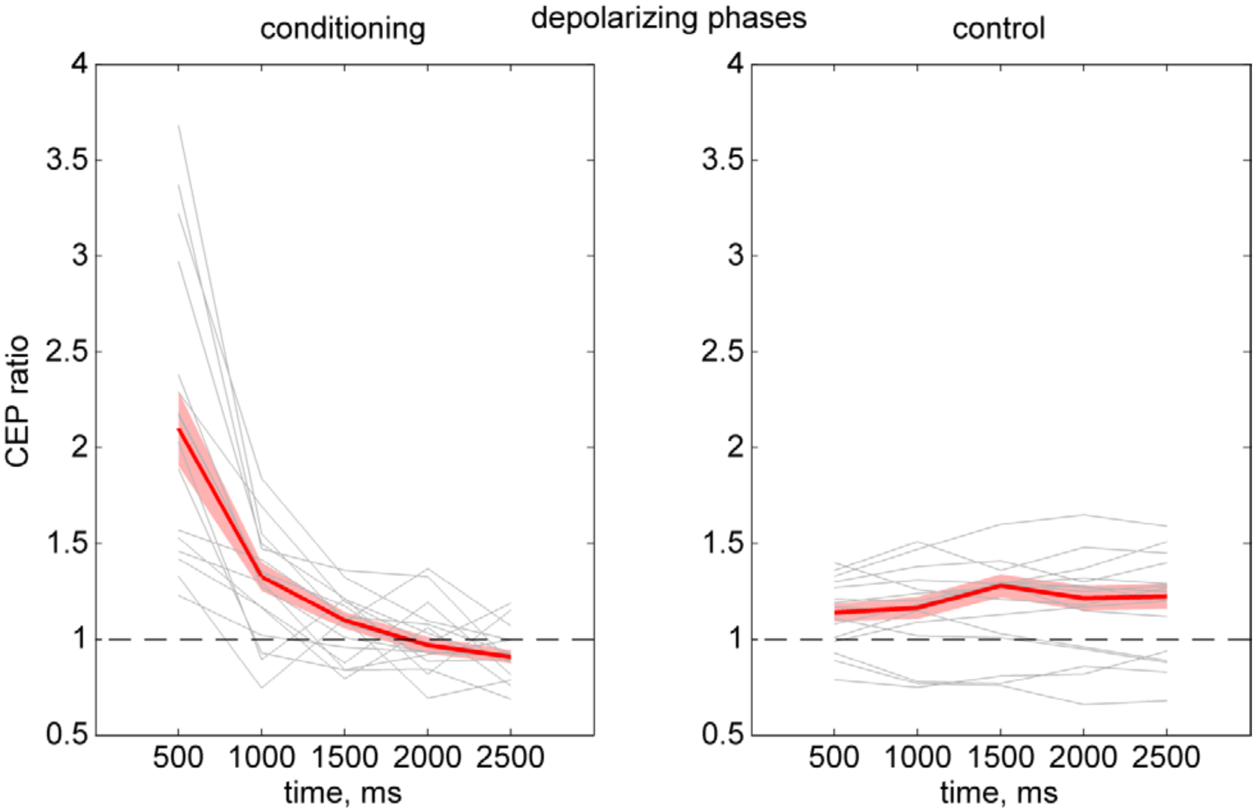

Figure 78. CEP ratio of consecutive test stimuli delivered after a burst, as a function of time from the end of the burst, in DPS experiments. (Left) Conditioning experiments. (Right) Control experiments.

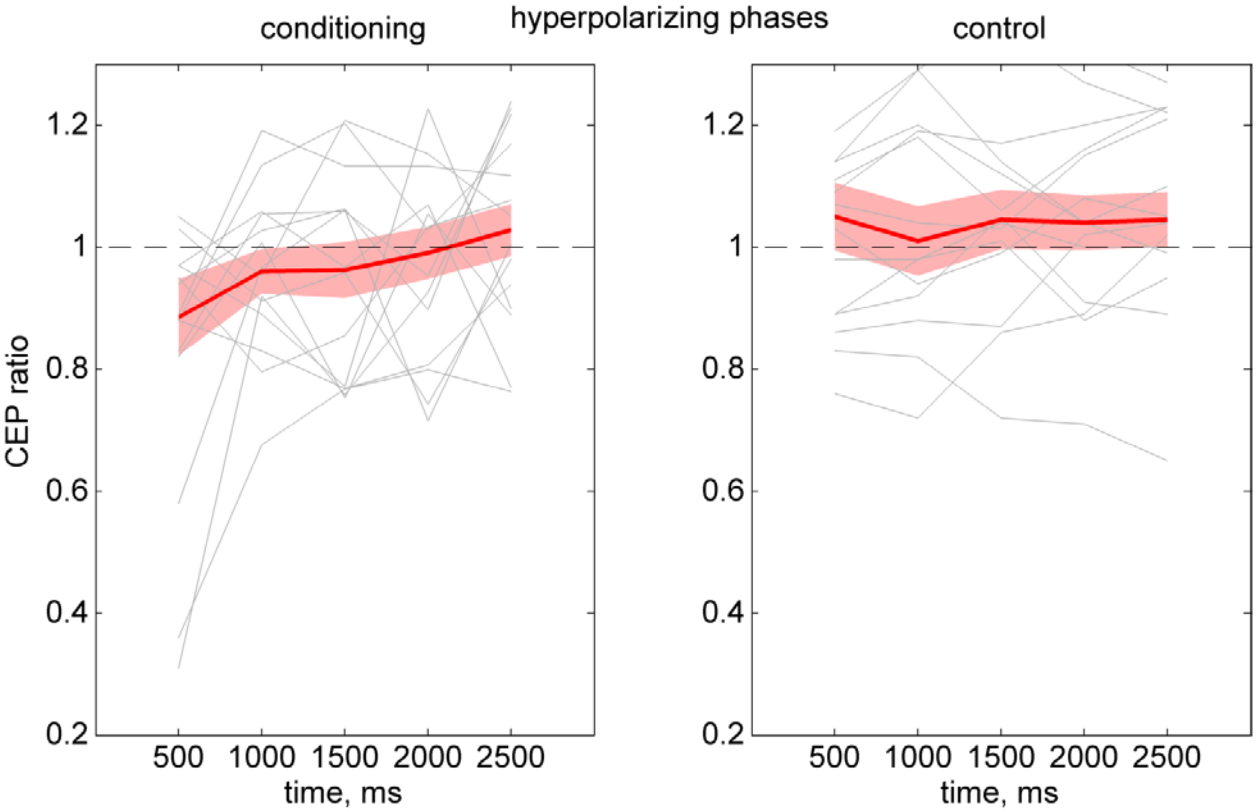

Figure 79. CEP ratio of consecutive test stimuli delivered after a burst, as a function of time from the end of the burst, in HPS experiments. (Left) Conditioning experiments. (Right) Control experiments.

In addition to $C_{TRIG,}$ cycle-triggered stimulation produced CEP amplitude changes on other sites that had stimulus-evoked CEPs. CEP responses to the 500 test stimuli delivered before any conditioning was performed, at C_{TRIG} had mean amplitude 57±35 µV; CEP responses at control sites had a mean amplitude of 62±38 µV (Wilcoxon rank-sum test, p NS) (Figure 18). The lack of a significant difference in CEP amplitude between C_{TRIG} and control sites was expected, as C_{TRIG} sites were chosen randomly among all sites with CEPs. The number of control sites with CEPs in a given experiment was between 1 and 6 (Figure 19), and they were found at different distances from C_{STIM} (Figure 20). Conditioning-induced changes of CEP amplitude at those control sites generally followed that at $C_{TRIG,}$ i.e. increase (CEP ratio>1) for DPS and decrease (CEP ratio<1) for HPS. At control sites, the magnitude of conditioning-induced change of CEP amplitude was typically smaller, i.e. closer to 1, than on C_{TRIG}. In many cases of

DPS, CEP ratio decreased with increasing stimulus phase difference (SPD) between a control site and C_{TRIG} (Figure 21). Accordingly, in HPS experiments, CEP ratio at a control site would increase (towards 1) with increasing SPD (Figure 22).

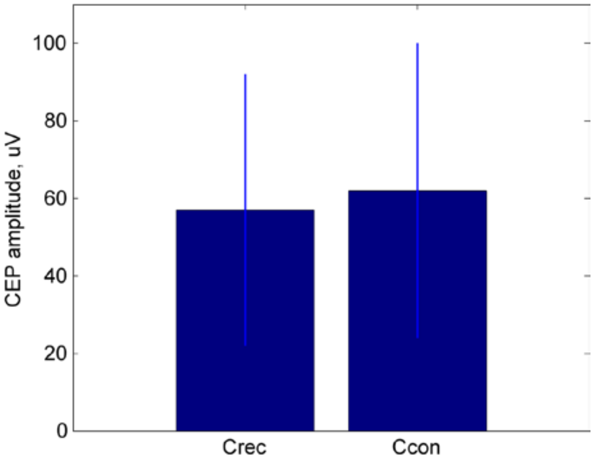

Figure 80. CEP amplitudes at triggering sites (Crec) and control sites (Ccon) (mean±SD values). There was no statistically significant difference (Wilcoxon rank-sum test, p NS).

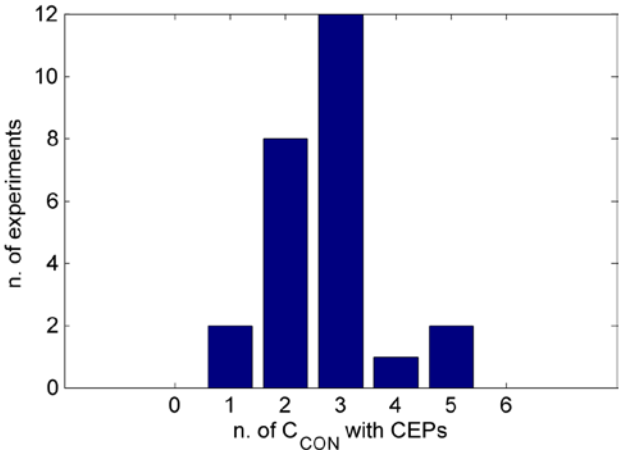

Figure 81. Number of control sites (Ccon) with CEPs elicited by Cstim test stimuli, for 25 experiments in monkey I.

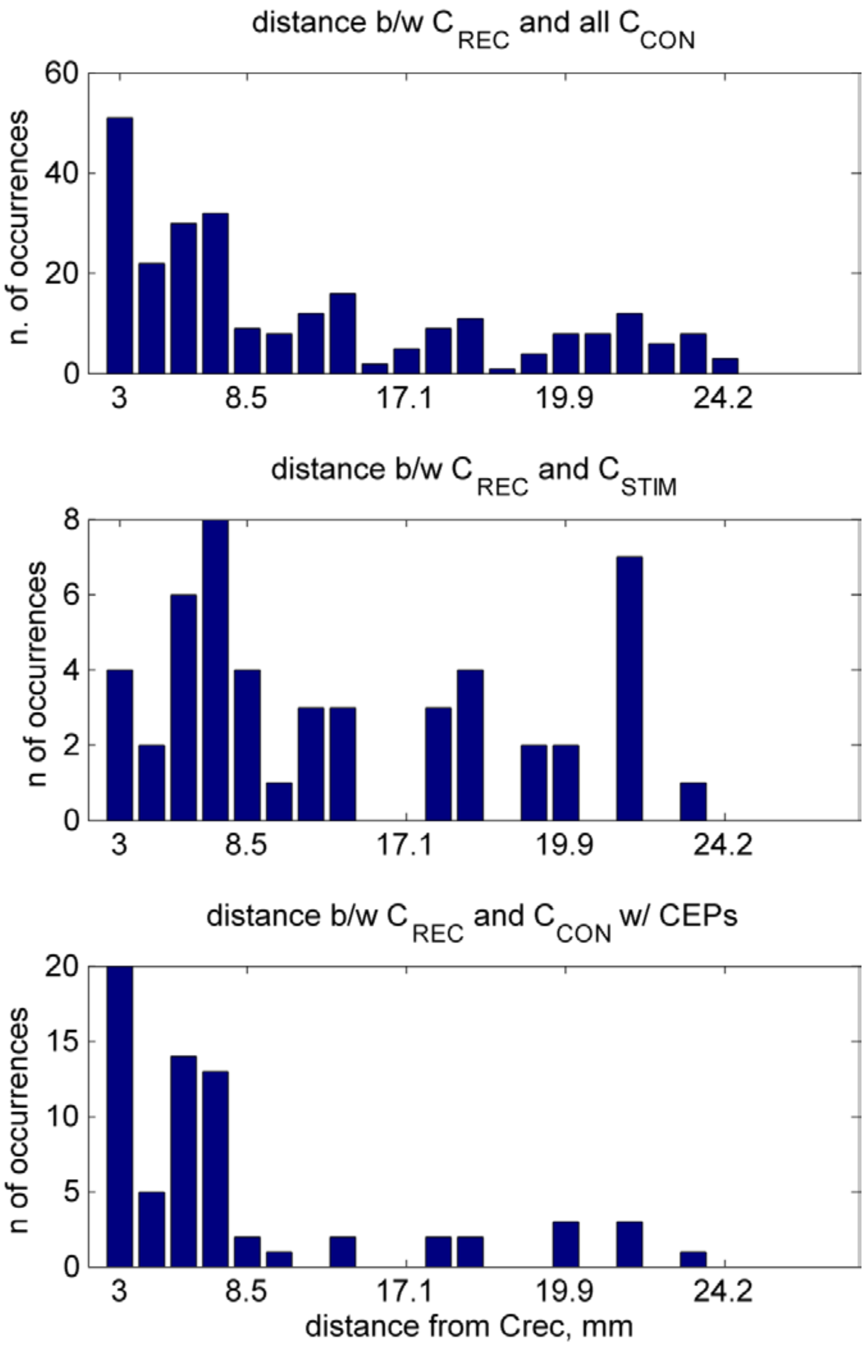

Figure 82. Distribution of distances between the triggering sites (C_{TRIG}) and either stimulated (Cstim) or control sites (Ccon), in 25 conditioning experiments with monkey I. (Top) Distances between Crec and all Ccon sites, including those with and without CEPs elicited by Cstim test stimuli. (Middle) Distances between Crec and Cstim sites. (Bottom) Distances between Crec and Ccon sites with CEPs elicited by Cstim test stimuli. The distributions of Cstim-Crec and Cstim-Ccon distances were not statistically different

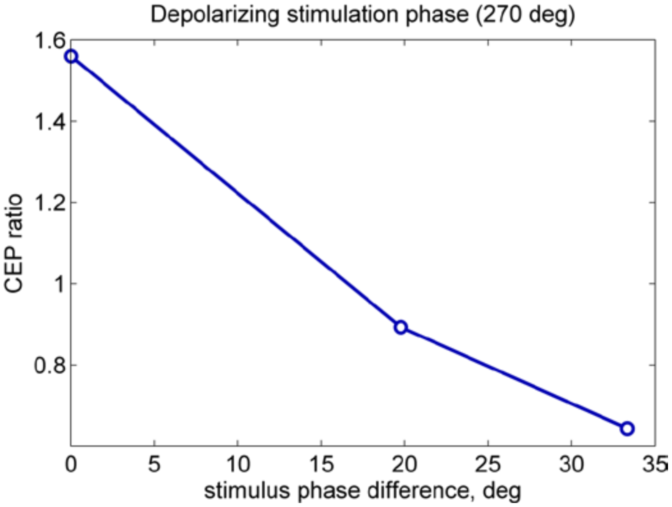

Figure 83. CEP ratios at the triggering site (Crec) and 2 control sites, from a DPS experiment (stimulation phase of 270 degrees). CEP ratios are also shown as a function of the SPD of each site with respect to Crec (SPD of 0 degrees corresponds to Crec). In this experiment there were 2 control sites. A CEP ratio closer to 1 implies a smaller conditioning-induced change in CEP amplitude.

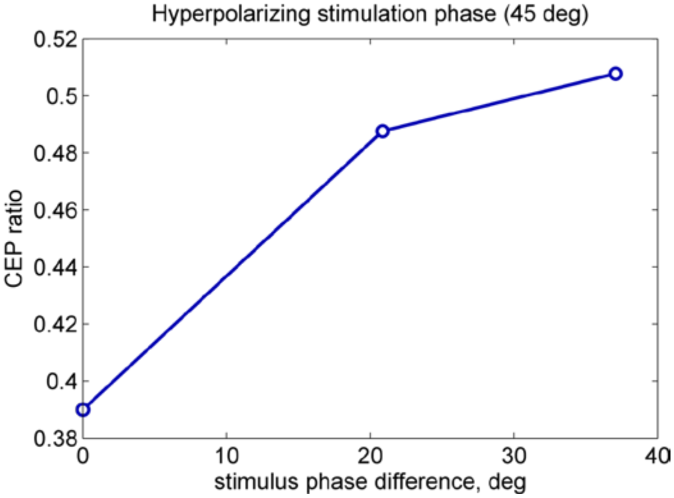

Figure 84. CEP ratios on the triggering site (Crec) and 2 control sites, from an HPS experiment (stimulation phase of 45 degrees).

Overall, the shift in CEP ratio on a control site away from the CEP ratio on C_{TRIG} was positively correlated with the SPD of that control site from C_{TRIG} (Figure 23). In other words, control sites with similar oscillatory phases at the time of stimulation to the phase of $C_{TRIG,}$ had conditioning-induced CEP amplitude changes similar to that of C_{REC}. In contrast, there was no correlation to the distance between the control site and C_{TRIG}.

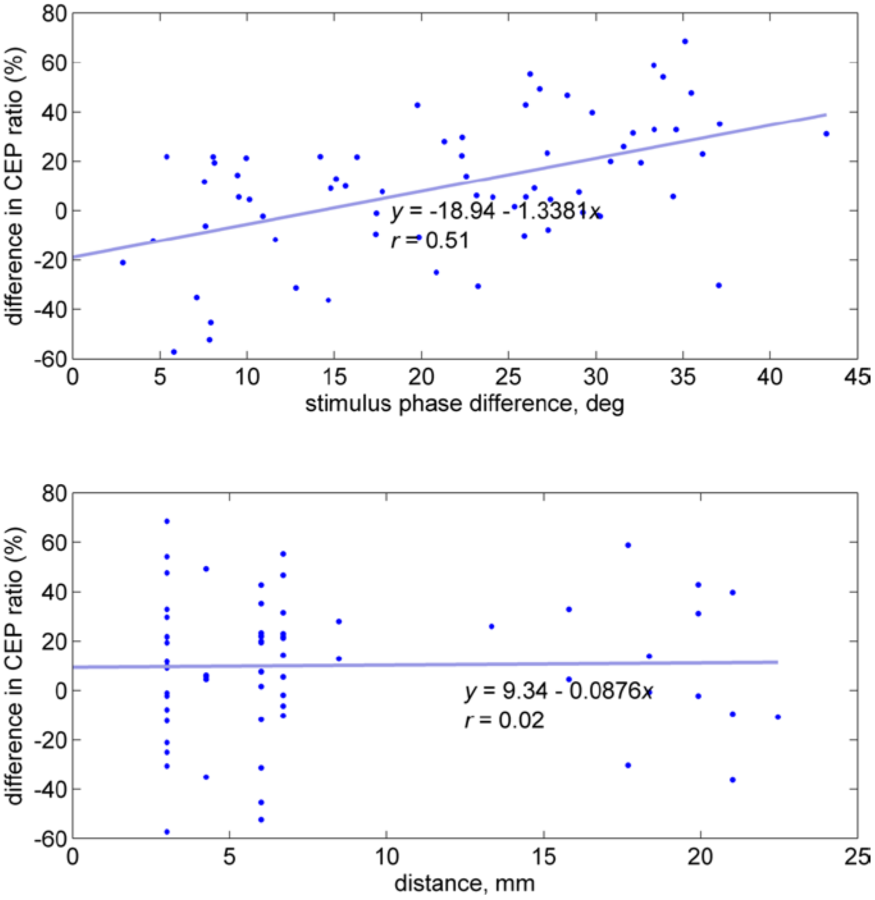

Figure 85. The effect of conditioning on control sites depends on their stimulus phase difference (SPD) in respect to C_{TRIG}. (Top) Correlation between the difference in CEP ratio on control sites in respect to that on Crec (from the same experiment), and their SPD from Crec. The correlation was statistically significant ($p<0.001$). (Bottom) Correlation between the difference in CEP ratio on control sites in respect to that on $C_{TRIG,}$ and their distance from Crec. The correlation was not significant ($p=0.36$).

Effects on coherence

Coherence spectra usually had peaks over alpha (2-4 Hz) and beta (15-25 Hz) ranges; coherence was higher, across all frequencies, for pairs of nearby sites than for pairs of remote sites (Figure 24).

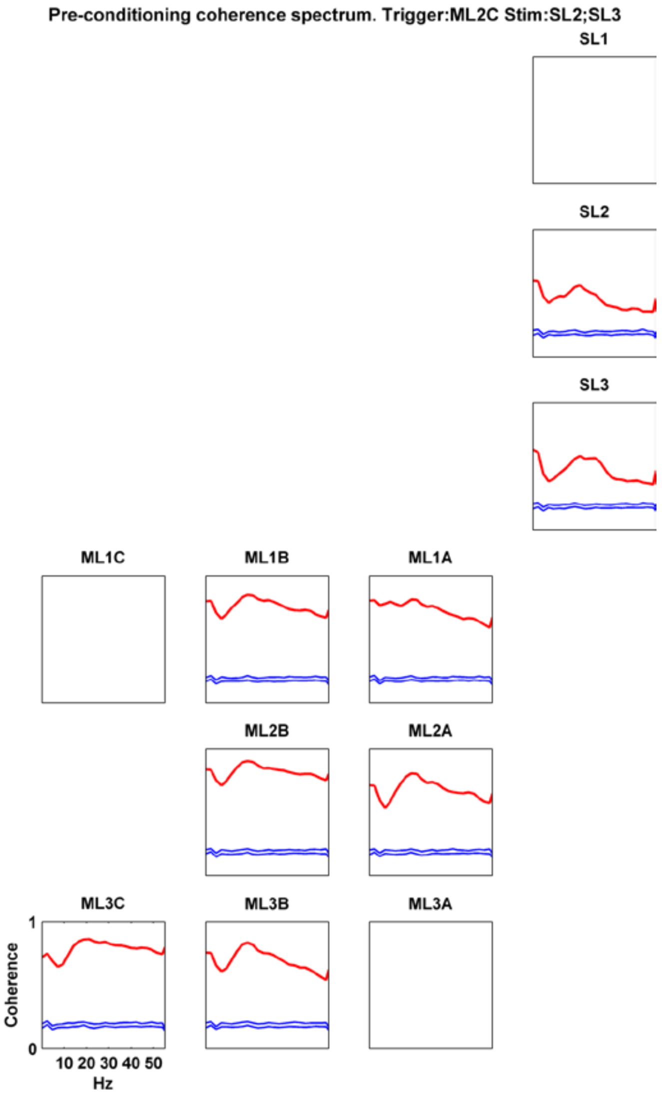

Figure 86. Coherence spectra of pairs of signals from the triggering site and other electrodes before a conditioning experiment. The panel with no plot in it corresponds to the triggering site; empty panels correspond to noisy signals that were not analyzed. The red curve represents the actual coherence spectrum, between 2 and 55 Hz; the 2 blue curves represent the 95% confidence intervals of the "random" coherence spectrum.

In DPS conditioning experiments, significant coherence changes were observed in pairs involving the triggering and the stimulated sites (T-S pairs), as well as in pairs involving the triggering and non-stimulated sites (T-NS pairs) (Figure 25).

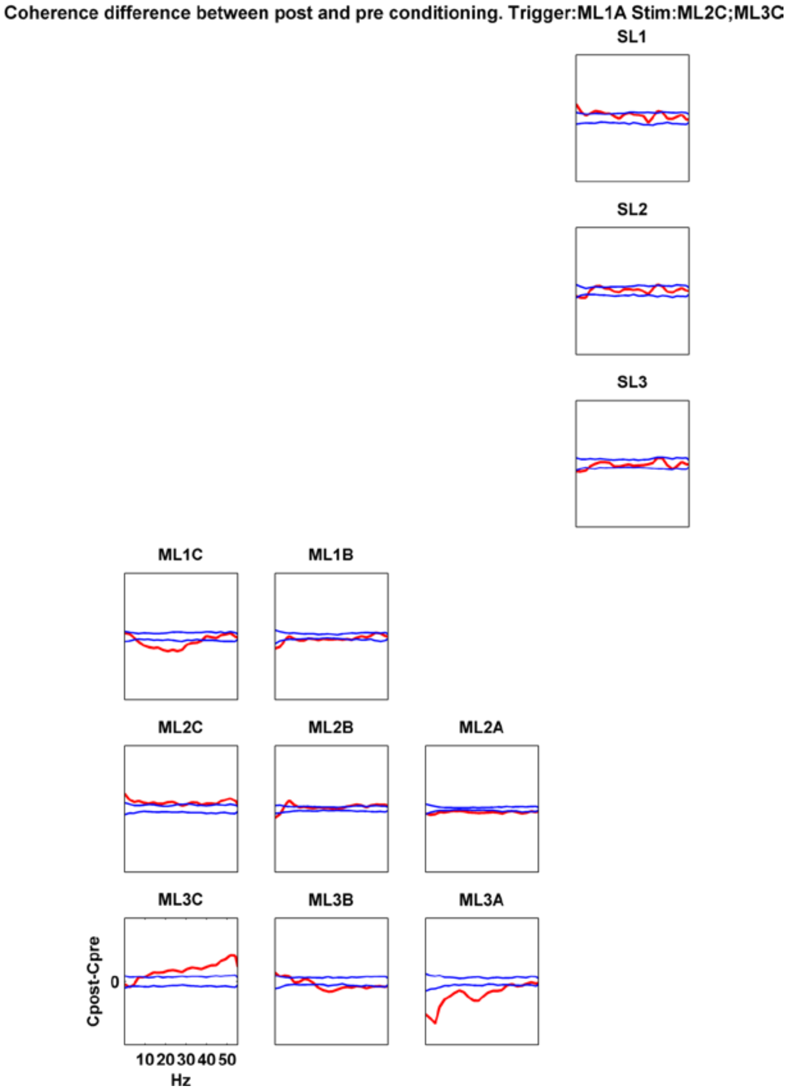

Figure 87. Coherence difference spectra of pairs of signals from the triggering electrode and other electrodes. In this DPS experiment stimulation the triggering site was ML1A (missing panel), and stimulation was delivered between sites ML2C and ML3C. The red curve represents the actual coherence spectrum, between 2 and 55 Hz; the 2 blue curves represent the 95% confidence intervals of the "random" coherence difference spectrum.

In the same example, scalar coherence in the delta (2-4 Hz) (Figure 26), theta (4-8 Hz) (Figure 27) and alpha (8-12 Hz) (Figure 28) ranges increased with conditioning, in T-S as well as in T-NS pairs. In contrast, scalar coherence in the beta range (15-25 Hz) increased significantly in T-S, but not in T-NS pairs (Figure 29).

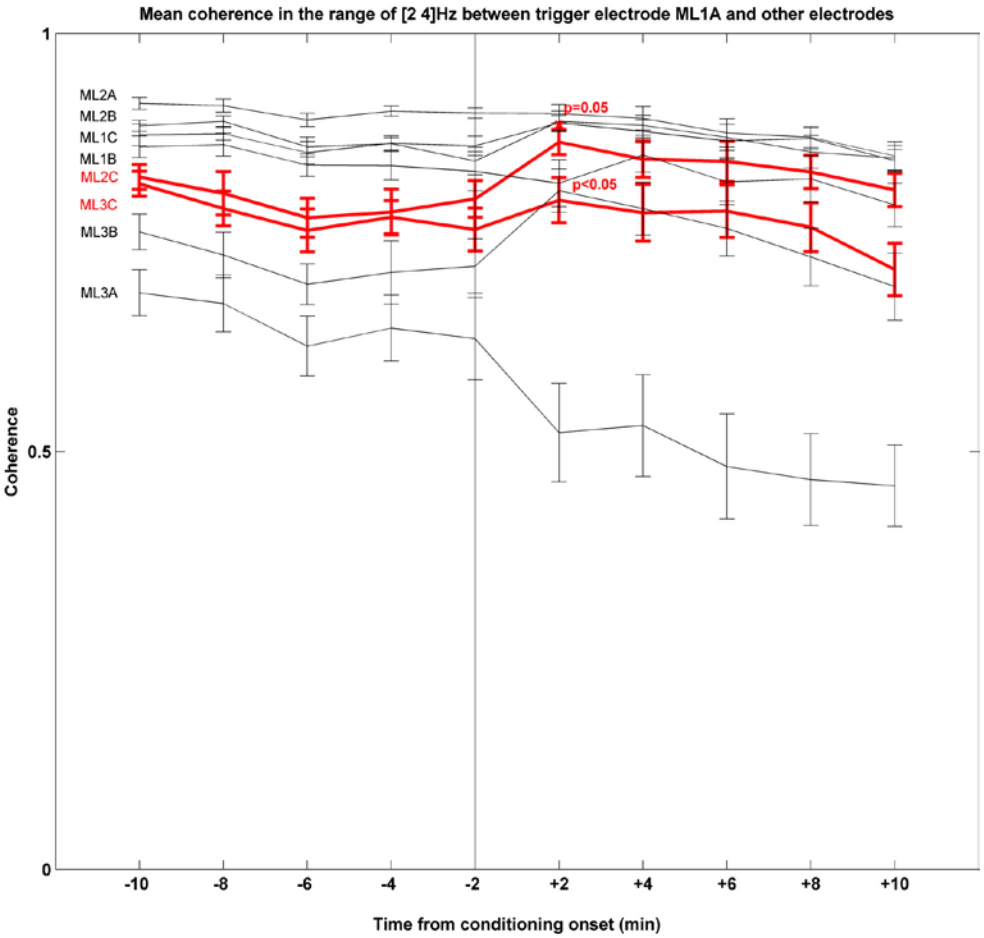

Figure 88. Changes in delta range (2-4 Hz) coherence between signals from the triggering site and other sites, as a function of time before and after conditioning in a DPS experiment. The 2 red curves correspond to coherence between the triggering and the 2 stimulated electrodes; the black curves to coherence between the triggering and the non-stimulated electrodes. The two p values correspond to the statistical significance of the comparison between pooled (-10 to -2 min) pre-conditioning and immediately post-conditioning (at +2 min) coherence values, for the 2 triggering-stimulated pairs.

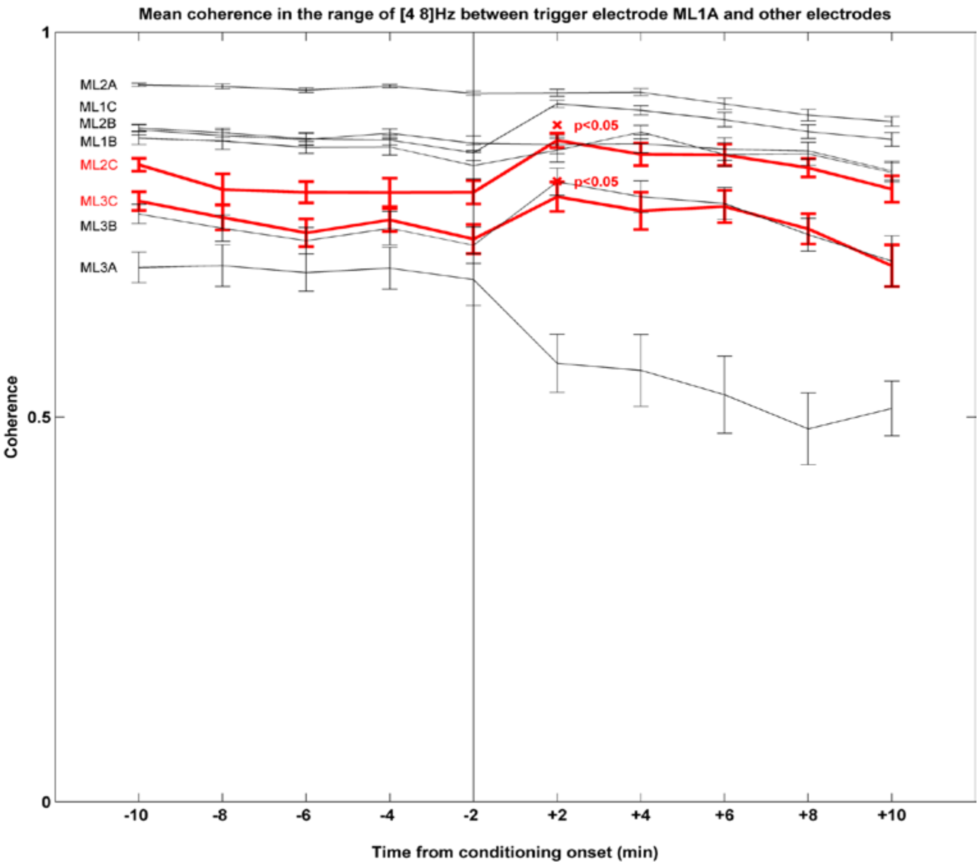

Figure 89. Changes in theta range (4-8 Hz) coherence between signals from the triggering site and other sites, as a function of time before and after conditioning in a DPS experiment.

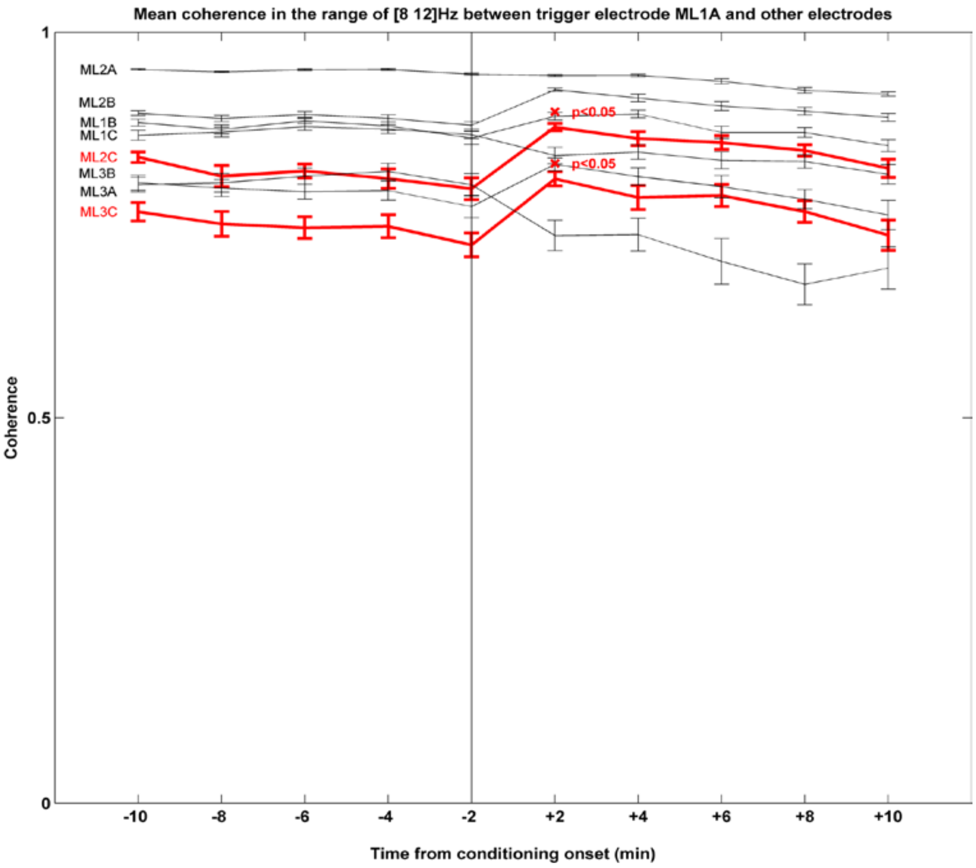

Figure 90. Changes in alpha range (8-12 Hz) coherence between signals from the triggering site and other sites, as a function of time before and after conditioning in a DPS experiment.

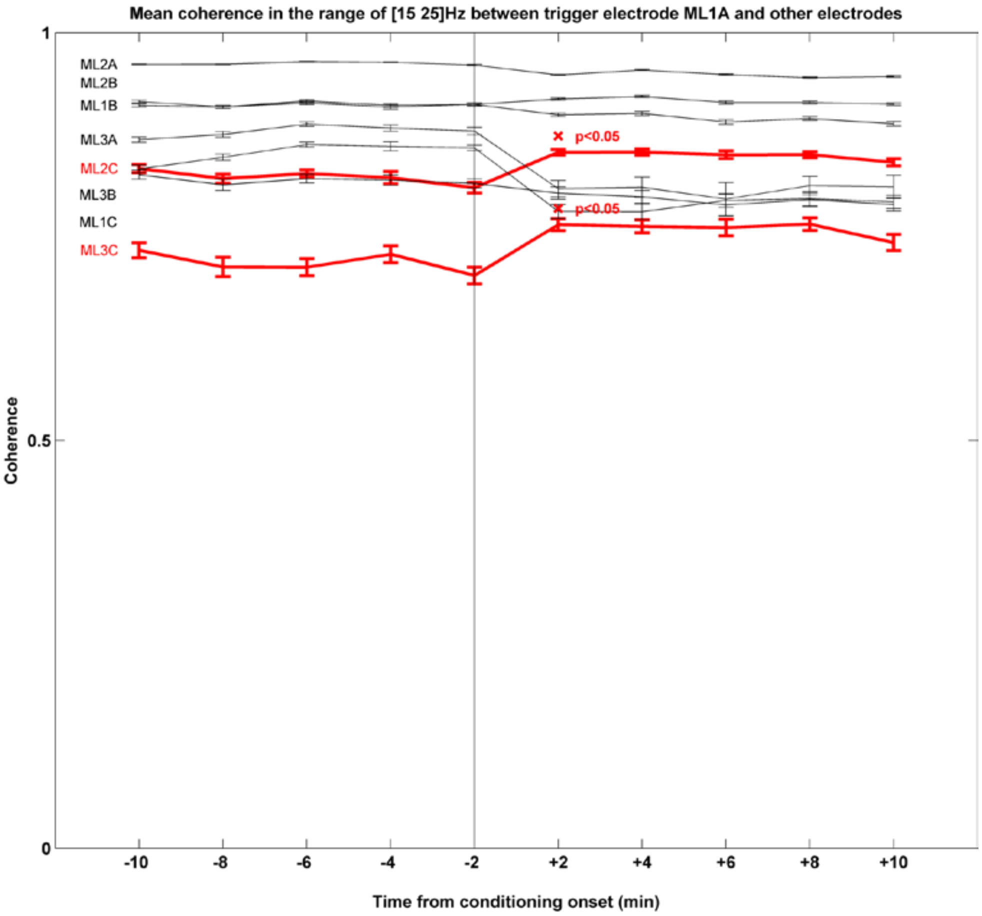

Figure 91. Changes in beta range (15-25 Hz) coherence between signals from the triggering site and other sites, as a function of time before and after conditioning in a DPS experiment.

In HPS experiments, coherence in the delta, theta and alpha ranges increased, in both T-S and T-NS pairs, as was the case with DPS experiments. In contrast, scalar coherence in the beta range decreased with stimulation, in both T-S and T-NS pairs (Figure 30).

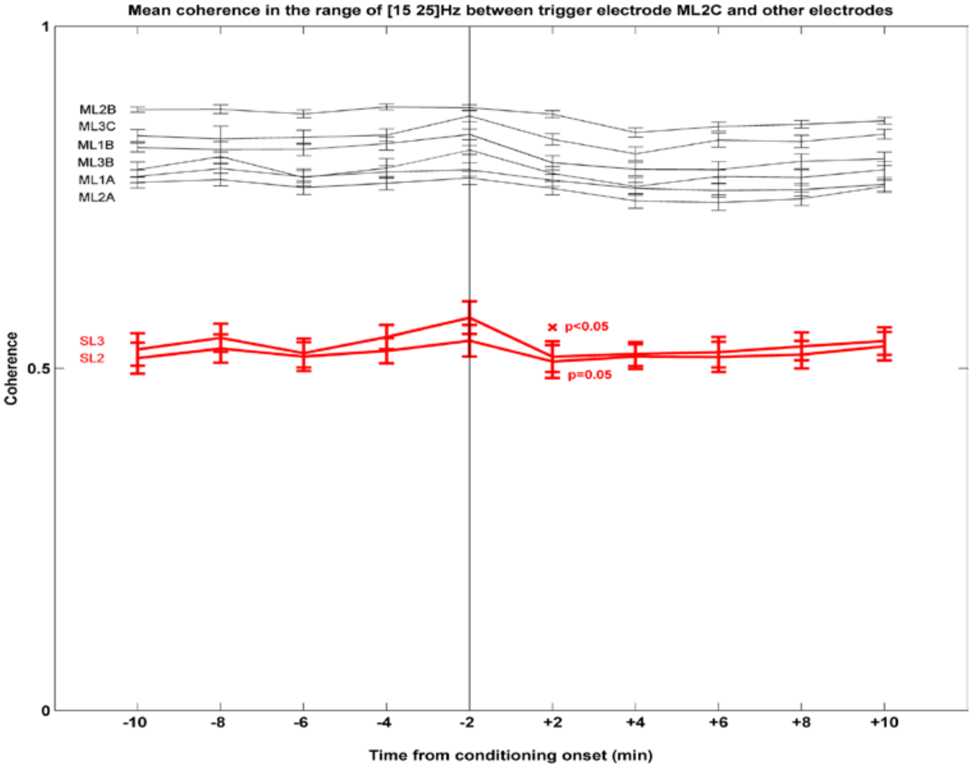

Figure 92. Changes in beta range (15-25 Hz) coherence between signals from the triggering site and other sites, as a function of time before and after conditioning in an HPS experiment.

Overall, in DPS experiments, scalar coherence for delta, theta and alpha ranges increased for both T-S and T-NS pairs; beta coherence on the other hand increased for T-S pairs (Figure 31) but decreased for T-NS pairs (Figure 32). In HPS experiments, coherence in delta, theta and alpha ranges increased, for both T-S and T-NS pairs, whereas beta coherence decreased (Figure 33)(Figure 34).

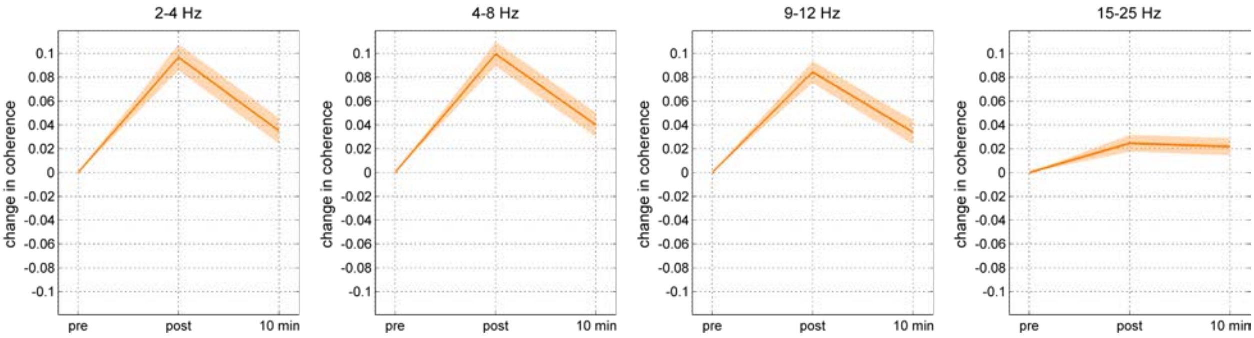

Figure 93. Change in scalar coherence for pairs between triggering and stimulated sites as a function of time around conditioning, averaged over all DPS experiments. Each panel corresponds to a different frequency range.

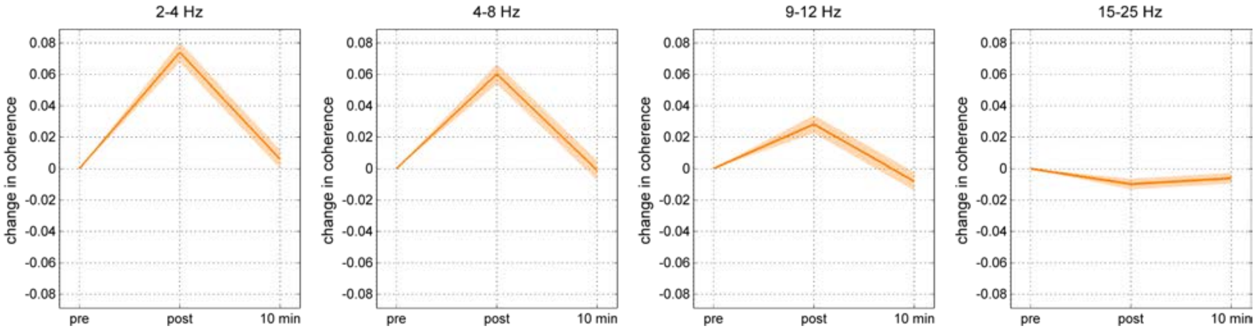

Figure 94. Change in scalar coherence for pairs between triggering and non-stimulated sites as a function of time around conditioning, averaged over all DPS experiments.

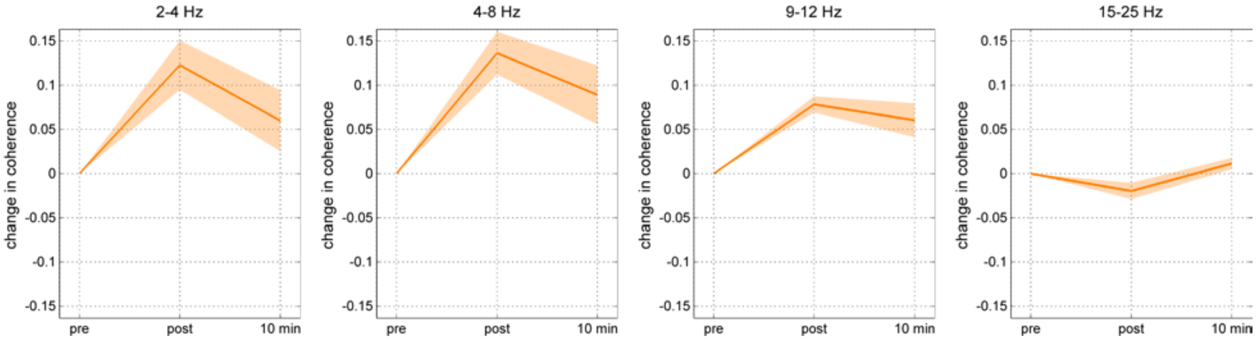

Figure 95. Change in scalar coherence for pairs between triggering and stimulated sites as a function of time around conditioning, averaged over all HPS experiments.

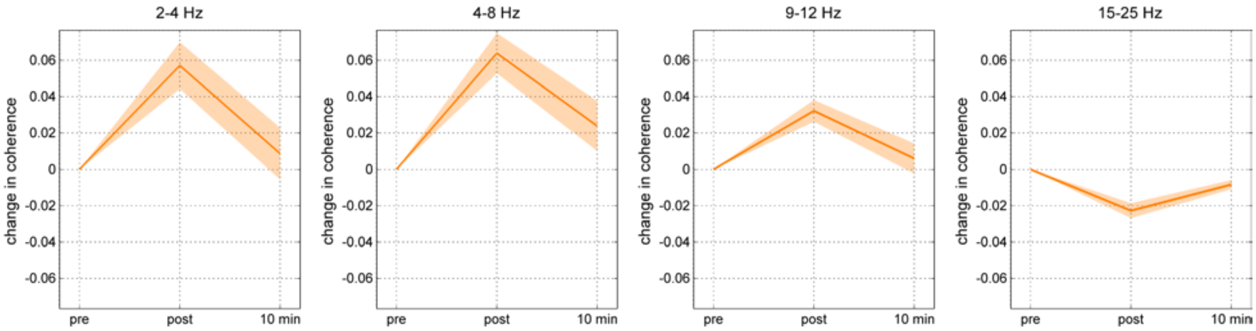

Figure 96. Change in scalar coherence for pairs between triggering and non-stimulated sites as a function of time around conditioning, averaged over all HPS experiments.

Discussion

In this study, we demonstrated that closed-loop stimulation of a cortical site triggered from cycles of beta (15-25 Hz) oscillatory episodes of ECoG recorded at a separate site leads to a change in the effective connectivity between these two sites that outlasts the oscillatory episodes. When stimulation was triggered from the negative (depolarizing) phase of beta cycles, effective connectivity was potentiated, and when triggered from the positive (hyperpolarizing) phase, effective connectivity was suppressed. The potentiation or suppression of connectivity required at least 2-3 conditioning stimuli for its induction and lasted for 1.5-2 sec after the end of each oscillatory episode. Such effects did not occur when the same stimuli were delivered at a later time, with no temporal relationship to ongoing oscillatory activity. In addition to the short-term changes in CEP-resolved connectivity, we found longer-term effects on correlations of spontaneous cortical activity, in the form of coherent beta oscillations between the site whose oscillatory activity triggered the stimulation and the site that received the stimulation; depolarizing-phase stimulation (DPS) caused an increase in beta coherence, whereas hyperpolarizing-phase stimulation (HPS) cased a decrease in beta coherence. This effect was present 5-10 minutes after the end of a 30-min-long conditioning session.

Measures of cortical connectivity

We used two methods for assessing stimulation-induced changes in cortical connectivity.

The first, the measurement of CEPs uses the cortical response to cortical stimulation and rests on the assumption that the presence of CEPs between two cortical sites reflects a direct anatomical connection between them. Stimulation of a cortical site typically activates large numbers of cells and fibers. If some of those fibers form connections with a second cortical site, an extracellular field will be evoked that represents the sum of the postsynaptic potentials and the, synaptically-mediated, activation of cells in the second cortical site.

Single pulses of surface electrical stimulation of small intensity excite, directly and indirectly, neurons and fibers in relatively limited radial distances (<3 mm) from the stimulating electrode (Adrian 1936; Asanuma and Rosen 1973; Bagshaw and Evans 1976; Gustafsson and Jankowska 1976; Stoney et al. 1968). Recruitment of these neurons happens relatively fast: less than 0.5 ms for direct excitation, 0.7-1.5 ms for transynaptic excitation (Gustafsson and Jankowska 1976; Rosenthal et al. 1967). These observations suggest that single cortical surface stimuli generate a relatively synchronous volley of “presynaptic” action potentials. These action potentials then travel on the fibers extending between the stimulated site and the recording sites, both near and distant (Adrian 1936). The result of the near-simultaneous arrival of those action potentials to a recording site generates the CEP.

Most CEPs in our study had a biphasic pattern (Figure 5): a brief (6-10 ms duration) negative phase that peaked at 5-8 ms post-stimulus, followed by a positive phase, with a greater, and more variable, duration (10-25 ms). Even though the exact generator mechanism of CEPs is not clear, it is likely that the first deflection in CEPs reflects mono- or oligosynaptic responses, in the form of postsynaptic potentials, produced by the near-synchronous arrival of the volley of action potentials from the stimulated site, via cortico-cortical projection fibers (Li and Chou 1962). There have been different hypotheses for the generator mechanism of the second phase, including delayed local activity at the recording site (El'kina and Trush 1982; Rosenthal et al. 1967) or antidromic activation of presynaptic terminals that originate from the stimulated or other sites (Curtis 1940; Matsumoto et al. 2007). The amplitude of the first phase would be the most direct measure of stimulus-evoked postsynaptic potential response. In practice, we found that the amplitudes of the two phases were highly correlated (CC=0.8, $p<0.001$). The magnitude of the conditioning effect on the two phases was also very similar (data not shown). We chose to first focus on the second phase because in about 9 experiments (of the 31 reported here) the initial segment of the first phase was partially obscured by the stimulus artifact. A more detailed analysis of the first phase of the CEP responses will have to be performed.

Volume conduction, from nearby activated cortical areas, can also be the source of much of the evoked response (Skrandies et al. 1978). In our study, this was minimized by implementing a Laplacian differential derivation of the field potential signal (Paralikar et al. 2009). Another potential source of a CEP is stimulus activation of a thalamocortical loop. In this case, the CEP arises as a result of activation of the recording site not directly from the stimulated site, but via a thalamic site that is connected to both. In a number of studies, using somatosensory evoked potentials, (Allison et al. 1991; Arezzo et al. 1979; Arezzo et al. 1981; Hayashi et al. 1995; Lemon 1979; Lemon and van der Burg 1979) it was determined that the typical thalamocortical latency in the nonhuman primate is between 3 and 10 ms. In our study, given that the earliest traces of CEP activity occurred at latencies 3-6 ms, CEPs cannot be attributed solely to corticothalamic loops, in which case minimum CEP latencies would have been at least 6 ms.

The second cortical connectivity measure we used is phase coherence. The association between field phase consistency and correlated neuronal firing, which implies a mediating connectivity, is based on a number of assumptions. As discussed in the background section, there is substantial evidence that neuronal activity and field phase are related; cells tend to fire at certain phases of oscillatory components of the extracellular field, and to be silent at others. In that regard, phase in certain frequencies, including beta, can track temporal changes in cortical excitability and cortical activity. Neurons in two cortical sites that are interconnected will tend to fire together and, therefore, at similar field phases. Likewise, if the fields recorded from two sites exhibit phase consistency, and therefore high coherence, one can infer that they could be interconnected. However, phase consistency between signals from two sites does not necessarily imply the presence of a direct connection between them. A third brain area, in the cortex or thalamus, could be providing common input to both, in which case coherence would still be high, even in the absence of a direct connection between them. Another possibility is volume conduction of activity from a third brain area, which would artificially increase coherence (Srinivasan et al. 1998). Furthermore, the choice of reference in recording of extracellular fields can have a profound effect on coherence (Fein et al. 1988; Srinivasan et al. 1998).

Even in the case that CEP amplitude and coherence do not reflect solely the direct anatomical connectivity between two cortical sites but are confounded by activity at a third site, calculating the change in CEP amplitude or coherence caused by stimulation would significantly reduce the contribution of activity from that third site. Such a calculation removes both the effect of passive tissue volume conduction and the effect of the reference electrode. It also minimizes effects from other brain areas, assuming those are not affected by stimulation.

Change in excitability or synaptic modification?

If the CEP at the triggering site (C_{TRIG}), or a control site, represents the “postsynaptic” response to the incoming volley of action potentials elicited by stimulation of the “presynaptic” site (C_{STIM}), then a conditioning-induced change in the magnitude of the CEP could be explained in three ways: it could reflect a change in the strength of the $C_{STIM} \rightarrow C_{TRIG}$ synaptic connection, a change in the excitability of cells at C_{STIM}, or a change in the excitability of cells at C_{REC}. In the first case, the same stimulus-evoked presynaptic volley would generate an altered postsynaptic response. In the second, the same stimulus would elicit a larger (or smaller) presynaptic volley, and therefore a larger or smaller postsynaptic response, without synaptic modification. In the third case, the same presynaptic volley would generate an altered postsynaptic response, without synaptic modification, as the same synaptic action would this time elicit larger or smaller activity from more or less excitable postsynaptic cells.

If the conditioning effect is mediated by a change in the excitability of C_{STIM}, we would expect that, for a given experiment, the change in the CEP at C_{TRIG} would be similar to the change in the CEP at all control sites. Even though in the vast majority of the experiments, control sites did show changes in the CEP, the magnitude of these change was typically smaller than that of the change at C_{TRIG} (Figure 21)(Figure 22). This differential effect can neither be explained by a possibly larger projection from C_{STIM} preferentially to C_{TRIG} because C_{TRIG} was chosen randomly among all sites with CEPs and the average amplitude of CEPs on C_{TRIG} was no different than that on control sites (Figure 18).

The conditioning effect could theoretically be mediated by a change in the excitability of C_{TRIG}. Such an effect would be produced either by a direct or by a synaptically-mediated effect of stimulation on C_{TRIG}. The first possibility is unlikely, as conditioning effects were seen at short, as well at long (>15 mm) distances between C_{STIM} and C_{TRIG}, or between C_{STIM} and control sites (Figure 20). Based on past experimental (Adrian 1936; El'kina and Trush 1982; Rosenthal et al. 1967) and theoretical studies (Nathan et al. 1993b) and on our own results (discussed in chapter 2), direct effects of cortical surface stimulation at distances >5-10 mm are unlikely. The second possibility requires that CEPs change more at sites that receive a larger projection from C_{STIM}. This can be excluded on the basis that the conditioning effect on C_{TRIG} was typically of greater magnitude than that on control electrodes, without C_{TRIG} necessarily receiving a larger projection from C_{STIM} (Figure 18).

In a very similar experiment to the one described here, Chen (Chen 1993a) showed that repeated intracortical stimulation triggered from the depolarizing phase of field potential oscillations in monkey M1, resulted in an increase in the amplitude of stimulus-evoked excitatory postsynaptic potential (EPSP) responses in nearby single neurons (Figure 35). The stimulus-triggered average EPSP includes two segments: the baseline segment (preceding the stimulus), and the EPSP segment (following the stimulus). The effect on EPSPs is compatible with the effect caused by conditioning on CEP amplitude, and offers further insight into potential mechanisms underlying it. Specifically, it rules out the possibility of increased excitability at C_{TRIG}. Provided that the stimulus-triggered average sweeps accurately reflect the DC level of the baseline segment (i.e. no high-pass filtering), that segment can be thought to be representative the baseline level of depolarization, and therefore neuronal excitability of cells at C_{TRIG}. In regards to that segment, there was no difference between responses to pre- and post-burst test stimuli, something that indicate that conditioning stimulation did not alter C_{TRIG} excitability.

The most likely mechanism for the effect of conditioning stimulation on CEPs is synaptic modification. Typically, the maximal connectivity change for a given triggering phase, and therefore synaptic modification, occurred between C_{STIM} and C_{TRIG}. This is expected given that neuronal activity at C_{TRIG} bears the tightest temporal relationship to stimulus-evoked activation of C_{STIM} (as it is beta phase at C_{TRIG} that triggers every stimulus) and that temporal coincidence between presynaptic and postsynaptic activity is a prerequisite for synaptic modification (see discussion below). Connectivity changes occurred also between C_{STIM} and control sites with CEPs. This is also expected, since during oscillatory episodes cycles at many control sites were in-phase with cycles at C_{TRIG} (Figure 7). The temporal relationship of conditioning stimuli with beta phase at control sites was, however, by necessity more variable than that with beta phase at C_{TRIG} (Figure 6), meaning that stimulus-evoked presynaptic action potentials arrived at control sites at a range of depolarization levels. That would explain why changes in connectivity between C_{STIM} and control sites were generally of smaller magnitude that those between C_{STIM} and C_{TRIG}.

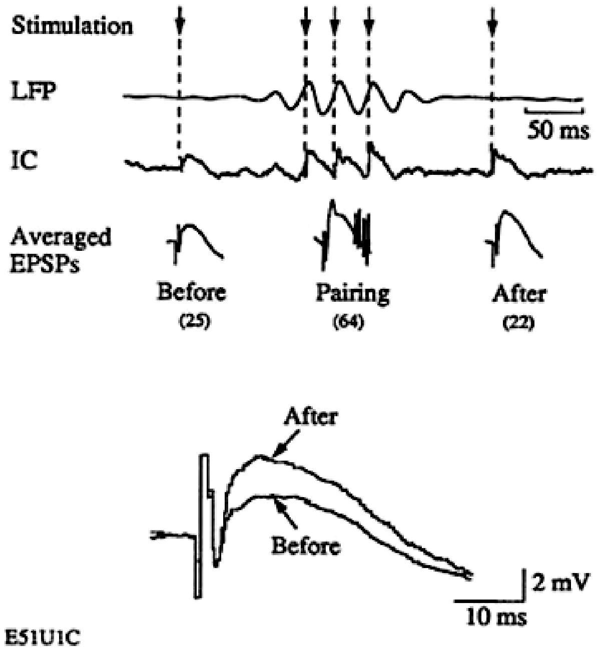

Figure 97. Effect of cycle-triggered conditioning on stimulus-evoked postsynaptic potentials in single neurons. Intracortical stimulation was triggered from the depolarizing phase of local field potential oscillatory cycles ("LFP" panel), while intracellular potential trajectories were recorded from single cells in the vicinity of the stimulating electrode ("IC" panel). Intracellular membrane potential responses to individual stimuli were registered before, during and after the oscillatory episodes and were used to compile stimulus-triggered excitatory postsynaptic potential averages ("EPSPs" panel). Average EPSPs following conditioning bursts were larger than those immediately preceding them (lower panel). From Chen D.F., Ph.D. Thesis, p. 121 (1993)

In some cases, the stimulus phase difference at a control site would result in that site receiving the presynaptic volley at a more “favorable” phase than C_{TRIG}. For example, if stimuli were triggered from a C_{TRIG} phase of 180 degrees, a control site with a +30 degree SPD to C_{TRIG} would experience conditioning stimuli at an average phase of 210 degrees, closer to the (theoretically) optimal depolarizing phase of 270 degrees. At the same time however, the stimulus-by-stimulus variability of phase on the control site would be larger than that on C_{TRIG}. It will be interesting to examine the relative effects of "favorable" SPDs and stimulus phase variability on the connectivity changes at control electrodes. Such a comparison would test whether optimal phase or maximum temporal coincidence is more important for modifications in connectivity.

It is worth noting that the beta phase that triggers stimulation is only an approximation of the postsynaptic potential at the time the stimulus-evoked presynaptic volley arrives at the synapse. This arrival time can actually be estimated by the latency of the CEP. The latency of the onset of CEPs was typically 3-6 ms (Figure 5), corresponding to a phase delay, relative to the triggering phase, of 20-45 degrees (for a beta cycle period of 50 ms). This means that when, for example, stimuli are triggered from the peak of the beta cycle, at a phase of 90 degrees, the presynaptic volley of action potentials elicited by the stimulation will reach the triggering site at an "effective" phase of 105-125 degrees, still within the hyperpolarizing half of the cycle (0-180 degrees), and therefore, based on the synaptic model proposed, will produce depression (Figure 13). Furthermore, if maximal neuronal activity is associated with the trough (~270 degrees) of the beta cycle (Canolty et al. 2010; Murthy and Fetz 1996b), we expect that the triggering phase producing maximum potentiation would be 225 degrees, for an "effective" phase of 245-270 degrees. Even though only 2 conditioning experiments were performed at that triggering phase, the average CEP ratio in those was the highest among all DSP experiments (Figure 13). This model predicts that triggering at a phase of 90 degrees would produce potentiation, whereas triggering at a phase of 360 degrees would produce depression. More conditioning experiments at those triggering phases are needed.

A synaptic model for the conditioning effect

The potentiating or suppressing effect of bursts of stimuli triggered from depolarizing or hyperpolarizing phases of beta cycles can be explained by synaptic potentiation or depression between presynaptic terminals, activated by conditioning stimuli at C_{STIM}, and postsynaptic cells at C_{TRIG}. When presynaptic activity is triggered by, and therefore coincides with, postsynaptic depolarization, synaptic potentiation occurs; when presynaptic activity coincides with relative postsynaptic hyperpolarization synaptic depression occurs (Figure 36). The dependence of the sign of synaptic modification, potentiation or depression, on the level of postsynaptic depolarization has been demonstrated in both the hippocampus (Hanse and Gustafsson 1992; Malenka 1991; Ngezahayo et al. 2000; Wigstrom and Gustafsson 1986) and the neocortex (Artola et al. 1990; Sjostrom et al. 2001). The effect of the level of postsynaptic depolarization on the expression of synaptic modification is thought to be mediated by a voltage-dependent occupation of an NMDA receptor (NMDAR) pore by Mg^{2+}. Depolarization of sufficient magnitude causes $Mg^{2+}$to be completely displaced; when NMDARs are then activated by presynaptically released glutamate, the result is a large influx of Ca^{2+} and subsequent downstream changes that will cause synaptic potentiation. When postsynaptic depolarization is moderate, the displacement is partial; in this case presynaptic activity will result in a smaller influx of Ca^{2+} and activation of different downstream signaling pathways that will cause synaptic depression (Malenka and Bear 2004).

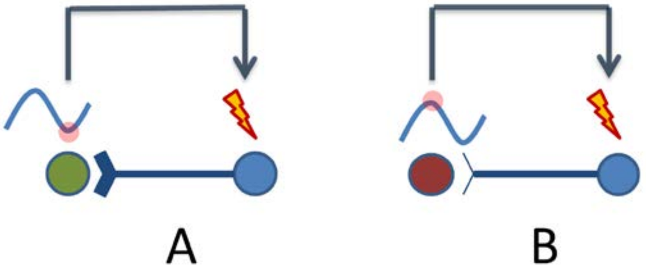

Figure 98. A synaptic model for conditioning-induced changes in effective cortical connectivity. (A) When presynaptic activity, caused by the delivery of conditioning stimuli to presynaptic cells, coincides with postsynaptic depolarization, represented by the depolarizing (negative) phase of the beta oscillation, synaptic potentiation occurs. (B) When presynaptic activity coincides with relative postsynaptic hyperpolarization, represented by the hyperpolarizing (positive) phase of the beta oscillation, synaptic depression occurs.

Induction and duration of synaptic modification

Induction of both long-term potentiation (LTP) and depression (LTD), the two classic forms of synaptic plasticity, typically requires a large number and/or high frequency of presynaptic-postsynaptic pairings (e.g. Sjostrom et al. 2001). We found that 3 consecutive stimuli, at an average frequency of about 20 Hz, were sufficient to induce potentiation (Figure 9) or depression (Figure 11). The exact magnitude of neuronal activation by each stimulus is unknown but, given the current intensity and the location of the stimulating electrode, the cortical volume affected is substantial (Nathan et al. 1993b) and a large number of action potentials are probably elicited. A volley of a large number of presynaptic action potentials arriving at the postsynaptic site nearly simultaneously, during a time window of a few ms, could, through spatiotemporal summation, mimic short, high-frequency stimulation trains that are effective at producing synaptic changes when small numbers of synapses are activated (e.g. Bliss and Gardner-Medwin 1973; Bliss and Lomo 1973; Hanse and Gustafsson 1992; Kauer et al. 1988; Kirkwood et al. 1993).

On the other hand, both LTP and LTD typically last minutes to days (Kuba and Kumamoto 1990), much longer than the conditioning effect observed in this study (1.5-2 s). Short-lived synaptic modification has been described in cases when brief trains of impulses (2-40) at moderate or high frequencies (20-400 Hz) were delivered; it was dependent on postsynaptic NMDAR activation and declined very rapidly, a few seconds to a few minutes, after its induction (e.g. Hanse and Gustafsson 1992; Kauer et al. 1988). It has been suggested that this form of synaptic modification could represent a distinct, albeit still NMDAR-dependent, process from LTP, or an inherent, early phase of LTP that stabilizes when additional conditions are met (Hanse and Gustafsson 1994; Zucker 1989). The conditioning effect seen in our study is compatible with such a form of short-lived synaptic modification.

The time course, both the onset and the decay, of the conditioning effect can be explained by NMDAR activation kinetics. NMDARs activate and deactivate slowly, with a rise time of 10-50 ms and a decay constant of 50-500 ms (Blanke and Van Dongen 2009). The slow kinetics of NMDAR-mediated synaptic currents facilitate temporal summation of synaptic inputs. The first 2 stimuli in a conditioning burst, delivered approximately every 50 ms (for a 20 Hz beta cycle), before NMDA currents have decayed, could serve to build up the required Ca^{2+} transient for downstream plasticity processes. After the end of a conditioning burst, which typically lasts between 100 and 200 ms (Figure 8), NMDAR-mediated currents become progressively smaller. The voltage dependence of the NMDAR-mediated current (Blanke and Van Dongen 2009) could also play a role in the decay rate of the conditioning effect, as well as in its direction (potentiation or depression): the amplitude of the NMDA current is maximal at relatively depolarized membrane potentials (e.g. early after a burst of DPS), and drops at more hyperpolarized membrane potentials (e.g. during HPS).

Short-term synaptic modification

In our discussion so far, we reasoned that the mechanism of expression of the short-lived conditioning effect is likely postsynaptic, as it depends on the level of postsynaptic depolarization. Could the conditioning effects be explained by purely presynaptic models of short-term synaptic plasticity? These changes in synaptic transmission can occur within less than 1 second and decay within a few seconds (Zucker and Regehr 2002), a time-course compatible with the conditioning effect seen in our study.

The rate of neurotransmitter release from stimulus-activated presynaptic terminals for a given stimulus intensity depends on presynaptic excitability, or neuronal activity at C_{STIM}, at the moment of stimulus delivery. Although potentials from C_{STIM} were not recorded during conditioning, it is conceivable that excitability at C_{STIM} wanes and waxes during beta oscillatory episodes, just like in other cortical sites (Figure 7). Assuming that beta phase at C_{STIM} follows, more or less, the beta phase at C_{TRIG} , it follows that spontaneous (baseline) C_{STIM} activity at the time of stimulation will generally be increased in DPS experiments, and decreased in HPS experiments. Increased baseline presynaptic activity may be associated with an elevated Ca^{2+} concentration at presynaptic terminals; elevated residual presynaptic Ca^{2+} at the time of neurotransmitter release is considered the primary mechanism for short-term potentiation (Zucker and Regehr 2002). It is not clear, however, how decreased baseline presynaptic activity, during HPS, could be associated with STD. Presynaptic STD is thought to arise from neurotransmitter depletion after a strong release event (Zucker and Regehr 2002) and would not be expected to occur under low-level baseline presynaptic activity.

It should, finally, be noted that the CEP measure used in the present study reflects events from a very large population of synapses. Given the variety of short- and long-term synaptic plasticity processes that co-exist in the same populations of synapses (Fisher et al. 1997), this population response likely reflects a mixture of synaptic potentiations and depressions of different induction and decay kinetics.

Effects of conditioning on phase coherence

The presence of phase coherence between two sites implies correlated neuronal activity (Rosenberg et al. 1989; Schlogl and Supp 2006). Both the time course of recorded signals (Figure 3) and their coherence spectra (e.g. Figure 24) indicate that the most prominent oscillations are in low frequencies (<10 Hz) and in the beta range (15-25 Hz). It is thought that slow (mainly theta and alpha) cortical oscillations arise from the entrainment of large cortical areas by thalamic networks, via extensive thalamocortical connections (Hughes and Crunelli 2005; Steriade 2005; 2001). In contrast, thalamocortical and intracortical networks mechanisms, as well as active membrane properties of cortical neurons have been implicated in the generation of beta oscillations (Miller 2007; Reimann et al. 2013; Steriade 2005). Conditioning caused coherence changes in both low frequencies and the beta range.

Theoretically, and excluding effects from the reference electrode and volume conduction, two factors could contribute to a change in coherence between two cortical sites (Nunez 2000): (a) a change in the degree of correlation between activities at each of the two sites and at a third (e.g. thalamic) site connected to both, (b) a change in the degree of correlation between activities at the two cortical sites.

The nonspecific effect of conditioning on coherence across both stimulated and non-stimulated sites at low frequencies suggests that cortical stimulation may have enhanced the entrainment of cortical activity by thalamic systems. A substantial body of research has documented a “synchronizing” effect of repetitive transcranial magnetic stimulation (rTMS) on slow oscillations across wide cortical areas, believed to represent increased thalamocortical synchrony (e.g. Azila Noh and Fuggetta 2012; Brignani et al. 2008; Fuggetta et al. 2005; Fuggetta and Noh 2013; Johnson et al. 2010; Klimesch et al. 2003; Paus et al. 2001). Ours is the first demonstration of such an effect arising from cortical surface stimulation.

The effect of conditioning on beta range coherence was more specific. In DPS experiments beta coherence between C_{TRIG} and C_{STIM} increased (Figure 31), whereas beta coherence between C_{TRIG} and control sites decreased (Figure 32). In contrast, HPS caused a drop in beta coherence between C_{TRIG} and C_{STIM} (Figure 33), as well as between C_{TRIG} and control sites (Figure 34). This effect, at least for DPS, cannot be explained by an overall increase in cortical excitability or in cortico-cortical or thalamo-cortical synchrony, as beta coherence between C_{TRIG} and control electrodes did not follow this pattern. It is more likely that this change reflects enhancement of cortical connectivity, and hence synaptic transmission, between C_{TRIG} and C_{STIM}. This effect persists until several minutes after the end of the conditioning session, which is considerably longer than the duration of the conditioning effect on CEP amplitude. If the fast decay of effect on CEPs is related to NMDAR kinetics, the much slower decay of the effect on coherence might instead reflect the kinetics of a later stage in the synaptic plasticity cascade, such as dendritic Ca^{2+} currents, or AMPA receptor changes (Malenka and Bear 2004).

Beta oscillations and synaptic plasticity

During episodes of beta oscillations in the sensorimotor cortex, activity of cells across widely separated sites becomes synchronized to the beta cycles. Since many forms of synaptic plasticity rely on the temporal association between presynaptic and postsynaptic activity, beta oscillatory episodes could be a mechanism for ongoing selection of the neuronal populations that will take part in synaptic plasticity events, and at which time windows. In this study, we demonstrated that when activity of large populations of neurons is triggered from spontaneously occurring beta oscillations, it can lead to a short-term modification in cortico-cortical connectivity and synaptic transmission. That modification was maximal between sites whose activity had the highest synchrony, and its direction, potentiation or depression, was determined by the timing of the triggered presynaptic activity relative to the phase of the beta oscillation. Induction of this form of plasticity suggests that one of the functions of ongoing beta oscillations in sensorimotor cortex might be the selection of subsets of synapses that will, under the continuous drive of spatiotemporal patterns of cortical activity (Canolty et al. 2010; Rubino et al. 2006), form, maintain or change functional neuronal ensembles (Engel and Fries 2010).

Beta oscillations have been implicated in attentional top-down processing in various cortical areas (Buschman and Miller 2009; 2007; Fetz 2013; Pesaran et al. 2008) and sensorimotor beta oscillations have been documented in tasks that require attention and involve visuomotor coordination, in both monkeys (Murthy and Fetz 1996a) and humans (Aoki et al. 1999). Since attention is closely associated with successful motor learning (Hikosaka et al. 2002), it will be interesting to examine whether activity-dependent, long-term synaptic plasticity in the motor cortex (Jackson et al. 2006a) can be modulated by beta oscillations.

Chapter 5: Conclusions

Electrocorticography (ECoG) is now a widely used recording modality for cortical activity, in both human subjects and experimental animals. The number of ECoG -related papers indexed on PubMed has been steadily increasing in the past 50 years (Figure 1). The high signal-to-noise ratio of ECoG signals, the capability of ECoG arrays to sample small, as well as large cortical areas, and the increased clinical relevance of much of ECoG research are some of the reasons why this technique will likely be used increasingly as a brain "imaging" tool.

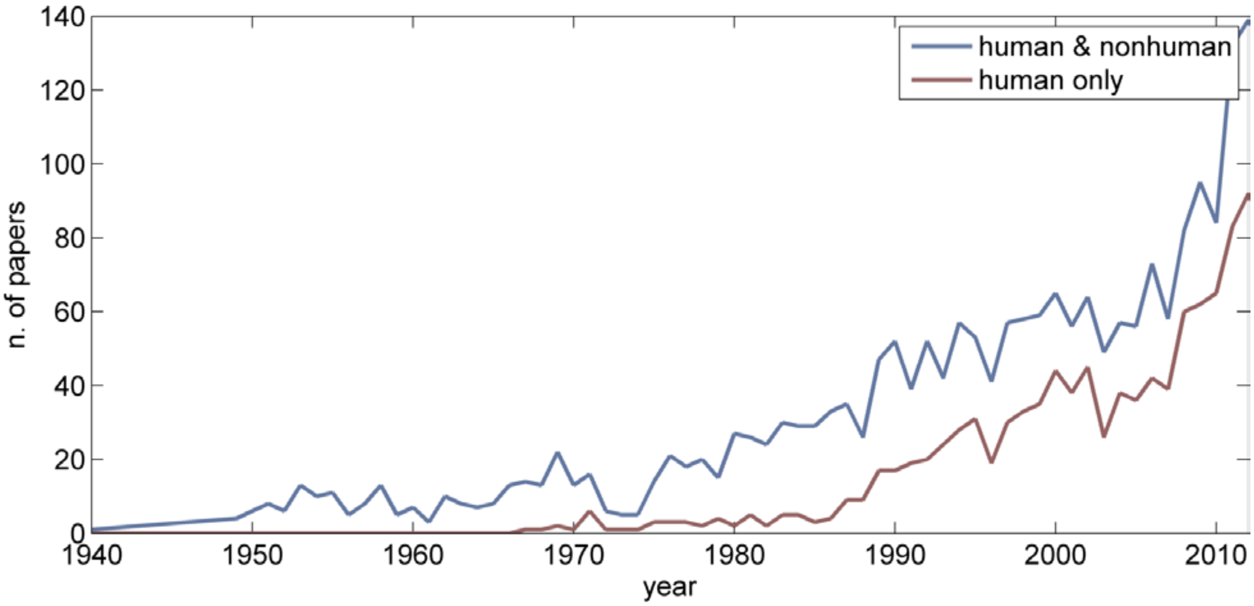

Figure 99. Number of ECoG-related papers indexed on PubMed, across the last 70 years; shown is the total number of papers (human and nonhuman subjects), and the number of papers with human subjects only.

The use of ECoG signals in decoding variables of motor and imagined movement in acute experiments is well established. Our finding, that such ECoG decoders can perform in open-loop mode over long periods of time with a relatively slow drop in performance, indicates that ECoG is compatible with chronic BCI applications. The gradual drop we observed in the signal-to-noise ratio of high-frequencies with advancing implant age is probably due to the development of reactive gliosis which, after about 6-12 months, was significant. Novel engineering solutions are being investigated to minimize the effect of gliosis on ECoG recordings (e.g. Schendela et al. 2013). Reduced tissue response when the pia remains intact is an important advantage of ECoG arrays over intracortical implants that needs to be further exploited.

Research using cortical surface electrodes today is still concentrated around their use as a method for recording from the cortex, rather than stimulating it. Despite the surge of interest on ECoG and its use in BCI applications, most papers discussing stimulation with ECoG electrodes outside of clinical cortical stimulation mapping were published before 1975 (e.g. Adrian 1936; Burns 1954; Craggs et al. 1976; Curtis 1940; Graham Brown and Sherrington 1912; Rosenthal et al. 1967). However, this situation is likely to change soon. A recent study reported that human subjects implanted with ECoG arrays for clinical reasons were able to discriminate between high- and low-frequency trains of stimuli delivered through the subdural electrodes (Johnson et al. 2013). This observation raises the possibility of using invasive electrical cortical surface stimulation (ECS) as a method for delivering sensory feedback directly into the brain, in the context of by-passing an injured efferent pathway. Another field in which ECS has recently seen some limited use is that of neurorehabilitation. A number of basic and clinical studies explored the use of repetitive, invasive ECS as a method for facilitating adaptive neuroplastic changes in animal models of stroke and in stroke patients (reviewed in Edwardson et al. 2013; Plow et al. 2009). Our own observations on the spatial extent and the time course of the effects of prolonged, repetitive, invasive ECS on the electrode-tissue interface, cortical excitability and spontaneous cortical activity will be useful in the design of safe and effective chronic invasive cortical stimulation systems.

Given that cortical surface electrodes can be used both for recording potentials from the cortex and delivering stimulation to the cortex, they are suitable for use in recurrent BCI (rBCI) systems. Such systems can be used to bridge two sites in the nervous system whose communication has been interrupted; for example, ECoG activity patterns that can be volitionally controlled could drive functional electrical stimulation (FES) of different muscles to generate movement, much like volitionally-controlled single unit activity drove FES of flexor and extensor muscles in a cursor tracking task (Moritz et al. 2008). An rBCI with cortical surface electrodes can also find application in activity-dependent stimulation protocols aiming at promoting plasticity between cortical sites, much like spike-triggered (Jackson et al. 2006a; Nishimura et al. (in press); Rebesco et al. 2010) or EMG-triggered (Lucas and Fetz 2013) intracortical stimulation leads to reorganization of functional maps of motor cortical areas. The development of the Neurochip2 (Zanos et al. 2011), which can record ECoG potentials, process them in real-time and deliver ECS triggered by different ECoG features will allow many of these possibilities to be explored.

Our finding that certain phases of ongoing, large-scale oscillations in the sensorimotor cortex are associated with short-term synaptic modification induced by closed-loop stimulation provides insight into what one of the physiological functions of these oscillations may be and how to harness it to control cortical plasticity. The fact that the effect of conditioning was dependent on the phase difference between cycles at different cortical sites indicates that, depending on the sites, there are different optimal time delays for the induction of activity-dependent plasticity. This raises the possibility that patterned cortical stimulation, with appropriate trigger-stimulus time delays, might be effective at producing plasticity across large cortical areas during the same conditioning session. This would be particularly relevant to models of cortical plasticity after ischemic stroke, where large cortical areas around the infarct need to be stimulated to promote functional reorganization (e.g. Adkins et al. 2008). The Neurochip2, with its independently controlled output channels, can implement such stimulation patterns.

A population pattern like the beta oscillation might correlate with a temporal window during which stimulation-induced synaptic plasticity is more likely, but its precise temporal relationship to underlying neuronal activity may be too variable to produce the long-lasting connectivity changes that occur with spike-triggered stimulation (Jackson et al. 2006a; Nishimura et al. (in press)). It is instead possible that each cycle-triggered stimulus leads to a combination of synaptic potentiation and depression, of which the net effect is a short-lasting change in cortical connectivity. Triggering cortical stimulation on a joint contingency of beta cycles and spike timing, or an ECoG-signature of localized neuronal activity like high-gamma power, might maximize the effectiveness of conditioning and increase the duration of its effects. On the other hand, cortical activity complexes, such as those occurring during certain sleep stages, have also been associated with increased potential for cortical plasticity (e.g. Chauvette et al. 2012), and stimulation triggered by sleep-associated cortical patterns might offer new insights into the temporal and spatial organization of sleep-related plasticity and memory consolidation (Ngo et al. 2013). A new version of the Neurochip, that will implement such combined contingencies, is under construction at the Fetz lab. Experiments like these will make use of cortical surface rBCIs in order to probe cortical function in ways unattainable by single unit-based studies.

References

Abdi H. Partial least squares regression and projection on latent structure regression (PLS regression). *Wiley Interdisciplinary Reviews: Computational Statistics* 2: 97-106, 2010.

Adkins DL, Hsu JE, and Jones TA. Motor cortical stimulation promotes synaptic plasticity and behavioral improvements following sensorimotor cortex lesions. *Experimental neurology* 212: 14-28, 2008.

Adrian ED. The spread of activity in the cerebral cortex. *The Journal of physiology* 88: 127-161, 1936.

Allison T, McCarthy G, Wood CC, and Jones SJ. Potentials evoked in human and monkey cerebral cortex by stimulation of the median nerve. A review of scalp and intracranial recordings. *Brain* 114 (Pt 6): 2465-2503, 1991.

Anderson NR, Blakely T, Schalk G, Leuthardt EC, and Moran DW. Electrocorticographic (ECoG) correlates of human arm movements. *Exp Brain Res* 223: 1-10, 2012.

Anderson WS, Kudela P, Cho J, Bergey GK, and Franaszczuk PJ. Studies of stimulus parameters for seizure disruption using neural network simulations. *Biol Cybern* 97: 173-194, 2007.

Aoki F, Fetz EE, Shupe L, Lettich E, and Ojemann GA. Increased gamma-range activity in human sensorimotor cortex during performance of visuomotor tasks. *Clin Neurophysiol* 110: 524-537, 1999.

Arezzo J, Legatt AD, and Vaughan HG, Jr. Topography and intracranial sources of somatosensory evoked potentials in the monkey. I. Early components. *Electroencephalogr Clin Neurophysiol* 46: 155-172, 1979.

Arezzo JC, Vaughan HG, Jr., and Legatt AD. Topography and intracranial sources of somatosensory evoked potentials in the monkey. II. Cortical components. *Electroencephalogr Clin Neurophysiol* 51: 1-18, 1981.

Artola A, Brocher S, and Singer W. Different voltage-dependent thresholds for inducing long-term depression and long-term potentiation in slices of rat visual cortex. *Nature* 347: 69-72, 1990.

Asanuma H, and Rosen I. Spread of mono- and polysynaptic connections within cat's motor cortex. *Exp Brain Res* 16: 507-520, 1973.

Azila Noh N, and Fuggetta G. Human cortical theta reactivity to high-frequency repetitive transcranial magnetic stimulation. *Hum Brain Mapp* 33: 2224-2237, 2012.

Bagshaw EV, and Evans MH. Measurement of current spread from microelectrodes when stimulating within the nervous system. *Exp Brain Res* 25: 391-400, 1976.

Baker SN, Kilner JM, Pinches EM, and Lemon RN. The role of synchrony and oscillations in the motor output. *Exp Brain Res* 128: 109-117, 1999.

Bancroft JD, and Gamble M. *Theory and practice of histological techniques, 6th Ed.* New York: Churchill Livingstone, 2007.

Bansal AK, Truccolo W, Vargas-Irwin CE, and Donoghue JP. Decoding 3D reach and grasp from hybrid signals in motor and premotor cortices: spikes, multiunit activity, and local field potentials. *J Neurophysiol* 107: 1337-1355, 2012.

Barsoukov E, and Mcdonald JR. *Impedance spectroscopy: theory, experiment, and applications*. Hoboken: John Wiley & Sons Inc., 2005.

Berger MS, Ojemann GA, and Lettich E. Neurophysiological monitoring during astrocytoma surgery. *Neurosurg Clin N Am* 1: 65-80, 1990.

Birbaumer N. Breaking the silence: brain-computer interfaces (BCI) for communication and motor control. *Psychophysiology* 43: 517-532, 2006.

Blanke ML, and Van Dongen AMJ. Activation mechanisms of the NMDA receptor. In: *Biology of the NMDA receptor*, edited by Van Dongen AMJ. Boca Raton (FL): CRC Press, 2009, p. 283-312.

Bliss TV, and Gardner-Medwin AR. Long-lasting potentiation of synaptic transmission in the dentate area of the unanaestetized rabbit following stimulation of the perforant path. *J Physiol* 232: 357-374, 1973.

Bliss TV, and Lomo T. Long-lasting potentiation of synaptic transmission in the dentate area of the anaesthetized rabbit following stimulation of the perforant path. *J Physiol* 232: 331-356, 1973.

Braitenberg V, and Schuz A. *Anatomy of the cortex: Statistics and geometry*. New York: Springer, 1991.

Brignani D, Manganotti P, Rossini PM, and Miniussi C. Modulation of cortical oscillatory activity during transcranial magnetic stimulation. *Hum Brain Mapp* 29: 603-612, 2008.

Brochier T, Spinks RL, Umilta MA, and Lemon RN. Patterns of muscle activity underlying object-specific grasp by the macaque monkey. *J Neurophysiol* 92: 1770-1782, 2004.

Brodmann K. *Brodmann's Localization in the Cerebral Cortex (translated with editorial notes and an introduction)*. London: Imperial College Press, 2009.

Brown GT, and Sherrington CS. On the instability of a cortical point. *Proc Royal Soc London, Series B* 85: 250-277, 1912.

Burns BD. The production of after-bursts in isolated unanesthetized cerebral cortex. *The Journal of physiology* 125: 427-446, 1954.

Buschman TJ, and Miller EK. Serial, covert shifts of attention during visual search are reflected by the frontal eye fields and correlated with population oscillations. *Neuron* 63: 386-396, 2009.

Buschman TJ, and Miller EK. Top-down versus bottom-up control of attention in the prefrontal and posterior parietal cortices. *Science* 315: 1860-1862, 2007.

Buzsaki G, and Draguhn A. Neuronal oscillations in cortical networks. *Science* 304: 1926-1929, 2004.

Canolty RT, Ganguly K, and Carmena JM. Task-dependent changes in cross-level coupling between single neurons and oscillatory activity in multiscale networks. *PLoS Comput Biol* 8: e1002809, 2012.

Canolty RT, Ganguly K, Kennerley SW, Cadieu CF, Koepsell K, Wallis JD, and Carmena JM. Oscillatory phase coupling coordinates anatomically dispersed functional cell assemblies. *Proc Natl Acad Sci U S A* 107: 17356-17361, 2010.

Carmena JM, Lebedev MA, Crist RE, O'Doherty JE, Santucci DM, Dimitrov DF, Patil PG, Henriquez CS, and Nicolelis MA. Learning to control a brain-machine interface for reaching and grasping by primates. *PLoS Biol* 1: E42, 2003.

Carmena JM, Lebedev MA, Henriquez CS, and Nicolelis MA. Stable ensemble performance with single-neuron variability during reaching movements in primates. *J Neurosci* 25: 10712-10716, 2005.

Carter GC. Coherence and time delay estimation. *Proc IEEE* 75: 236-255, 1987.

Chao. Long-term asynchronous decoding of arm motion using electrocorticographic signals in monkey. *Frontiers in Neuroengineering* 2010.

Chapin JK, Moxon KA, Markowitz RS, and Nicolelis MA. Real-time control of a robot arm using simultaneously recorded neurons in the motor cortex. *Nat Neurosci* 2: 664-670, 1999.

Charlet de Sauvage R, Lima da Costa D, Erre JP, and Aran JM. Electrical and physiological changes during short-term and chronic electrical stimulation of the normal cochlea. *Hearing research* 110: 119-134, 1997.

Chauvette S, Seigneur J, and Timofeev I. Sleep oscillations in the thalamocortical system induce long-term neuronal plasticity. *Neuron* 75: 1105-1113, 2012.

Chen DF. Synaptic interactions between primate cortical neurons revealed by in vivo intracellular potentials. In: *Dept of Physiology and Biophysics*. Seattle: University of Washington, 1993a.

Chen DF. Synaptic interactions between primate cortical neurons revealed by in vivo intracellular potentials. In: *Physiology and Biophysics*. Seatte: University of Washington, 1993b.

Chen R, Classen J, Gerloff C, Celnik P, Wassermann EM, Hallett M, and Cohen LG. Depression of motor cortex excitability by low-frequency transcranial magnetic stimulation. *Neurology* 48: 1398-1403, 1997.

Cherian A, Krucoff MO, and Miller LE. Motor cortical prediction of EMG: evidence that a kinetic brain-machine interface may be robust across altered movement dynamics. *J Neurophysiol* 106: 564-575, 2011.

Chestek CA, Gilja V, Nuyujukian P, Foster JD, Fan JM, Kaufman MT, Churchland MM, Rivera-Alvidrez Z, Cunningham JP, Ryu SI, and Shenoy KV. Long-term stability of neural prosthetic control signals from silicon cortical arrays in rhesus macaque motor cortex. *J Neural Eng* 8: 045005, 2011.

Colgin LL, Denninger T, Fyhn M, Hafting T, Bonnevie T, Jensen O, Moser MB, and Moser EI. Frequency of gamma oscillations routes flow of information in the hippocampus. *Nature* 462: 353-357, 2009.

Craggs MD. Cortical control of motor prostheses: using the cord-transected baboon as the primate model for human paraplegia. *Adv Neurol* 10: 91-101, 1975.

Craggs MD, Rushton DN, and Clayton DG. The stability of the electrical stimulation map of the motor cortex of the anesthetized baboon. *Brain : a journal of neurology* 99: 575-600, 1976.

Crone NE, Sinai A, and Korzeniewska A. High-frequency gamma oscillations and human brain mapping with electrocorticography. *Prog Brain Res* 159: 275-295, 2006.

Csicsvari J, Jamieson B, Wise KD, and Buzsaki G. Mechanisms of gamma oscillations in the hippocampus of the behaving rat. *Neuron* 37: 311-322, 2003.

Curtis HJ. Intercortical connections of corpus callosum as indicated by evoked potentials. *Journal of neurophysiology* 3: 407-413, 1940.

de Jong S. SIMPLS: An alternative approach to partial least squares regression. *Chemometrics and Intelligent Laboratory Systems* 18: 251-263, 1993.

Do AH, Wang PT, King CE, Schombs A, Cramer SC, and Nenadic Z. Brain-computer interface controlled functional electrical stimulation device for foot drop due to stroke. *Conf Proc IEEE Eng Med Biol Soc* 2012: 6414-6417, 2012.

Dobelle WH. Artificial vision for the blind by connecting a television camera to the visual cortex. *ASAIO J* 46: 3-9, 2000.

Donoghue JP. Bridging the brain to the world: a perspective on neural interface systems. *Neuron* 60: 511-521, 2008.

Donoghue JP, Sanes JN, Hatsopoulos NG, and Gaal G. Neural discharge and local field potential oscillations in primate motor cortex during voluntary movements. *J Neurophysiol* 79: 159-173, 1998.

Douglas RJ, and Martin KA. Neuronal circuits of the neocortex. *Annu Rev Neurosci* 27: 419-451, 2004.

Douglas RJ, and Martin KA. Recurrent neuronal circuits in the neocortex. *Curr Biol* 17: R496-500, 2007.

Duffau H. Contribution of cortical and subcortical electrostimulation in brain glioma surgery: methodological and functional considerations. *Neurophysiol Clin* 37: 373-382, 2007.

Dum RP, and Strick PL. Frontal lobe inputs to the digit representations of the motor areas on the lateral surface of the hemisphere. *J Neurosci* 25: 1375-1386, 2005.

Edwardson MA, Lucas TH, Carey JR, and Fetz EE. New modalities of brain stimulation for stroke rehabilitation. *Experimental brain research Experimentelle Hirnforschung Experimentation cerebrale* 224: 335-358, 2013.

El'kina GA, and Trush VD. Effect of level of spatial synchronization of cortical potentials on spread of evoked responses to cortical electrical stimulation. *Neurosci Behav Physiol* 12: 301-307, 1982.

Enatsu R, Kubota Y, Kakisaka Y, Bulacio J, Piao Z, O'Connor T, Horning K, Mosher J, Burgess RC, Bingaman W, and Nair DR. Reorganization of posterior language area in temporal lobe epilepsy: a cortico-cortical evoked potential study. *Epilepsy Res* 103: 73-82, 2013.

Engel AK, and Fries P. Beta-band oscillations--signalling the status quo? *Curr Opin Neurobiol* 20: 156-165, 2010.

Engel AK, Konig P, Kreiter AK, and Singer W. Interhemispheric synchronization of oscillatory neuronal responses in cat visual cortex. *Science* 252: 1177-1179, 1991a.

Engel AK, Kreiter AK, Konig P, and Singer W. Synchronization of oscillatory neuronal responses between striate and extrastriate visual cortical areas of the cat. *Proc Natl Acad Sci U S A* 88: 6048-6052, 1991b.

Fanardjian VV, and Papoyan EV. Electrophysiological evidence for a direct neuronal connection from the motor cortex to the parietal association cortex of the cat. *Neurosci Lett* 184: 201-203, 1995.

Fein G, Raz J, Brown FF, and Merrin EL. Common reference coherence data are confounded by power and phase effects. *Electroencephalogr Clin Neurophysiol* 69: 581-584, 1988.

Fetz EE. Volitional control of cortical oscillations and synchrony. *Neuron* 77: 216-218, 2013.

Fetz EE, and Cheney PD. Postspike facilitation of forelimb muscle activity by primate corticomotoneuronal cells. *J Neurophysiol* 44: 751-772, 1980.

Fetz EE, Toyama K, and Smith W. Synaptic interactions between cortical neurons. In: *Cerebral Cortex*, edited by Peters A, and Jones EG. New York: Plenum Publishing Corp., 1991, p. 1-47.

Fisher SA, Fischer TM, and Carew TJ. Multiple overlapping processes underlying short-term synaptic enhancement. *Trends Neurosci* 20: 170-177, 1997.

Fitzgibbon SP, Lewis TW, Powers DM, Whitham EW, Willoughby JO, and Pope KJ. Surface laplacian of central scalp electrical signals is insensitive to muscle contamination. *IEEE Trans Biomed Eng* 60: 4-9, 2013.

Flint RD, 3rd, Ethier C, Oby ER, Miller LE, and Slutzky MW. Local field potentials allow accurate decoding of muscle activity. *J Neurophysiol* 2012a.

Flint RD, Ethier C, Oby ER, Miller LE, and Slutzky MW. Local field potentials allow accurate decoding of muscle activity. *J Neurophysiol* 108: 18-24, 2012b.

Flint RD, Lindberg EW, Jordan LR, Miller LE, and Slutzky MW. Accurate decoding of reaching movements from field potentials in the absence of spikes. *J Neural Eng* 9: 046006, 2012c.

Freeman WJ. Harmonic oscillation as model for cortical excitability changes with attention in cats. *Science* 133: 2058-2059, 1961.

Freeman WJ, Rogers LJ, Holmes MD, and Silbergeld DL. Spatial spectral analysis of human electrocorticograms including the alpha and gamma bands. *J Neurosci Methods* 95: 111-121, 2000.

Fries P. A mechanism for cognitive dynamics: neuronal communication through neuronal coherence. *Trends Cogn Sci* 9: 474-480, 2005.

Fuggetta G, Fiaschi A, and Manganotti P. Modulation of cortical oscillatory activities induced by varying single-pulse transcranial magnetic stimulation intensity over the left primary motor area: a combined EEG and TMS study. *Neuroimage* 27: 896-908, 2005.

Fuggetta G, and Noh NA. A neurophysiological insight into the potential link between transcranial magnetic stimulation, thalamocortical dysrhythmia and neuropsychiatric disorders. *Exp Neurol* 245: 87-95, 2013.

Ganguly K, and Carmena JM. Emergence of a stable cortical map for neuroprosthetic control. *PLoS Biol* 7: e1000153, 2009.

Geddes LA, and Roeder R. Criteria for the selection of materials for implanted electrodes. *Annals of biomedical engineering* 31: 879-890, 2003a.

Geddes LA, and Roeder R. Criteria for the selection of materials for implanted electrodes. *Ann Biomed Eng* 31: 879-890, 2003b.

Gerven Mv, Farquhar J, Schaefer R, Vlek R, Geuze J, Nijholt A, Ramsey N, Haselager P, Vuurpijl L, Gielen S, and Desain P. The brain–computer interface cycle. *J Neural Eng* 6: 041001, 2009.

Gevins AS, Doyle JC, Cutillo BA, Schaffer RE, Tannehill RS, Ghannam JH, Gilcrease VA, and Yeager CL. Electrical potentials in human brain during cognition: new method reveals dynamic patterns of correlation. *Science* 213: 918-922, 1981.

Ghosh PM, Keese CR, and Giaever I. Monitoring electropermeabilization in the plasma membrane of adherent mammalian cells. *Biophysical journal* 64: 1602-1609, 1993.

Godschalk M, Mitz AR, van Duin B, and van der Burg H. Somatotopy of monkey premotor cortex examined with microstimulation. *Neurosci Res* 23: 269-279, 1995.

Goncharova, II, McFarland DJ, Vaughan TM, and Wolpaw JR. EMG contamination of EEG: spectral and topographical characteristics. *Clinical neurophysiology : official journal of the International Federation of Clinical Neurophysiology* 114: 1580-1593, 2003.

Gonzalez J, Horiuchi Y, and Yu W. Classification of upper limb motions from around-shoulder muscle activities: hand biofeedback. *Open Med Inform J* 4: 74-80, 2010.

Graham Brown T, and Sherrington R. On the instability of a cortical point. *Proc Royal Soc London B* 85: 250-277, 1912.

Green AM, and Kalaska JF. Learning to move machines with the mind. *Trends Neurosci* 34: 61-75, 2011.

Greenblatt RE, and Pflieger ME. Randomization-based hypothesis testing from event-related data. *Brain Topogr* 16: 225-232, 2004.

Grenier F, Timofeev I, and Steriade M. Focal synchronization of ripples (80-200 Hz) in neocortex and their neuronal correlates. *J Neurophysiol* 86: 1884-1898, 2001.

Griffin DM, Hudson HM, Belhaj-Saif A, McKiernan BJ, and Cheney PD. Do corticomotoneuronal cells predict target muscle EMG activity? *J Neurophysiol* 99: 1169-1986, 2008.

Griffith RW, and Humphrey DR. Long-term gliosis around chronically implanted platinum electrodes in the Rhesus macaque motor cortex. *Neurosci Lett* 406: 81-86, 2006.

Gustafsson B, and Jankowska E. Direct and indirect activation of nerve cells by electrical pulses applied extracellularly. *J Physiol* 258: 33-61, 1976.

Gwinn RP, Spencer DD, Spencer SS, Duckrow RB, Vives K, Wu K, Tkeshelashvili D, and Zaveri HP. Local spatial effect of 50 Hz cortical stimulation in humans. *Epilepsia* 49: 1602-1610, 2008.

Hanse E, and Gustafsson B. Onset and stabilization of NMDA receptor-dependent hippocampal long-term potentiation. *Neurosci Res* 20: 15-25, 1994.

Hanse E, and Gustafsson B. Postsynaptic, but not presynaptic, activity controls the early time course of long-term potentiation in the dentate gyrus. *J Neurosci* 12: 3226-3240, 1992.

Harris KD. Neural signatures of cell assembly organization. *Nat Rev Neurosci* 6: 399-407, 2005.

Hatsopoulos NG, and Donoghue JP. The Science of Neural Interface Systems. *Annual Review of Neuroscience* 32: 249-266, 2009a.

Hatsopoulos NG, and Donoghue JP. The science of neural interface systems. *Annu Rev Neurosci* 32: 249-266, 2009b.

Havenith MN, Yu S, Biederlack J, Chen NH, Singer W, and Nikolic D. Synchrony makes neurons fire in sequence, and stimulus properties determine who is ahead. *J Neurosci* 31: 8570-8584, 2011.

Hayashi N, Nishijo H, Ono T, Endo S, and Tabuchi E. Generators of somatosensory evoked potentials investigated by dipole tracing in the monkey. *Neuroscience* 68: 323-338, 1995.

He SQ, Dum RP, and Strick PL. Topographic organization of corticospinal projections from the frontal lobe: motor areas on the medial surface of the hemisphere. *J Neurosci* 15: 3284-3306, 1995.

Heldman DA, Wang W, Chan SS, and Moran DW. Local field potential spectral tuning in motor cortex during reaching. *IEEE Trans Neural Syst Rehabil Eng* 14: 180-183, 2006.

Hess G, Aizenman CD, and Donoghue JP. Conditions for the induction of long-term potentiation in layer II/III horizontal connections of the rat motor cortex. *J Neurophysiol* 75: 1765-1778, 1996.

Hikosaka O, Nakamura K, Sakai K, and Nakahara H. Central mechanisms of motor skill learning. *Curr Opin Neurobiol* 12: 217-222, 2002.

Histed MH, Bonin V, and Reid RC. Direct activation of sparse, distributed populations of cortical neurons by electrical microstimulation. *Neuron* 63: 508-522, 2009.

Hochberg LR, Bacher D, Jarosiewicz B, Masse NY, Simeral JD, Vogel J, Haddadin S, Liu J, Cash SS, van der Smagt P, and Donoghue JP. Reach and grasp by people with tetraplegia using a neurally controlled robotic arm. *Nature* 485: 372-375, 2012.

Holsheimer J, and Feenstra BW. Volume conduction and EEG measurements within the brain: a quantitative approach to the influence of electrical spread on the linear relationship of activity measured at different locations. *Electroencephalogr Clin Neurophysiol* 43: 52-58, 1977.

Hughes SW, and Crunelli V. Thalamic mechanisms of EEG alpha rhythms and their pathological implications. *Neuroscientist* 11: 357-372, 2005.

Jackson A, Gee VJ, Baker SN, and Lemon RN. Synchrony between neurons with similar muscle fields in monkey motor cortex. *Neuron* 38: 115-125, 2003.

Jackson A, Mavoori J, and Fetz EE. Long-term motor cortex plasticity induced by an electronic neural implant. *Nature* 444: 56-60, 2006a.

Jackson A, Moritz CT, Mavoori J, Lucas TH, and Fetz EE. The Neurochip BCI: towards a neural prosthesis for upper limb function. *IEEE transactions on neural systems and rehabilitation engineering : a publication of the IEEE Engineering in Medicine and Biology Society* 14: 187-190, 2006b.

Jankowska E, Padel Y, and Tanaka R. The mode of activation of pyramidal tract cells by intracortical stimuli. *J Physiol* 249: 617-636, 1975.

Johnson JS, Hamidi M, and Postle BR. Using EEG to explore how rTMS produces its effects on behavior. *Brain Topogr* 22: 281-293, 2010.

Johnson LA, Wander JD, Sarma D, Su DK, Fetz EE, and Ojemann JG. Direct electrical stimulation of the somatosensory cortex in humans using electrocorticography electrodes: a qualitative and quantitative report. *Journal of neural engineering* 10: 036021, 2013.

Kauer JA, Malenka RC, and Nicoll RA. NMDA application potentiates synaptic transmission in the hippocampus. *Nature* 334: 250-252, 1988.

Kikuchi T, Matsumoto R, Mikuni N, Yokoyama Y, Matsumoto A, Ikeda A, Fukuyama H, Miyamoto S, and Hashimoto N. Asymmetric bilateral effect of the supplementary motor area proper in the human motor system. *Clin Neurophysiol* 123: 324-334, 2012.

Kim D, Jun SC, and Kim HI. Computational study of subdural and epidural cortical stimulation of the motor cortex. In: *33rd Annual International Conference of the IEEE EMBS*. Boston, MA: 2011, p. 7226-7229.

Kirkwood A, Dudek SM, Gold JT, Aizenman CD, and Bear MF. Common forms of synaptic plasticity in the hippocampus and neocortex in vitro. *Science* 260: 1518-1521, 1993.

Klimesch W, Sauseng P, and Gerloff C. Enhancing cognitive performance with repetitive transcranial magnetic stimulation at human individual alpha frequency. *Eur J Neurosci* 17: 1129-1133, 2003.

Krusienski DJ, and Wolpaw JR. Brain-computer interface research at the wadsworth center developments in noninvasive communication and control. *Int Rev Neurobiol* 86: 147-157, 2009.

Kuba K, and Kumamoto E. Long-term potentiations in vertebrate synapses: a variety of cascades with common subprocesses. *Prog Neurobiol* 34: 197-269, 1990.

Kubanek J, Miller KJ, Ojemann JG, Wolpaw JR, and Schalk G. Decoding flexion of individual fingers using electrocorticographic signals in humans. *J Neural Eng* 6: 066001, 2009.

Lakatos P, Karmos G, Mehta AD, Ulbert I, and Schroeder CE. Entrainment of neuronal oscillations as a mechanism of attentional selection. *Science* 320: 110-113, 2008.

Lauer RT, Peckham PH, and Kilgore KL. EEG-based control of a hand grasp neuroprosthesis. *Neuroreport* 10: 1767-1771, 1999.

Lemon RN. Short-latency peripheral inputs to the motor cortex in conscious monkeys. *Brain Res* 161: 150-155, 1979.

Lemon RN, and van der Burg J. Short-latency peripheral inputs to thalamic neurones projecting to the motor cortex in the monkey. *Exp Brain Res* 36: 445-462, 1979.

Lempka SF. The electrode-tissue interface during recording and stimulation in the central nervous system. In: *Department of Biomedical Engineerign*. Cleveland, OH: Case Western Reseve University, 2010.

Lesser RP, Kim SH, Beyderman L, Miglioretti DL, Webber WR, Bare M, Cysyk B, Krauss G, and Gordon B. Brief bursts of pulse stimulation terminate afterdischarges caused by cortical stimulation. *Neurology* 53: 2073-2081, 1999.

Lesser RP, Luders H, Klem G, Dinner DS, Morris HH, and Hahn J. Cortical afterdischarge and functional response thresholds: results of extraoperative testing. *Epilepsia* 25: 615-621, 1984.

Leyton ASF, and Sherrington CS. Observations on the excitable cortex of the chimpanzee, orangutan and gorilla. *Quart J Exp Physiol* 11: 135-222, 1917.

Li CL, and Chou SN. Cortical intracellular synaptic potentials and direct cortical stimulation. *J Cell Comp Physiol* 60: 1-16, 1962.

Lipton SA, and Rosenberg PA. Excitatory amino acids as a final common pathway for neurologic disorders. *N Engl J Med* 330: 613-622, 1994.

Livanov MN, Gavrilova NA, and Aslanov AS. [Interrelationship between Various Parts of the Human Cerebral Cortex during Intellectual Work]. *Zh Vyssh Nerv Deiat Im I P Pavlova* 14: 185-194, 1964.

Logothetis NK, Augath M, Murayama Y, Rauch A, Sultan F, Goense J, Oeltermann A, and Merkle H. The effects of electrical microstimulation on cortical signal propagation. *Nat Neurosci* 13: 1283-1291, 2010.

Lucas TH, and Fetz EE. Myo-cortical crossed feedback reorganizes primate motor cortex output. *The Journal of neuroscience : the official journal of the Society for Neuroscience* 33: 5261-5274, 2013.

Ludwig KA, Uram JD, Yang J, Martin DC, and Kipke DR. Chronic neural recordings using silicon microelectrode arrays electrochemically deposited with a poly(3,4-ethylenedioxythiophene) (PEDOT) film. *Journal of neural engineering* 3: 59-70, 2006.

Luppino G, Matelli M, Camarda R, and Rizzolatti G. Corticocortical connections of area F3 (SMA-proper) and area F6 (pre-SMA) in the macaque monkey. *J Comp Neurol* 338: 114-140, 1993.

Malenka RC. Postsynaptic factors control the duration of synaptic enhancement in area CA1 of the hippocampus. *Neuron* 6: 53-60, 1991.

Malenka RC, and Bear MF. LTP and LTD: an embarrassment of riches. *Neuron* 44: 5-21, 2004.

Mannard A, and Stein RB. Determination of the frequency response of isometric soleus muscle in the cat using random nerve stimulation. *J Physiol* 229: 275-296, 1973.

Manola L, Holsheimer J, Veltink P, and Buitenweg JR. Anodal vs cathodal stimulation of motor cortex: a modeling study. *Clin Neurophysiol* 118: 464-474, 2007.

Maris E, Schoffelen JM, and Fries P. Nonparametric statistical testing of coherence differences. *J Neurosci Methods* 163: 161-175, 2007.

Matsumoto R, Nair DR, Ikeda A, Fumuro T, Lapresto E, Mikuni N, Bingaman W, Miyamoto S, Fukuyama H, Takahashi R, Najm I, Shibasaki H, and Luders HO. Parieto-frontal network in humans studied by cortico-cortical evoked potential. *Hum Brain Mapp* 33: 2856-2872, 2012.

Matsumoto R, Nair DR, LaPresto E, Bingaman W, Shibasaki H, and Luders HO. Functional connectivity in human cortical motor system: a cortico-cortical evoked potential study. *Brain* 130: 181-197, 2007.

McCreery D. Tissue reaction to electrodes: The problem of safe and effective stimulation of neural tissue. In: *Neuroprosthetics: Theory and practice*, edited by Horch KW, and Dhillon G. Singapore: World Scientific Publishing Co., 2004.

McCreery D, Pikov V, and Troyk PR. Neuronal loss due to prolonged controlled-current stimulation with chronically implanted microelectrodes in the cat cerebral cortex. *Journal of neural engineering* 7: 036005, 2010.

McCreery DB, Agnew WF, and Bullara LA. The effects of prolonged intracortical microstimulation on the excitability of pyramidal tract neurons in the cat. *Ann Biomed Eng* 30: 107-119, 2002.

McCreery DB, Agnew WF, Yuen TG, and Bullara L. Charge density and charge per phase as cofactors in neural injury induced by electrical stimulation. *IEEE transactions on bio-medical engineering* 37: 996-1001, 1990.

McCreery DB, Bullara LA, and Agnew WF. Neuronal activity evoked by chronically implanted intracortical microelectrodes. *Exp Neurol* 92: 147-161, 1986.

McCreery DB, Yuen TG, Agnew WF, and Bullara LA. A characterization of the effects on neuronal excitability due to prolonged microstimulation with chronically implanted microelectrodes. *IEEE transactions on bio-medical engineering* 44: 931-939, 1997.

Merrill DR, Bikson M, and Jefferys JG. Electrical stimulation of excitable tissue: design of efficacious and safe protocols. *J Neurosci Methods* 141: 171-198, 2005.

Miller KJ, Leuthardt EC, Schalk G, Rao RP, Anderson NR, Moran DW, Miller JW, and Ojemann JG. Spectral changes in cortical surface potentials during motor movement. *J Neurosci* 27: 2424-2432, 2007.

Miller KJ, Zanos S, Fetz EE, den Nijs M, and Ojemann JG. Decoupling the cortical power spectrum reveals real-time representation of individual finger movements in humans. *The Journal of neuroscience : the official journal of the Society for Neuroscience* 29: 3132-3137, 2009.

Miller R. Theory of the normal waking EEG: from single neurones to waveforms in the alpha, beta and gamma frequency ranges. *Int J Psychophysiol* 64: 18-23, 2007.

Moran DW, and Schwartz AB. Motor cortical representation of speed and direction during reaching. *J Neurophysiol* 82: 2676-2692, 1999.

Morgan JP. The first reported case of electrical stimulation of the human brain. *J Hist Med Allied Sci* 37: 51-64, 1982.

Moritz CT, Perlmutter SI, and Fetz EE. Direct control of paralysed muscles by cortical neurons. *Nature* 456: 639-642, 2008.

Mosteller F. A k-sample slippage test for an extreme population. *Annals of Mathematical Statistics* 19: 58-65, 1948.

Murthy VN, and Fetz EE. Coherent 25- to 35-Hz oscillations in the sensorimotor cortex of awake behaving monkeys. *Proc Natl Acad Sci U S A* 89: 5670-5674, 1992.

Murthy VN, and Fetz EE. Oscillatory activity in sensorimotor cortex of awake monkeys: synchronization of local field potentials and relation to behavior. *J Neurophysiol* 76: 3949-3967, 1996a.

Murthy VN, and Fetz EE. Synchronization of neurons during local field potential oscillations in sensorimotor cortex of awake monkeys. *J Neurophysiol* 76: 3968-3982, 1996b.

Nathan SS, Lesser RP, Gordon B, and Thakor NV. Electrical stimulation of the human cerebral cortex: Theoretical approach. In: *Electric and magnetic stimulation of the brain and spinal cord*, edited by Devinsky O, Beric A, and Dogali M. New York: Raven Press, Ltd., 1993a, p. 61-85.

Nathan SS, Sinha SR, Gordon B, Lesser RP, and Thakor NV. Determination of current density distributions generated by electrical stimulation of the human cerebral cortex. *Electroencephalography and clinical neurophysiology* 86: 183-192, 1993b.

Nazarpour K, Ethier C, Paninski L, Rebesco JM, Miall RC, and Miller LE. EMG prediction from motor cortical recordings via a nonnegative point-process filter. *IEEE Trans Biomed Eng* 59: 1829-1838, 2012.

Nelson MJ, Pouget P, Nilsen EA, Patten CD, and Schall JD. Review of signal distortion through metal microelectrode recording circuits and filters. *J Neurosci Methods* 169: 141-157, 2008.

Newbold C, Richardson R, Huang CQ, Milojevic D, Cowan R, and Shepherd R. An in vitro model for investigating impedance changes with cell growth and electrical stimulation: implications for cochlear implants. *Journal of neural engineering* 1: 218-227, 2004.

Newbold C, Richardson R, Millard R, Huang C, Milojevic D, Shepherd R, and Cowan R. Changes in biphasic electrode impedance with protein adsorption and cell growth. *Journal of neural engineering* 7: 056011, 2010.

Newbold C, Richardson R, Millard R, Seligman P, Cowan R, and Shepherd R. Electrical stimulation causes rapid changes in electrode impedance of cell-covered electrodes. *Journal of neural engineering* 8: 036029, 2011.

Ngezahayo A, Schachner M, and Artola A. Synaptic activity modulates the induction of bidirectional synaptic changes in adult mouse hippocampus. *J Neurosci* 20: 2451-2458, 2000.

Ngo HV, Martinetz T, Born J, and Molle M. Auditory closed-loop stimulation of the sleep slow oscillation enhances memory. *Neuron* 78: 545-553, 2013.

Nicolelis MA, and Lebedev MA. Principles of neural ensemble physiology underlying the operation of brain-machine interfaces. *Nat Rev Neurosci* 10: 530-540, 2009.

Niedermeyer E. Historical aspects of electroencephalography. In: *Electroencephalography: basic principles, clinical applications, and related fields, 5th Edition*, edited by Niedermeyer E, and Lopes da Silva FH. Philadelphia: Lippincott Williams & Wilkins, 2005.

Nishimura Y, Perlmutter SI, Eaton R, and Fetz E. Spike-timing dependent plasticity in primate corticospinal connections induced during free behavior *Neuron* (in press).

Nishimura Y, Perlmutter SI, and Fetz EE. Restoration of upper limb movement via artificial corticospinal and musculospinal connections in a monkey with spinal cord injury. *Frontiers in neural circuits* 7: 57, 2013.

Nitsche MA, and Paulus W. Excitability changes induced in the human motor cortex by weak transcranial direct current stimulation. *J Physiol* 527 Pt 3: 633-639, 2000.

Nunez PL. *Neocortical dynamics and human EEG rhythms*. New York: Oxford University Press, 1995.

Nunez PL. Toward a quantitative description of large-scale neocortical dynamic function and EEG. *Behav Brain Sci* 23: 371-398; discussion 399-437, 2000.

O'Doherty JE, Lebedev MA, Ifft PJ, Zhuang KZ, Shokur S, Bleuler H, and Nicolelis MA. Active tactile exploration using a brain-machine-brain interface. *Nature* 479: 228-231, 2011.

O'Doherty JE, Lebedev MA, Li Z, and Nicolelis MA. Virtual active touch using randomly patterned intracortical microstimulation. *IEEE Trans Neural Syst Rehabil Eng* 20: 85-93, 2012.

Okun M, Naim A, and Lampl I. The subthreshold relation between cortical local field potential and neuronal firing unveiled by intracellular recordings in awake rats. *J Neurosci* 30: 4440-4448, 2010.

Paralikar KJ, Rao CR, and Clement RS. New approaches to eliminating common-noise artifacts in recordings from intracortical microelectrode arrays: inter-electrode correlation and virtual referencing. *J Neurosci Methods* 181: 27-35, 2009.

Pascual-Leone A, Valls-Sole J, Wassermann EM, and Hallett M. Responses to rapid-rate transcranial magnetic stimulation of the human motor cortex. *Brain* 117 (Pt 4): 847-858, 1994.

Paus T, Sipila PK, and Strafella AP. Synchronization of neuronal activity in the human primary motor cortex by transcranial magnetic stimulation: an EEG study. *J Neurophysiol* 86: 1983-1990, 2001.

Peckham PH, and Knutson JS. Functional Electrical Stimulation for Neuromuscular Applications*. *Annual Review of Biomedical Engineering* 7: 327-360, 2005.

Pell GS, Roth Y, and Zangen A. Modulation of cortical excitability induced by repetitive transcranial magnetic stimulation: influence of timing and geometrical parameters and underlying mechanisms. *Progress in neurobiology* 93: 59-98, 2011.

Penfield W. *The cerebral cortex of man*. New York: Mcmillan, 1950.

Penfield W, and Boldrey E. Somatic motor and sensory representation in the cerebral cortex of man as studied by electrical stimulation. *Brain* 60: 389-443, 1937.

Pesaran B, Nelson MJ, and Andersen RA. Free choice activates a decision circuit between frontal and parietal cortex. *Nature* 453: 406-409, 2008.

Pesaran B, Pezaris JS, Sahani M, Mitra PP, and Andersen RA. Temporal structure in neuronal activity during working memory in macaque parietal cortex. *Nat Neurosci* 5: 805-811, 2002.

Pfurtscheller G, and Lopes da Silva FH. Event-related EEG/MEG synchronization and desynchronization: basic principles. *Clinical neurophysiology : official journal of the International Federation of Clinical Neurophysiology* 110: 1842-1857, 1999.

Pfurtscheller G, Muller GR, Pfurtscheller J, Gerner HJ, and Rupp R. 'Thought'--control of functional electrical stimulation to restore hand grasp in a patient with tetraplegia. *Neurosci Lett* 351: 33-36, 2003.

Pfurtscheller G, Neuper C, Brunner C, and da Silva FL. Beta rebound after different types of motor imagery in man. *Neurosci Lett* 378: 156-159, 2005.

Pfurtscheller G, and Solis-Escalante T. Could the beta rebound in the EEG be suitable to realize a "brain switch"? *Clinical neurophysiology : official journal of the International Federation of Clinical Neurophysiology* 120: 24-29, 2009.

Pfurtscheller G, Stancak A, Jr., and Neuper C. Post-movement beta synchronization. A correlate of an idling motor area? *Electroencephalogr Clin Neurophysiol* 98: 281-293, 1996.

Plow EB, Carey JR, Nudo RJ, and Pascual-Leone A. Invasive cortical stimulation to promote recovery of function after stroke: a critical appraisal. *Stroke; a journal of cerebral circulation* 40: 1926-1931, 2009.

Pohlmeyer EA, Solla SA, Perreault EJ, and Miller LE. Prediction of upper limb muscle activity from motor cortical discharge during reaching. *J Neural Eng* 4: 369-379, 2007.

Priori A, and Lefaucheur JP. Chronic epidural motor cortical stimulation for movement disorders. *Lancet Neurol* 6: 279-286, 2007.

Raos V, Umilta MA, Gallese V, and Fogassi L. Functional properties of grasping-related neurons in the dorsal premotor area F2 of the macaque monkey. *J Neurophysiol* 92: 1990-2002, 2004.

Raos V, Umilta MA, Murata A, Fogassi L, and Gallese V. Functional properties of grasping-related neurons in the ventral premotor area F5 of the macaque monkey. *J Neurophysiol* 95: 709-729, 2006.

Rathelot JA, and Strick PL. Muscle representation in the macaque motor cortex: an anatomical perspective. *Proc Natl Acad Sci U S A* 103: 8257-8262, 2006.

Ray A, Chan L, Thomas B, and Weiland JD. Effects of prolonged stimulation at the electrode-retina interface. *Conference proceedings : Annual International Conference of the IEEE Engineering in Medicine and Biology Society IEEE Engineering in Medicine and Biology Society Conference* 1: 1285-1287, 2006.

Rebesco JM, Stevenson IH, Kording KP, Solla SA, and Miller LE. Rewiring neural interactions by micro-stimulation. *Frontiers in systems neuroscience* 4: 2010.

Reimann MW, Anastassiou CA, Perin R, Hill SL, Markram H, and Koch C. A biophysically detailed model of neocortical local field potentials predicts the critical role of active membrane currents. *Neuron* 79: 375-390, 2013.

Richardson AG, and Fetz EE. Brain state-dependence of electrically evoked potentials monitored with head-mounted electronics. *IEEE Trans Neural Syst Rehabil Eng* 20: 756-761, 2012.

Romo R, Hernandez A, Zainos A, Brody CD, and Lemus L. Sensing without touching: psychophysical performance based on cortical microstimulation. *Neuron* 26: 273-278, 2000.

Romo R, Hernandez A, Zainos A, and Salinas E. Somatosensory discrimination based on cortical microstimulation. *Nature* 392: 387-390, 1998.

Rosenberg JR, Amjad AM, Breeze P, Brillinger DR, and Halliday DM. The Fourier approach to the identification of functional coupling between neuronal spike trains. *Prog Biophys Mol Biol* 53: 1-31, 1989.

Rosenthal J, Waller HJ, and Amassian VE. An analysis of the activation of motor cortical neurons by surface stimulation. *Journal of neurophysiology* 30: 844-858, 1967.

Rubino D, Robbins KA, and Hatsopoulos NG. Propagating waves mediate information transfer in the motor cortex. *Nat Neurosci* 9: 1549-1557, 2006.

Salmelin R, Hamalainen M, Kajola M, and Hari R. Functional segregation of movement-related rhythmic activity in the human brain. *Neuroimage* 2: 237-243, 1995.

Santhanam G, Ryu SI, Yu BM, Afshar A, and Shenoy KV. A high-performance brain-computer interface. *Nature* 442: 195-198, 2006.

Sato KC, and Tanji J. Digit-muscle responses evoked from multiple intracortical foci in monkey precentral motor cortex. *J Neurophysiol* 62: 959-970, 1989.

Schalk G, Kubanek J, Miller KJ, Anderson NR, Leuthardt EC, Ojemann JG, Limbrick D, Moran D, Gerhardt LA, and Wolpaw JR. Decoding two-dimensional movement trajectories using electrocorticographic signals in humans. *J Neural Eng* 4: 264-275, 2007.

Schalk G, and Leuthardt EC. Brain-computer interfaces using electrocorticographic signals. *IEEE Rev Biomed Eng* 4: 140-154, 2011.

Schendela AA, S. T, K. BS, J. RT, B. LBD, L. K-H, and C. WJ. A cranial window imaging method for monitoring vascular growth around chronically implanted micro-ECoG devices. *Journal of neural engineering* 218: 121-130, 2013.

Schlogl A, and Supp G. Analyzing event-related EEG data with multivariate autoregressive parameters. *Prog Brain Res* 159: 135-147, 2006.

Schwartz AB, Cui XT, Weber DJ, and Moran DW. Brain-controlled interfaces: movement restoration with neural prosthetics. *Neuron* 52: 205-220, 2006.

Senanarong V, Cummings JL, Fairbanks L, Mega M, Masterman DM, O'Connor SM, and Strickland TL. Agitation in Alzheimer's disease is a manifestation of frontal lobe dysfunction. *Dement Geriatr Cogn Disord* 17: 14-20, 2004.

Serruya MD, Hatsopoulos NG, Paninski L, Fellows MR, and Donoghue JP. Instant neural control of a movement signal. *Nature* 416: 141-142, 2002.

Shannon RV. A model of safe levels for electrical stimulation. *IEEE transactions on bio-medical engineering* 39: 424-426, 1992.

Sherrington CS. *The integrative action of the nervous system*. London: Constable, 1911.

Sil'kis IG, and Bogdanova OG. The properties and possible mechanisms of interhemisphere synchronization in the motor cortex of the rat. *Neurosci Behav Physiol* 29: 523-530, 1999.

Sirota A, Montgomery S, Fujisawa S, Isomura Y, Zugaro M, and Buzsaki G. Entrainment of neocortical neurons and gamma oscillations by the hippocampal theta rhythm. *Neuron* 60: 683-697, 2008.

Sjostrom PJ, Turrigiano GG, and Nelson SB. Rate, timing, and cooperativity jointly determine cortical synaptic plasticity. *Neuron* 32: 1149-1164, 2001.

Skrandies W, Wassle H, and Peichl L. Are field potentials an appropriate method for demonstrating connections in the brain? *Exp Neurol* 60: 509-521, 1978.

Spira ME, and Hai A. Multi-electrode array technologies for neuroscience and cardiology. *Nature nanotechnology* 8: 83-94, 2013.

Srinivasan R, Nunez PL, and Silberstein RB. Spatial filtering and neocortical dynamics: estimates of EEG coherence. *IEEE Trans Biomed Eng* 45: 814-826, 1998.

Stark E, Asher I, and Abeles M. Encoding of reach and grasp by single neurons in premotor cortex is independent of recording site. *J Neurophysiol* 97: 3351-3364, 2007.

Steriade M. Cellular substrates of brain rhythms. In: *Electroencephalography: basic principles, clinical applications, and related fields, 5th Edition*, edited by Niedermeyer E, and Lopes da Silva FH. Philadelphia: Lippincott Williams & Wilkins, 2005, p. 31-84.

Steriade M. Impact of network activities on neuronal properties in corticothalamic systems. *J Neurophysiol* 86: 1-39, 2001.

Stolwijk JA, Hartmann C, Balani P, Albermann S, Keese CR, Giaever I, and Wegener J. Impedance analysis of adherent cells after in situ electroporation: non-invasive monitoring during intracellular manipulations. *Biosensors & bioelectronics* 26: 4720-4727, 2011.

Stoney SD, Jr., Thompson WD, and Asanuma H. Excitation of pyramidal tract cells by intracortical microstimulation: effective extent of stimulating current. *J Neurophysiol* 31: 659-669, 1968.

Strick PL. Stimulating research on motor cortex. *Nat Neurosci* 5: 714-715, 2002.

Suner S, Fellows MR, Vargas-Irwin C, Nakata GK, and Donoghue JP. Reliability of signals from a chronically implanted, silicon-based electrode array in non-human primate primary motor cortex. *IEEE Trans Neural Syst Rehabil Eng* 13: 524-541, 2005.

Szarowski DH, Andersen MD, Retterer S, Spence AJ, Isaacson M, Craighead HG, Turner JN, and Shain W. Brain responses to micro-machined silicon devices. *Brain Res* 983: 23-35, 2003.

Tehovnik EJ. Electrical stimulation of neural tissue to evoke behavioral responses. *J Neurosci Methods* 65: 1-17, 1996.

Tehovnik EJ, Tolias AS, Sultan F, Slocum WM, and Logothetis NK. Direct and indirect activation of cortical neurons by electrical microstimulation. *J Neurophysiol* 96: 512-521, 2006.

Tolias AS, Sultan F, Augath M, Oeltermann A, Tehovnik EJ, Schiller PH, and Logothetis NK. Mapping cortical activity elicited with electrical microstimulation using FMRI in the macaque. *Neuron* 48: 901-911, 2005.

Towle VL, Carder RK, Khorasani L, and Lindberg D. Electrocorticographic coherence patterns. *J Clin Neurophysiol* 16: 528-547, 1999.

Tranchina D, and Nicholson C. A model for the polarization of neurons by extrinsically applied electric fields. *Biophysical journal* 50: 1139-1156, 1986.

Valentin A, Anderson M, Alarcon G, Seoane JJ, Selway R, Binnie CD, and Polkey CE. Responses to single pulse electrical stimulation identify epileptogenesis in the human brain in vivo. *Brain* 125: 1709-1718, 2002.

van 't Klooster MA, Zijlmans M, Leijten FS, Ferrier CH, van Putten MJ, and Huiskamp GJ. Time-frequency analysis of single pulse electrical stimulation to assist delineation of epileptogenic cortex. *Brain* 134: 2855-2866, 2011.

van Kuyck K, Welkenhuysen M, Arckens L, Sciot R, and Nuttin B. Histological alterations induced by electrode implantation and electrical stimulation in the human brain: a review. *Neuromodulation : journal of the International Neuromodulation Society* 10: 244-261, 2007.

Varela F, Lachaux JP, Rodriguez E, and Martinerie J. The brainweb: phase synchronization and large-scale integration. *Nat Rev Neurosci* 2: 229-239, 2001.

Vetter RJ, Williams JC, Hetke JF, Nunamaker EA, and Kipke DR. Chronic neural recording using silicon-substrate microelectrode arrays implanted in cerebral cortex. *IEEE transactions on bio-medical engineering* 51: 896-904, 2004.

Ward MP, Rajdev P, Ellison C, and Irazoqui PP. Toward a comparison of microelectrodes for acute and chronic recordings. *Brain Res* 1282: 183-200, 2009.

Wegener J, Keese CR, and Giaever I. Recovery of adherent cells after in situ electroporation monitored electrically. *BioTechniques* 33: 348, 350, 352 passim, 2002.

Weiland JD, and Anderson DJ. Chronic neural stimulation with thin-film, iridium oxide electrodes. *IEEE transactions on bio-medical engineering* 47: 911-918, 2000.

Wessberg J, Stambaugh CR, Kralik JD, Beck PD, Laubach M, Chapin JK, Kim J, Biggs SJ, Srinivasan MA, and Nicolelis MA. Real-time prediction of hand trajectory by ensembles of cortical neurons in primates. *Nature* 408: 361-365, 2000.

Wigstrom H, and Gustafsson B. Postsynaptic control of hippocampal long-term potentiation. *J Physiol (Paris)* 81: 228-236, 1986.

Wilks SJ, Koivuniemi AS, Thongpang S, Williams JC, and Otto KJ. Evaluation of micro-electrocorticographic electrodes for electrostimulation. *Conference proceedings : Annual International Conference of the IEEE Engineering in Medicine and Biology Society IEEE Engineering in Medicine and Biology Society Conference* 2009: 5510-5513, 2009.

Williams JC, Hippensteel JA, Dilgen J, Shain W, and Kipke DR. Complex impedance spectroscopy for monitoring tissue responses to inserted neural implants. *Journal of neural engineering* 4: 410-423, 2007.

Wold S, Ruhe A, Wold H, and Dunn III WJ. The collinearity problem in linear regression. The partial least squares (PLS) approach to generalized inverses. *SIAM J Sci Stat Comput* 5: 735-743, 1984.

Womelsdorf T, Schoffelen JM, Oostenveld R, Singer W, Desimone R, Engel AK, and Fries P. Modulation of neuronal interactions through neuronal synchronization. *Science* 316: 1609-1612, 2007.

Wongsarnpigoon A, and Grill WM. Computational modeling of epidural cortical stimulation. *Journal of neural engineering* 5: 443-454, 2008.

Woolsey CN, Settlage PH, Meyer DR, Sencer W, Hamuy TP, and Travis AM. Patterns of localisation in precentral and 'supplementary' motor areas and their relation to the concept of a premotor area. *Research Publications, Association for Research in Nervous and Mental Diseases* 30: 238-264, 1952.

Yazdan-Shahmorad A, Kipke DR, and Lehmkuhle MJ. Polarity of cortical electrical stimulation differentially affects neuronal activity of deep and superficial layers of rat motor cortex. *Brain Stimul* 4: 228-241, 2011a.

Yazdan-Shahmorad A, Lehmkuhle MJ, Gage GJ, Marzullo TC, Parikh H, Miriani RM, and Kipke DR. Estimation of electrode location in a rat motor cortex by laminar analysis of electrophysiology and intracortical electrical stimulation. *Journal of neural engineering* 8: 046018, 2011b.

Yuen TG, Agnew WF, and Bullara LA. Tissue response to potential neuroprosthetic materials implanted subdurally. *Biomaterials* 8: 138-141, 1987.

Zanos S. Neural correlates of high-frequency intracortical and epicortical field potentials. *J Neurosci* 29: 3673-3675, 2009.

Zanos S, Richardson AG, Shupe L, Miles FP, and Fetz EE. The Neurochip-2: an autonomous head-fixed computer for recording and stimulating in freely behaving monkeys. *IEEE transactions on neural systems* *and rehabilitation engineering : a publication of the IEEE Engineering in Medicine and Biology Society* 19: 427-435, 2011.

Zucker RS. Short-term synaptic plasticity. *Annu Rev Neurosci* 12: 13-31, 1989.

Zucker RS, and Regehr WG. Short-term synaptic plasticity. *Annu Rev Physiol* 64: 355-405, 2002.